Biomimetic Surface Coatings

from Modular Amphiphilic Proteins

Fan Wan

Thesis submitted to
the Faculty of Graduate and Postdoctoral Studies
in partial fulfillment of the requirements
for the Doctorate in Philosophy degree in Physics

Department of Physics
Faculty of Science
University of Ottawa

Abstract

Engineering of biofunctional scaffolds to precisely regulate cell behavior and tissue growth is of significance in regenerative medicine. Protein-based biomaterials are attractive candidates for functionalization of scaffold surfaces since the ability to precisely control protein sequence and structure allows for fine-tuning of cell-substrate interactions that regulate cell behavior. In this thesis, a series of de novo proteins for bio-functionalization of interfaces was designed, synthesized, and studied. These proteins are based on a diblock motif consisting of a surface-active, amphiphilic block β-sheet domain linked to a disordered, water-soluble block with a terminal functional domain. Several types of functional domains were investigated, including sequences that act as ligands for cell surface receptors and sequences that act as templates for the growth of inorganic particles. Under moderate temperature and pH conditions, the amphiphilic β-sheet block was shown to have a strong affinity to a variety of scaffold materials and to form stable protein coatings on hydrophobic materials by self-assembly. Moreover, the surface adsorption of the proteins was shown to have minimal impact on the presentation of the functional end domains in the soluble block. For the case of diblocks with the RGDS integrin binding sequence, the capability for mediating cell attachment and spreading was demonstrated via control over ligand density on hydrophobic polymer surfaces. The case of diblock proteins with templating domains for inorganic materials was investigated for two systems. First, hydroxyapatite-binding domains were ligated to the end terminus of the water-soluble block to develop proteins for possible bone regeneration applications. It was demonstrated that the hydroxyapatite-binding domain had strong affinity to hydroxyapatite nanoparticles and was able to induce calcium phosphate mineralization on the surfaces coated with diblock proteins from dilute solutions

with Ca^{2+} and PO_4^{3-}. Next, a silver-binding domain was ligated to the end terminus to create a diblock protein for potential antimicrobial surface applications. The silver-binding domain was shown to accumulate and reduce silver ions, resulting in the formation of silver nanoparticles on the surfaces functionalized by the protein.

Advisor: James L. Harden

Statement of Originality

Except stated otherwise, the results presented in this thesis were obtained by the author during the period of her Ph.D. research project under the supervision of Dr. James L. Harden. They are to the best of her knowledge original.

Conception

Experimental ideas, methodologies and conception of the research plan were developed in collaboration with my supervisor, Dr. James L. Harden.

Experiments and Analysis

I performed all experiments and data analyses.

The DNA cloning was performed in collaboration with Stephen E. Fisher.

Scott Dick performed ^{125}I-labelling experiment, which is presented in appendix C and appendix D.

Phase contrast and confocal imaging were taken in collaboration with Zeinab Al-Rekabi

FTIR-ATR experiments were performed in collaboration with Jonathan Labriola.

Figure 6-9c and Figure 6-9d were taken using JEOL USA JEM-2100F Transmission Electron Microscope in collaboration with Yun Li.

Data interpretation and conclusions were developed through discussions with Dr. James L. Harden.

Thesis

This thesis is my own work. I thank Dr. James L. Harden for providing editorial assistance.

Acknowledgements

First and foremost, I would sincerely like to thank Professor James L. Harden, my research supervisor, for his expert advice and his enormous support, without which this work would not have been possible. His vast knowledge, wise vision and guidance in scientific research made me grow as a scientist.

I would like to thank Dr. Scott Dick for his continuous support, infinite patience and guidance in the lab, and also for his help with ^{125}I-labeling studies. I would also like to thank Dr. Stephen E. Fisher for his contributions on DNA cloning, Zeinab Al-Rekabi for her help with Microscope imaging, and Yun Li for her professional technical support.

Special thanks also to Professor Andrew Pelling, Professor Michel Godin, Professor Natalie Goto, Professor John E. Baenziger and Professor Juan C. Scanio for kindly helping me carry out the experimental project using instruments in their labs.

I would also like to thank members of the Harden lab and Pelling lab for showing me a different perspective of this research field and helping me out along the way. Especially thanks to Mona for her kind words of support and to Scott Shane for all the insight and advice he has given to me.

Thanks to my parents for their love, support and faith in me.

Last but not least, I would like to take this opportunity to thank my husband Xin and son Ethan for being by my side every day throughout this experience. Their immense patience, cooperation and love help me reach this goal.

Table of Contents

List of Figures

List of Tables

List of Abbreviations

kDa	kilo-Dalton
RU	Resonance unit, 1RU=1pg/mm^2
μM, μm	micro-Molar, micro-meter (10^{-6})
DMP1	Dentin matrix protein1
DNA	Deoxyribonucleic acid
ECM	Extracellular Matrix
E. coli	Escherichia coli
FA(s)	Focal Adhesion(s)
FN	Fibronectin
HFF	Human Foreskin Fibroblast
LN	Laminin
RGDS	Arg-Gly-Asp-Ser
YIGSR	Tyr-Ile-Gly-Ser-Arg
VN	Vitronectin
AgNPs	Silver nanoparticles
Au	Gold
HA	Hydroxyapatite
OCP	Octacalcium phosphate
PEG	Poly-ethylene glycol
PET	polyethylene terephthalate
PMSF	Phenylmethylsulfonyl fluoride
PS	Polystyrene
SAM	Self-assembled monolayer
ATR	Attenuated total reflectance
CD	Circular dichroism
DSC	Differential scanning calorimetry
EDS	Energy-dispersive X-ray spectroscopy
FPLC	Fast performance liquid chromatography
FT-IR	Fourier transform infrared spectroscopy
MALDI	Matrix Assisted Laser Desorption Ionization

MALDI-TOF	Matrix-assisted laser desorption ionization-time-of-flight mass spectroscopy
OD	Optical density
PCR	Polymerase chain reaction
SDM	Site-directed-mutagenesis
SDS- PAGE	Sodium Dodecyl Sulfate- Polyacrylamide gel electrophoresis
SEM	Scanning electron microscopy
SPR	Surface Plasmon Resonance
TEM	Transmission electron microscopy
UV	Ultra-violet
UV-Vis	Ultraviolet–visible spectroscopy
BSA	Bovine Serum Albumin
$CaCl_2$	Calcium chloride
dH_2O	Distilled water
DMSO	Dimethyl Sulfoxide
DMEM	Dulbecco's Modified Eagle Medium
DNaseI	Deoxyribonuclease I
dNTPs	Deoxynucleotide Triphosphates
EDTA	Ethylenediaminetetraacetic acid
FBS	Fetal bovine serum
IPTG	Isopropyl β-D-1-thiogalactopyranoside
KH_2PO_4	Potassium phosphate monobasic
LB	Luria-Bertani Medium
$MgCl_2$	Magnesium Chloride
$MgSO_4 \cdot 7H2O$	Magnesium sulfate heptahydrate
$MnCl_2$	Manganese chloride
NaCl	Sodium Chloride
$NaHCO_3$	Sodium bicarbonate
NHS	N-Hydroxysulfosuccinimide
$(NH_4)_2HPO4$	Ammonium phosphate dibasic
PBS	Phosphate-buffered saline
PNK	Polynucleotide kinase
TFA	Trifluoroacetic acid

Chapter 1

Introduction

1.1 Medical Challenges and Tissue Engineering

Damage and degeneration of tissues and organs in the human body as a result of disease, injury and trauma are typically treated with organ and tissue transplantation. This treatment has been used for almost 60 years since the kidney was first transplanted in 1955. However, major problems exist in traditional transplantation surgeries either by autolograft, which transplants tissue from one site to another in the same patient, or by allograft, which transplants tissue from one individual to another. Shortage of tissue or organ donors is probably the major problem and becomes worse yearly as the population ages [1, 2]. This problem is compounded by frequent cases of immunological rejection and donor site morbidity. The latest annual report by the Canadian Organ Replacement Register (CORR) of the Canadian Institute for Health Information (CIHI) showed that there were 1,033 organ donors (living and deceased) in 2011 and 4,543 patients were still waiting for organ transplant at the end of that year [3]. The Scientific Registry of Transplant Recipients (SRTR), in collaboration with the Organ Procurement and Transplantation Network (OPTN) in the USA, registered 14,144 donors in 2011, and 120,012 patients awaiting transplantation at the end of that year [4]. To reduce the shortage of available organs, and to overcome problems associated with transplantation such as donor site morbidity and immune rejection,

tissue engineering has emerged and grown as a new multi-disciplinary scientific field during the last several decades.

The term tissue engineering was initially defined at the first National Science Foundation (USA) workshop in 1988 as “the application of the principles and methods of engineering and life sciences toward fundamental understanding of structure-function relationship in normal and pathological mammalian tissues and the development of biological substitutes for the repair or regeneration of tissue or organ function.”[5] By employing a variety of knowledge from different disciplines, including biology, biochemistry, biophysics, biotechnology, engineering, materials science, and medical sciences, tissue engineering aims to create biological substitutes for the regeneration of damaged tissues and organs through the delivery of signaling biomolecules onto scaffolds for cell and tissue growth. Thus, tissue engineering encompasses three basic elements including scaffolds, cells and signaling biomolecules (including growth factors) [6].

1.2 Biomaterials as Scaffolds

A scaffold refers to a non-living, porous, degradable structure which defines the geometry of the replacement tissue as well as provides environmental cues to promote tissue regeneration [7]. Designing scaffolds capable of recreating the *in vivo* microenvironment is one of the major goals in tissue engineering. A variety of biomaterials have been used in designing scaffolds. Biomaterials were first defined as non-living substances used in medical devices with strictly structural functions (for example, a joint prosthesis) [8]. The development of biotechnology extended the concept of biomaterials as naturally or

synthetically produced substances (other than drugs) or combination of substances which evaluate, treat, augment, or replace tissues, organs, or functions of the body as a whole or as a part of a system during a period of time [9]. Thus, biomaterials have evolved from simply providing structural support toward the goal of targeted tissue regeneration. Numerous scaffolds produced from either natural biomaterials or synthetic biomaterials have been developed to accommodate mammalian cells, to modulate cell adhesion and spreading, and to regenerate three-dimensional tissues and organs like skin, cartilage and bone. To succeed in these roles, such biomaterials must possess [10,11]:

- Biocompatibility, which means no potential of serious immunogenicity or cytotoxicity to native cells, tissues or organs in vivo;
- Biodegradability, to allow for the scaffold to be replaced gradually in order to minimize the long-term biocompatibility concerns;
- Mechanical strength, to mimic the mechanical properties of the tissue and maintain geometrical tissue constraints;
- Appropriate surface properties to stimulate and maintain normal cellular behavior, such as attachment, differentiation and proliferation;
- High porosity with interconnected pores of appropriate size, to supply nutrition, cellular infiltration and tissue integration, etc;
- Flexibility of fabrication into a variety of sizes and shapes.

It is challenging to design homogeneous biomaterials that fulfill all these requirements for successful scaffolds at the same time. Therefore, a common approach is to design and fabricate composite scaffold systems from several different biomaterials, each

fulfilling one or more of the above criteria. For example, a successful scaffold system might be fabricated from a biodegradable synthetic polymer material with appropriate mechanical and microstructural properties that is subsequently modified to give it specific biochemical surface properties needed for the desired interaction with cells or other biological attributes (referred in the following as “biofunctional” properties). This thesis focuses on designer proteins for such surface modification that incorporate biofunctional domains or inorganic templating sequences to improve cell attachment, induce calcium phosphate deposits, or initiate broad-acting biocidal activities to otherwise bioneutral materials.

1.3 Surface Modification of Biomaterials

Since most biological interactions occur at the interface between the scaffold material and the biological environment, the surface structure and properties of materials play essential roles in controlling these interactions [12]. Scaffolds gain new surface functionalities that they do not originally have through surface modification. In this case, the aim of such modification of a scaffold surface is to improve specific biological functions such as cell attachment without changing the mechanical and structural properties of the scaffold [13].

Surface modification generally focuses on: (1) physically or chemically altering the composition of a surface (to display specific molecules, compounds or atoms) using techniques such as chemical modification and etching; (2) coating a surface with a material of desirable composition and functionality via passive adsorption, chemical grafting, or thin film deposition; and (3) fabricating surface textures or patterns using lithographic or printing

methods such as UV-based imprinting [13]. Such modified surfaces may have a wide range of functions, including modulating cell adhesion and proliferation, modifying blood compatibility, improving anti-bacterial properties, increasing tissue-bonding affinity, controlling protein adsorption, improving immune response, and altering transport properties[13]. For example, Kazemzadeh-Narbat et al. [14] demonstrated that a micro-porous, calcium phosphate-coated titanium surface modified by a cationic, antimicrobial peptide possessed antibiotic activity against certain bacteria. Plasma treatment is simple and widely used method for modifying the chemical reactivity of surfaces. Polycaprolactone scaffolds treated with oxygen plasma were shown to exhibit altered surface wettability, surface energy, and surface biocompatibility [15]. Physical vapour deposition has been used to generate antibiotic surface activity for blood-contacting materials by small biological protein domains [16]. Porous polyelectrolyte multilayers, assembled on glass slides by sequential deposition, were used to mimic the pore sizes of corneal membranes *in vivo* [17]. These polyelectrolyte coatings were found to significantly enhance corneal epithelial cellular response such as proliferation and migration [18]. This thesis focuses on a new class of de novo proteins that can provide tailored surface functionalities via self-assembly on scaffold materials.

1.3.1 Strategies to Functionalize Biomaterial Surfaces

Immobilization of biomolecules such as proteins, peptides or polysaccharides on scaffold surfaces is crucial for generating bio-mimetic surfaces [18, 19]. Such immobilized molecules act to induce specific cellular behavior and direct new tissue formation, as well as to minimize the non-specific adsorption of biomolecules from solution. Molecular

immobilization strategies typically include enhancing adsorption of specific proteins or materials, and passivation of scaffold surfaces to resist non-specific adsorption, in order to obtain a surface with well-defined cell-material interactions.

Since most scaffold materials are not inherently bioinert, a scaffold biomaterial elicits non-specific protein adsorption immediately when it contacts cell culture media or body fluids [20]. Such non-specific proteins interact with cells and trigger unexpected intracellular responses. Therefore, passivating the surfaces is essential for proper function of bio-mimetic scaffold surfaces. It is widely accepted that hydrophilic and charged molecules are effective against protein adsorption [21]. Poly (ethylene glycol) (PEG), an uncharged hydrophilic polymer, also known as poly (ethylene oxide) (PEO), has been widely utilized due to its resistance to adsorption of proteins and cells [22-24]. In addition to PEG, phospholipid surfaces [25] and saccharide surfaces [26] are also commonly used for reducing the non-specific protein adsorption.

Molecular recognition, which is a specific binding process between molecules, is probably the most important attribute required of de novo scaffold surfaces. The prototypical class of molecular recognition is the ligand-receptor interaction in which a small molecule (ligand) binds to another macromolecule (receptor) and elicits a normal biological response [27]. Such ligand-receptor interactions can be achieved by modifying scaffold surfaces with specific cell binding and signaling motifs. For this purpose, native macromolecules of the extracellular matrix (ECM), including glycosaminoglycans such as heparan sulphate, proteoglycans such as aggrecan, and proteins such as fibronectin (FN), vitronectin (VN) and laminin (LN), have been used. Alternatively, short bio-molecular peptides or

polysaccharides that specifically interact with cell receptors have been isolated from ECM macromolecules and used for surface modification [28]. These cell-binding motifs are able to link the cytoskeleton with the adhesive scaffold surface, resulting in the activation of a variety of signal transduction cascades responsible for regulating various cell-matrix interactions and cellular behaviors [29]. Many cell-binding motifs have been utilized to generate specific cellular responses and make materials biocompatible [30, 31]. Commonly used cell-binding motifs in tissue engineering are discussed in more detail in chapter 2.

Numerous functional domains initiate specific non-biological molecular recognition. For example, Roy *et al.* [32] have demonstrated that a peptide with amino acide sequence of SVSVGMKPSPRP has high binding affinity to hydroxyapatite (HA). As HA is associated with bone tissue formation, methods to induce the formation of HA nanocrystals on scaffold surfaces of interest in tissue engineering. Silver-binding peptides isolated by Naik et al. [33] are capable of reducing silver ions to nucleate the formation of silver nanoparticles from a silver nitrite aqueous solution. Such silver nanoparticles are known to act as potent yet biocompatible biocides, so they are also of interest as components of biomaterials scaffolds. In this thesis, we are interested in generating surfaces possessing both attributes to improve cell attachment and to produce medically relevant inorganic particles for various applications in tissue engineering.

1.3.2 Protein-based Biomaterials

Protein-based biomaterials have demonstrated potential for applications in biomedicine, biotechnology and synthetic biology, due to several significant advantages they

have compared to naturally derived protein materials and synthetic polymers. Naturally derived proteins, such as collagen, gelatin, fibrin and elastin, inevitably undergo batch-to-batch variability, as they are typically isolated from tissues. Since these are typically large biomolecules, it is also difficult to modify their properties without compromising their native structure and function. Moreover, the display of the desired signaling ligands in these proteins is not easily controlled in a non-native environment (i.e. when immobilized on a surface). Disease transmission and immunogenic responses related to their natural sources are also a potential hazard [34]. For synthetic polymers, there are disadvantages associated with the lack of precise control over monomer sequence and polymer molecular weight. Specifically, the challenges associated with synthesis of polymers composed of more than two distinct monomers in a prescribed sequence order are formidable. As sequence typically dictates function in biomacromolecules, this is a serious deficiency. In contrast, protein-based biomaterials possess chemical diversity and structural complexity since they are built from more than 20 natural and non-natural amino acids. They possess not only biological functionalities and complex structures like naturally derived proteins, but also a high degree of design-ability when using molecular biology methods. Monodisperse product from recombinant protein expression and reduced toxicity are significant advantages for these protein-based biomaterials compared with synthetic polymers. More importantly, protein-based biomaterials are highly controllable in terms of molecular weight and sequence, and easily modified to specific needs [34-36].

Numerous recombinantly synthesized natural proteins, such as silk, elastin, and collagen, have been utilized for direct replacement of biological tissues [34, 37]. For

example, Liu et al. fabricated hydrogels from recombinant human collagen solutions as corneal substitutes. These engineered cornea materials exhibited comparable white light transmission, sufficient support of *in vitro* epithelium and nerve overgrowth, and appropriate tensile strength and elasticity for use in corneal replacement [38]. Later, this research group showed regeneration and repair of the damaged eye tissue with biosynthetic corneas based on an early phase clinical trial with 10 patients [39]. Bio-mimetic peptides have been used to impart precise biomolecular recognition and functionality to biomaterials used for specific medical and biological applications [34, 37]. For example, a PEGylated poly-amidoamine dendrimer modified by a cyclic RGD peptide demonstrated improved antitumor activity by actively targeting to neovascular endothelial cells and tumor cells via RGD–integrin recognition [40]. Finally, protein-based biomaterials can be designed to self-assemble from their protein or peptide components peptides into fibers, onto surfaces, or into hydrogel networks [30, 41-43], as discussed in more detail below.

1.3.3 Molecular Self-assembly

Molecular self-assembly is a ubiquitous process in nature by which individual molecular building blocks spontaneously associate and organize into complex, stable and supermolecular patterns or structures through weak, non-covalent interactions without external intervention [44]. Complementarities in shape among molecular building blocks and the formation of non-covalent interactions between molecules are two key elements during molecular assembly and organization. These non-covalent interactions, typically including hydrophobic and hydrophilic interactions, electrostatic interactions, hydrogen bonding, and

van der Waals interactions, are weak. Their collective effects, however, dominate conformational behavior and drive the formation of physically stable structures [44].

Self-assembly is critical to the high level of hierarchical structure and function achieved by biological systems in processes as diverse as structural scaffolding, mineral templating and selective transport [45-47]. It is also an attractive fabrication method for biomaterials, especially for tissue engineering scaffolds, as the fabrication process takes place in aqueous environments without toxic reagents and with minimal outside intervention. Many self-assembling biomaterials are formed from components with amphiphilic attributes. These amphiphilic domains have separate organized hydrophobic and hydrophilic domains, as for example, in the amphiphilic α-helical leucine zipper motif [48, 49]. Amphiphilicity drives biomolecules as building blocks to associate through weak, noncovalent hydrophobic interactions, to a variety of precisely ordered assemblies, such as micelles and filaments, under aqueous conditions [50]. The morphology of the self-assembling biomaterials depends on the structure of the building blocks as well as on the external environmental conditions, including the pH, temperature, and ionic strength [50, 51].

Since self-assembling protein biomaterials are synthesized from monomeric building blocks with exact molecular-level precision, the structure and function of the final biomaterials are controllable and usually encoded in the primary structure of its building blocks [50]. Properties of these biomaterials can also be independently manipulated, tuned and tailored through appropriate genetic modular modifications to suit a specific tissue engineering application. In particular, by fusing biofunctional peptide sequences to assembly domains, the resulting self-assembled material is able to interact with cells in a prescribed

manner. For example, incorporation of specific cell binding domains like RGDS and YIGSR in the self-assembling biomaterials leads to a significant increase in cell attachment and spreading [30]. Programmed biomaterial degradation can also be achieved by inserting a recognition site for an enzyme with proteolytic activity [52]. The addition of HA-binding peptides provides a route to initiate calcium phosphate deposition and subsequent HA crystal formation onto the biomaterial [32, 53, 54]. Overall, this approach allows for the facile formulation of biomaterials with a wide range of functional attributes by self-assembly.

Numerous self-assembling systems have already been developed [55, 56]. One example, pioneered by the Tirrell group [57], is the triblock protein system consisting of a soluble, disordered coil flanked on both ends by amphiphilic helical leucine zipper domains. The leucine zipper motif has a repetitive heptad pattern ('*abcdefg*') with hydrophobic residues (often leucines) at the '*a*' and '*d*' positions while '*e*' and '*g*' are (typically charged) polar residues. In an aqueous solution, such sequences adopt an amphiphilic, α-helical secondary structure with a hydrophobic strip composed of the '*a*' and '*d*' residues. These amphiphilic helices associate into bundles composed of a hydrophobic core of '*a*' and '*d*' residues shielded from the aqueous solution. In a triblock protein system with such amphiphilic helical ends, helix bundle formation leads to the self-assembly of a reversible hydrogel network. Mi et al. [58] developed the first such system that included cell binding domains in the central spacer block, thereby providing a means of creating self-assembly of protein scaffolds with specific cell binding capability. Subsequent work investigated the utility of such a biofunctional triblock protein motif for functionalization of otherwise bioneutral surfaces with the RGDS integrin binding sequence [30, 59].

As an alternative to amphiphilic helical sequences as association domains, this thesis work explores the use of amphiphilic β-sheet sequences to functionalize hydrophobic, bioneutral material surfaces. In this study, a series of amphiphilic diblock proteins, composed of an amphiphilic β-sheet assembly sequence joined to a soluble, disordered domain with a terminal functional peptide sequence, were developed and studied for functionalizing scaffold interfaces by self-assembly.

1.4 Aims and Hypothesis of this Study

Inspired by the view of an ideal scaffold, self-assembling biomaterials, and genetic modular design methods, the principal aims of this thesis work were (1) to develop modular proteins based on a amphiphilic diblock motif for creating biofunctional scaffold interfaces by self-assembly and (2) to characterize the surface modification capabilities of these new proteins. Three variants of this diblock motif were explored for their capability to realize three different biomaterial surfaces: surfaces to regulate cell behavior such as cell adhesion and growth; surfaces with the ability to bind and/or bind to HA nanoparticles for potential use for bone and tooth tissue regeneration; and surfaces to induce the formation of bound silver nanoparticles for potential use as antimicrobial biomaterial surface treatments.

The hypothesis explored in this thesis is that proteins based on an amphiphilic diblock motif can provide a facile and well-controlled means to functionalize scaffold surfaces with specific biological or physical attributes. To test this hypothesis and achieve the aims of the thesis, a number of studies were carried out as presented in the following chapters of the thesis.

1.5 Layout of the Thesis

This thesis work is presented in seven chapters and four appendices. Following the Introduction (this present chapter), the design of the diblock proteins with functional domains and the recombinant DNA methods used to biologically synthesize and purify these proteins is presented in Chapter 2. Included in this chapter are a review of the basic knowledge of protein structures and protein design methodologies, and a brief presentation of the methods used for creating the recombinant DNA and for expression and purification of proteins. In Chapter 3, the physical properties of the diblock proteins created are evaluated using mass spectroscopy, circular dichroism spectroscopy (CD), differential scanning calorimetry (DSC), and Fourier transform infared spectroscopy (FTIR). A basic review of each characterization method is included in the discussion. The results demonstrate that incorporation of the ECM-derived bioactive peptides into diblock proteins does not have a significant impact on their secondary structures. Chapter 4 presents studies of the biofunctional surfaces generated via passive adsorption and self-assembly of BSL-RGDS, one of the principal bioactive variants of the diblock proteins of this work. Results from phase contrast optical microscopy and confocal fluorescence microscopy, biochemical assays for cell response, and immunofluorescence microscopy studies of cells on the surfaces are presented and discussed. These studies demonstrated that the surface concentration of the bioactive ligand, RGDS, can be titrated and controlled, thereby manipulating cell responses such as attachment and spreading, and that the self-assembly method for surface functionalization with these bioactive diblock proteins is effective for both smooth and porous materials. In Chapter 5, a diblock protein variant with a functional

HA-binding peptide sequences is discussed. Electron microscopy studies demonstrated that this protein has high-specific binding affinity to crystalline hydroxyapatite and is able to direct the mineralization process of calcium and phosphate to produce hydroxyapatite or octacalcium phosphate (OCP) without being affected by the self-assembly of amphiphilic block of proteins. In Chapter 6, another diblock protein variant with a silver-binding domain is discussed. This protein was shown to reduce silver ions in solution and subsequently induce the formation of silver nanoparticles on the silver-binding domain. It was also demonstrated that immobilization of this diblock on a surface does not affect the production of silver nanoparticles by the silver-binding domain AG4, thus providing the possibility to control the deposition of inorganic silver nanoparticles on a protein functionalized scaffold. The final chapter consists of concluding statements about the work performed and results obtained, and suggestions for future applications of these diblock proteins.

Chapter 2

Design of a Library of Diblock Proteins with Functional Domains

2.1 Literature Review

2.1.1 Proteins

Proteins are large biomolecular assemblies consisting of one or more chains of amino acids. As the "molecular machinery" of the cell, proteins perform functions within living organisms including signal transmission, enzymatic catalysis, mechanical support, replication of DNA, immune protection, and response to stimuli [60]. These functions depend strongly on the three dimensional structure of proteins. Amino acids are the base monomeric units of proteins and possess common elements (sketched in Figure 2-1) including a central carbon (C_α) to which is attached an amino group (NH_2) on one side and a carboxyl group (COOH) on the other side. In addition, a side chain (R) which distinguishes one amino acid from another links to the C_α [61].

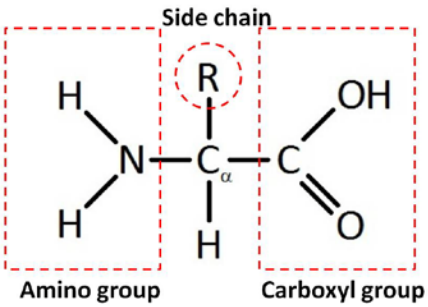

Figure 2- 1 Schematic diagram of an amino acid with C_α**.**

The 20 naturally occurring amino acids are usually divided into three different groups according to the physical attributes of their different side chains. The first group contains hydrophobic side chains, such as Leu, Val, Ala (Here the common 3-letter abbreviation system is used for the amino acids) [61]. The second group consists of potentially charged side chains including Asp, Glu, Arg, and Lys; while the third group includes the neutral, polar side chains such as Ser, Thr, Asn, and Gln [61]. Together the second and third groups are polar or hydrophilic in nature, in contrast with the first group. Schematic diagrams of all naturally occurring amino acids are presented in Figure 2-2.

Proteins with a wide variety of structures and biochemical properties are produced through linking of amino acids by peptide bonds. Peptide bonds are formed by condensing the carboxyl group of one amino acid with the amino group of another to release water [61], as presented in Figure 2-3. This polymerization process is repeated, forming a linear macromolecule defined by a polypeptide main chain with a defined sequence of side chains. The amino acid linear sequence of the polypeptide chain determines the primary structure of proteins. The conformation of the main chain and its side chains defines the higher order structures. The secondary structure of a protein refers to a highly regular localized organization of the main chain. Two main types of the secondary structure, α- helix and β-

sheet, are discussed later in this chapter. The tertiary structure is a description of the complex and irregular folding of the polypeptide chain. It creates a more compact overall structure by arranging the different secondary structural subunits in three dimensions. Such folding is driven by hydrogen boding as well as the non-specific hydrophobic interactions. The quaternary structure is determined by the arrangement of identical or different subunits of a large protein in three dimensions [61, 62]. The following discussion will focus on the proteins with well-defined secondary structure, particularly the β-sheet structure.

2.1.2 The Protein Secondary Structure

The secondary structure of a protein is defined by regular, localized arrangement of its main chain into particular conformations stabilized by hydrogen bonds between different amino acid residues. The possible secondary structures are dictated by interactions (primarily steric) between the side chains. Different secondary structural motifs can be identified using a unique set of backbone dihedral angles φ and ψ (Figure 2-4). The angle φ describes the rotations of the polypeptide backbone around the N-C_α, bonds, while angle ψ describes the rotations of the polypeptide backbone around the C_α-C bonds.

Two of the most commonly occurring secondary structures are the α-helix and the β-sheet structures, sketched in Figure 2-5. A helical secondary structure is comprised of either right-handed or left-handed coiled sequence with well-defined period and pitch. It is primarily stabilized by hydrogen bonds between the carboxyl group of one amino acid with the amino group of non-neighboring amino acid. The α-helix (Figure 2-5(a)) which is defined by an $i \rightarrow i+4$ hydrogen bonding scheme and right-handed helicity is the most stable

and abundant structure in proteins since the arrangement of side chains avoids unfavorable steric interactions [63]. The β-sheet is a common secondary structure formed when two or more adjacent, extended polypeptide chains (β-strands) of 3 to 10 amino acids long are organized with hydrogen bonds between the C=O moieties from one chain and the N-H moieties from another [61,63]. Two classes of β- sheet structures are the parallel β-sheet (Figure 2-5(b)) in which the amino acids of all β-strands are aligned in the same direction, and the antiparallel β-sheet (Figure 2-5(c)) in which the amino acids of adjacent strands are aligned in the opposite direction.

The distribution of dihedral angles of a protein structure is typically presented in a scatter plot of ψ versus φ for all the residues, known as a Ramachandran plot (Figure 2-6). Particular monolithic secondary structures are defined by specific points on a Ramachandran plot. For instance, the right-handed α-helix is characterized by angles φ and ψ of approximately -60° and -45°. Anti-parallel β-sheets are determined by angles φ and ψ of approximately -135° and 150°, and parallel β-sheets are identified with angles φ and ψ of approximately -120° and 135° [63]. Most combinations of angles φ and ψ are excluded due to the steric hindrance of side chains in unfavorable main chain conformations. Figure 2-6 indicates the favorable and unfavorable regions of φ and ψ angles.

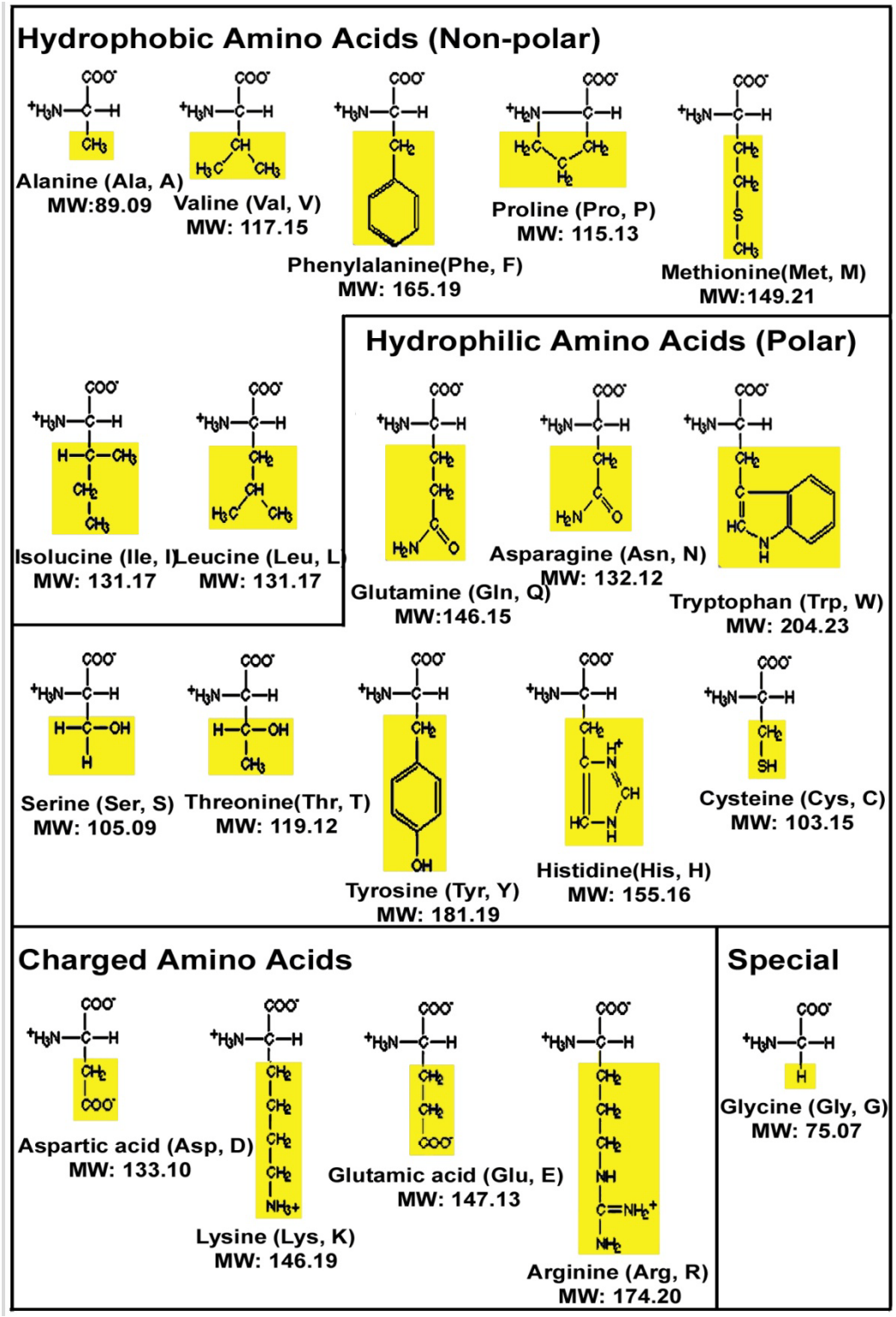

Figure 2- 2 Schematic diagrams of all naturally occurring amino acids with their names and molecular weights beneath. The amino acids are classified based on [61].

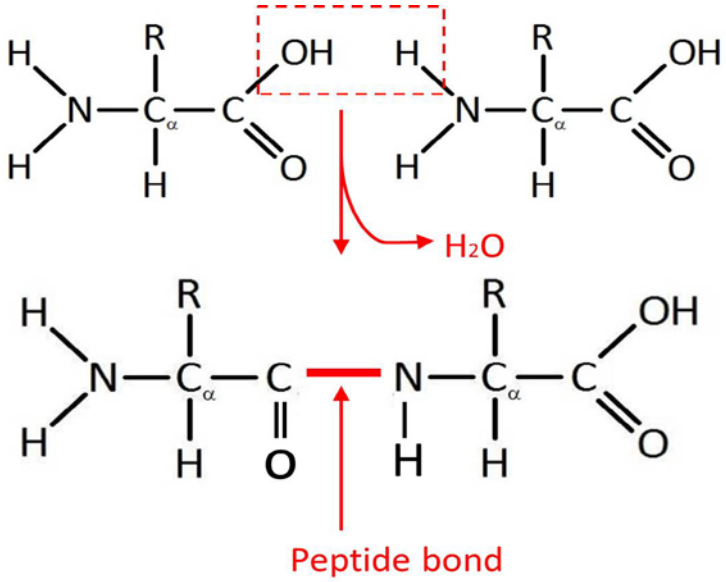

Figure 2- 3 Schematic diagram of peptide bond formation.

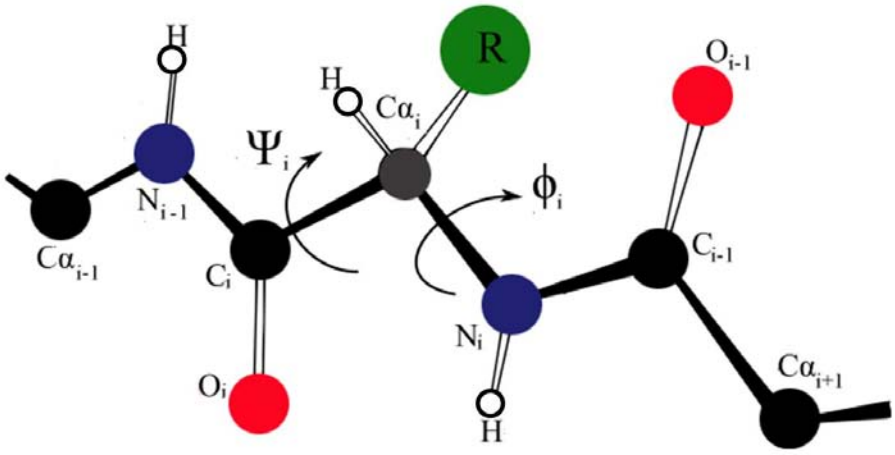

Figure 2- 4 The dihedral angles ψ and φ of a protein conformation.

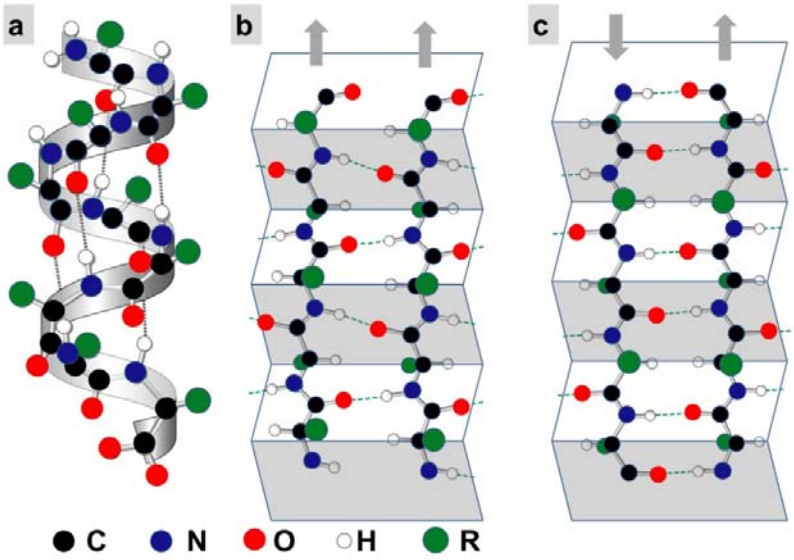

Figure 2- 5 Protein secondary structure. (a) α-helix; (b) parallel β-sheet; (c) anti-parallel β-sheet.

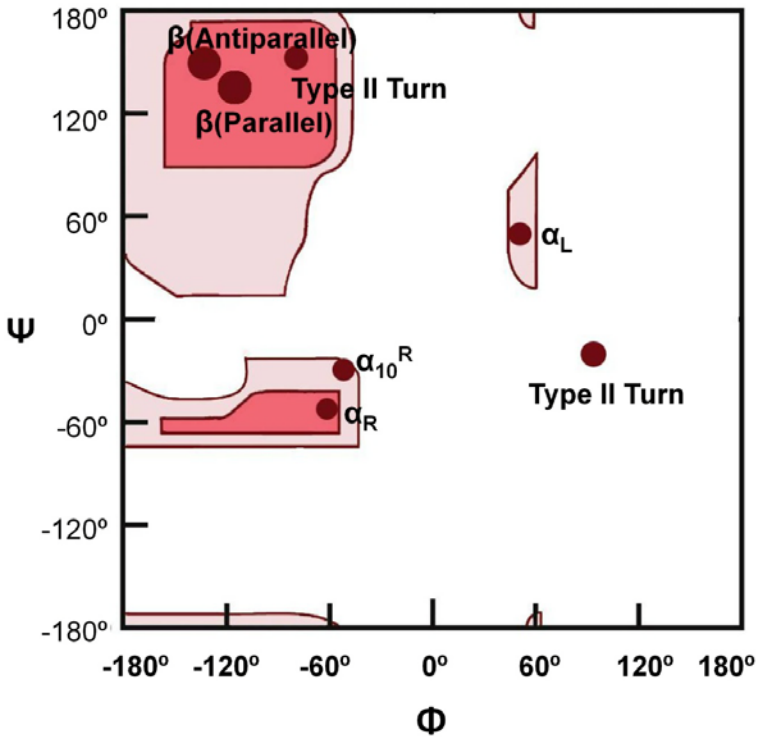

Figure 2- 6 A Ramachandran plot showing the combinations of angles φ and ψ for stable α-helical and β-sheet structures. β(parallel): parallel β-sheets; β(antiparallel): antiparallel β-

sheets; α_R: right-handed α-helices; α_{10}^R: right-handed α_{10}-helices; α_L: left-handed α-helices.

2.1.3 Protein Design Methodologies

The secondary and tertiary structures of a protein are strongly influenced by its linear amino acid sequence. The ability to design amino acid sequences with desired structures would have great impact on biotechnology and biomedical applications. However, among the enormous number of possible amino acid sequences of modest length, only a small portion of them are capable of folding correctly and quickly to native secondary and tertiary states. Thus, the design of desired protein structures still poses many challenges.

Rational protein design and combinatorial protein design are two major methodologies widely used by protein designers [64, 65]. In the rational protein design approach, the scientist uses detailed knowledge of the structure and function of the protein to develop new uniquely- folded, thermally-stable proteins with particular functionality one at a time, typically using a suite of computational and bioinformatics tools. For example, in Mayo's lab a stable, uniquely folded protein domain containing a short helix, two strands and a hairpin was obtained using an automated protein design algorithm. The designed protein was able to mimic the shape of a zinc finger domain without the use of the metal ligand [66]. A prior structural knowledge of a protein is required in the rational protein design to allow scientists to modify a protein in a predicable way. Such structural knowledge is usually unavailable. Compared with rational protein design, combinatorial protein design involves working with a wide range of sequence libraries instead of a single sequence. A typical combinatorial protein design involves three steps: creating diversity by building a

large library of gene variants, screening and selecting mutants or variants with desired functions, and amplifying gene variants identified in the second step [67]. A prior structural knowledge of a protein is not necessary in a combinatorial protein design. On the contrary, to discover desired protein structure combinations and explore new protein functions is one of advantages of combinatorial protein designs. Combination of efficiency and diversity becomes the major challenge due to the exponentially large number of possible sequences. To enhance the possibility of success, the sequence libraries must be confined by existing knowledge on protein structure and protein folding. For instance, the Hecht group [65,69] has explored the amphiphilicity of domains observed in native protein folding and proposed a "binary code" strategy to successfully reduce the complexity of α-helix and β-sheet libraries in combinatorial protein design. In this work, we have utilized this approach for the development of amphiphilic β-sheet domains, as elaborated below.

2.1.4 The 'Binary Code' Strategy

The use of binary patterning of polar and nonpolar amino acids has been extensively investigated by the Hecht group as a design tool for both amphiphilic α-helix and β-sheet libraries. This work demonstrated that appropriate generic patterns of polar and nonpolar residues in designed sequences commensurate with the inherent structural periodicity of a particular secondary structure guide formation of an amphiphilic form of that secondary structure, without regard to the precise identity of the individual amino acids. Moreover, they showed that such amphiphilic secondary structures in turn guide the folding of the polypeptide into a tertiary structure by simultaneously exposing polar residues to solvent and burying nonpolar residues in the interior of the protein [68].

Since α-helices have structural repeats of 3.6 residues per turn, binary patterned sequences designed to be consistent with amphipathic α-helices are linear sequences of polar (P) and nonpolar (N) residues with the pattern of N-N-P-P-N-N-P-P-N-P-P-N-N-P-P-N in which a nonpolar residue is placed at every third or fourth position. Xiong et al. [65] have demonstrated that peptides with such patterns indeed fold into α-helical structures that self-assemble into bundles in order to shield nonpolar faces from the polar solution. In contrast to the α-helical NP pattern, a strict binary patterned sequence of P and N residues, i.e. with a pattern of P-N-P-N-P-N-P, leads to amphiphilic β-strands, regardless of the particular choices of N and P residues. West et al. [69] designed and synthesized a library of such amphiphilic β-sheet structures using this binary code strategy, which were shown to self-associate into aggregates (oligomeric multimers and large fibrils) that shield their nonpolar faces from solution. Moreover, some of these amphiphilic β-sheet designs were shown to associate at interfaces between polar and non-polar phases (such as air-water interfaces) [70, 71], an attribute that is crucial for the work described in this thesis. Hetcht *et al.* [70] reported that β-sheet proteins formed stable films at the air-water interface after they were deposited onto the aqueous surface in a Langmuir–Blodgett trough. The protein surface films stayed robust for many hours at surface pressures corresponding to their assembled states.

Although the patterns of polar and nonpolar residues dictated by an NP code motif must be respected to ensure the formation of amphiphilic α-helices or β-sheet structures, the particular choice of individual residue at each polar or nonpolar position can be extensively varied. Therefore, the libraries generated from the 'binary code' strategy have enormous combinatorial diversity. On the other hand, the detailed choice of residue at each polar or

nonpolar position influences other properties of these proteins. For instance, the stability and type of aggregate formed from these amphiphilic secondary structures (dimers, trimers, fibrils, sheets) and their dependence on solution conditions (pH, temperature, electrolyte concentration) are very sensitive to the details of the sequence [69,70,72].

2.2 Diblock Proteins with Functional Domains

2.2.1 Design of Diblock Proteins

This thesis describes de novo proteins based on a diblock motif designed to form functional interfaces by self-assembly. The artificial protein consists of a surface-active, amphiphilic β-sheet block structure to direct self-assembly onto non-polar surfaces joined to a disordered, water soluble block with an end terminal functional domain (e.g. bio-active ligand or a sequence for templating growth of inorganic materials). A sketch of this diblock motif is given in Figure 2-7. Diblock proteins with several different functional end domains were synthesized and investigated, as described below. Under moderate temperature and pH conditions, the amphiphilic block has a strong affinity for polymer surfaces by self-assembly, thus resulting in a stable monolayer of protein at the material-solution interfaces. In order to ensure the availability of the functional end domains for interaction with cells or constituents in solution, a sufficiently long, soluble, and flexible spacer domain is required. Our hypothesis is that such diblock proteins can be designed with independent surface assembly and functional domains, so that proteins would coat the surfaces by self-assembly, leaving the functional end domain available to promote a specific biological or templating function. The central objective of this study is to design such proteins that are able self-assemble into

stable, functionalized layers with selective bioactive and/or templating sequences. Detailed descriptions of the assembly, spacer and functional domains of these diblock designs are presented below. A complete description of each sequence studied in this thesis is given in Table 2-2.

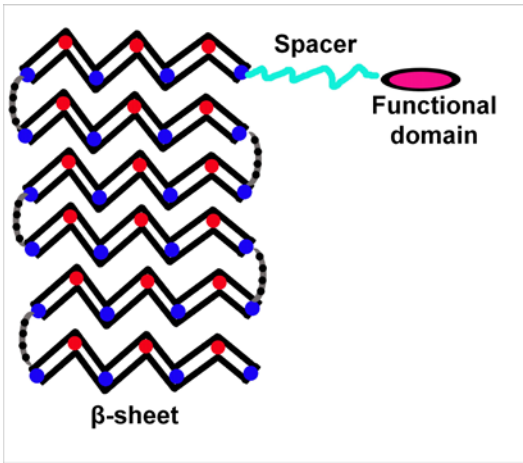

Figure2- 7 A general scheme of the diblock protein.

2.2.1.1 β-sheet Design

The β-sheet design used in this research is based on the #17 β-sheet sequence of Xu *et al.* [70], originally designed using the 'binary code' strategy. It is composed of six amphiphilic β-strands with the P-N-P-N-P-N-P pattern separated by four-residue turns. It was previously demonstrated by Xu *et al.* that sequence #17 was able to fold into a stable amphiphilic β-sheet structure, which was shown to self-assemble into monolayers at an air-water interface (and also oligomerize into large fibrils in electrolyte solution). The amino acid sequence of β-sheet #17 is given below. The beta strand polar/non-polar residues are indicated with red/green font, while the turn residues are in gray font.

β-sheet #17:

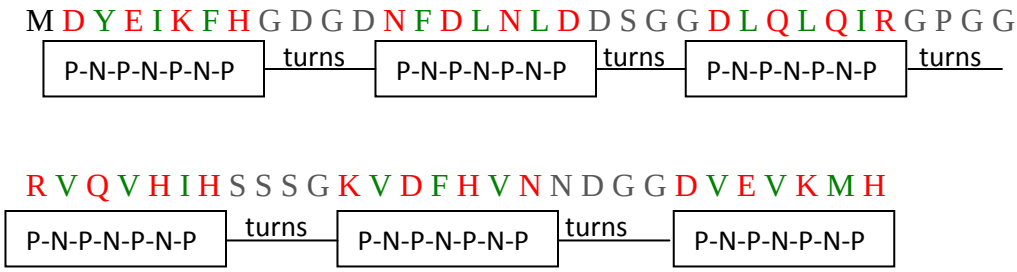

2.2.1.2 Spacer Designs

Several factors affect activity of functional domains immobilized on substrates. Steric inaccessibility of active sites, active sites buried within the protein, partially denatured protein structure due to immobilization, and even physical constraints imposed by the material substrate (e.g. roughness) can all result in unsatisfactory interactions. Combining functional domains with sufficiently long, soluble spacer arms is a proven method to minimize these potential problems [73]. The spacer itself should have no tendency to either form the ordered secondary structure or interfere with the folding of domains. It must be long enough to avoid steric hindrance and allow the functional domains to effectively gain access to the receptor binding. However, the optimal length of such a spacer is unclear a priori and depends on the particular final application. Thus, hydrophilic, disordered coil spacers of two lengths were studied in this thesis: an 8 amino acid peptide sequence (subsequently denoted “short spacer”) and a 19 amino acid peptide sequence (subsequently denoted “long spacer”). These were linked to the C-terminus of the β-sheet sequence to enhance availability of the terminal functional domains (discussed below). The long spacer was based on a sequence originally designed by Whitlow et al. [73] for

reducing aggregation and enhancing proteolytic stability of a single chain variable fragment (scFv). The short spacer is modified from the long spacer by omitting amino acids from Lys8 to Gly18. Glycine and serine residues in both spacers improve conformational flexibility; the charged residues such as glutamic acid and lysine in the long spacer improve the solubility [73, 74]. The sequences of the short and long spacers are shown below:

Short spacer: G S T S G S G T
Long spacer: G S T S G S G K P G S G E G S T K G T

2.2.1.3 Functional Domains

Bio-mimetic materials with tailored cell-substrate interactions can be simply generated by incorporation of bio-active peptides into biomaterials. Many of these peptides originated from ECM proteins such as fibronectin (FN), vitronectin (VN), and laminin (LN), and often such short consensus sequences exhibit similar receptor specificity and binding affinity as the intact ECM proteins. Their advantage lies in their reduced synthesis cost, and their potentially improved steric availability, cell-type selectivity, and solution stability [28]. A range of ECM-derived, bioactive peptides that have been used in biomedical and biotechnology applications are summarized in Table 2-1. Many of these peptides bind to targets for precise regulation of particular cell behaviors.

Well-studied examples of such cell-binding sequences include RGD, YIGSR, DGEA, and IKVAV. Arg-Gly-Asp (RGD), a bioactive tripeptide derived from fibronectin (FN) and laminin (LN), is one of most commonly used bio-active domains. It interacts with several integrin cell adhesion receptors, ultimately resulting in linking the ECM to a cell's

cytoskeleton [75]. This linkage plays an essential role in regulation of numerous cell processes including proliferation, differentiation, migration, and apoptosis. Variations of RGD listed in Table 2-1 were also extensively studied. Tyr-Ile-Gly-Ser-Arg (YIGSR) is a laminin-derived peptide motif that binds to a 67 kDa laminin receptor in many cell types to mediate adhesion and perform numerous physiological processes [76]. Kubota *et al*. [77] reported that YIGSR inhibited the morphological differentiation of endothelial cells into capillary-like structures. Sakamoto et al.[78] showed that YIGSR prevented embryonic angiogenesis via the 32/67 kDa receptor. Iwamoto et al. [79] also confirmed that YIGSR inhibited tumor cell metastases. DGEA, a sequence from collagen, binds selectively to the α2β1 integrin [80]. IKVAV is capable to bind to receptors on neurons and stimulates the extension of neurites [81]. This thesis focuses on diblock protein constructs that incorporate the RGDS and YIGSR cell binding sequences as well as on two inorganic templating sequences.

Phage display (PD), a combinatorial biology technique, has been utilized as a powerful tool in the selection and identification of inorganic templating sequences [82]. Phage display peptide libraries are generated by inserting random sequences within certain genes encoded on phage genomes, thereby creating phages with different but random peptides. These phages are contacted with inorganic substrates to identify inorganic templating ligands. In the last decade, phage displayed peptide libraries have been utilized to select inorganic templating ligands which bind to metals, metal oxides, polymeric materials, mineral, carbon materials, or semiconductors [33, 54, 82-84]. A positively charged gold binding peptide identified from phage display was first reported by Whaley et al. [83]. The

gold nanoparticles as the target materials were assembled on the phage via this peptide. Similarly, two silver binding peptides AG3 and AG4 were selected from phage display based on their capabilities to form silver nanoparticles [33]. Gungormus *et al*. [54] isolated HA- binding peptides HABP1 and HABP2 from phage display and verified that they were able to produce calcium phosphate crystals. A calcite binding peptide was selected from phage display by Gaskin et al. [84] and found to control the calcite crystal formation. In the thesis, we focus on HA-binding peptides with sequences described in Table 2-3 as 5mer, 7mer and 9mer and a silver-binding peptide with sequence described as AG4.

Table 2- 1 Bio-active domains employed for polymeric surface functionalization

Bio-active Domains	Origin	Receptor	Function	References
RGD-based peptides including : RGD, RGDS, GRGD, GRGDF, GRGDS, GYRGDS, RGDC, RGDV, RGDT, LRGDN, GRGDY, GRGDSY, GRGDVY, GRGDSP, GdRGDSP, GRGDTP, GRGDSPC, EPRGDNYR, GGGRGDSP, CGRGDSY, CSSPHSRNSGSGSGSGSGRGDSP	Fibronectin, vitronectin, laminin, and collagen	Integrin α_5 β_1, α_v β_3, and α_1 β_1	Cell adhesion and proliferation	30,75,85-109
YIGSR-based peptides including YIGSR, CYIGSR, GYIGSR, CDPGYIGSR, DPGYIGSR, CDPGYIGSRC	Laminin (β_1 chain)	67-kDa laminin(LN) receptor	Cell Adhesion and proliferation	76-79,88,90, 102-104, 106,108, 110-112
DGEA	Collagen	α_2 $\beta_1$integrin	Adhesion of platelets, other cells	80
LDV, LDVP, GPEILDVPST	Fibronectin	integrin α_4 β_1,	Adhesion	107,113
REDVDY, GREDVY	Fibronectin	integrin α_4 β_1,	Endothelial cell Adhesion	102,114
PHSRN	Fibronectin	integrin α_5 β_1,	cell adhesion, invasion and wound healing.	88,105
IKVAV, CIKVAV, CSRAKQAASIKVAVSADR	Laminin	110kDa laminin receptor protein	Neurite extension, viability	81,106,112, 115-116
PDSGR	Laminin	67kDa laminin binding protein	Adhesion	88
RNIAEIIKDI	Laminin	cellular prion protein	neuronal adhesion and neurite extension	112
KHIFSDDSSE	Neural cell adhesion molecules	Specific receptors on the particular type of neuronal cells	Astrocyte adhesion	108
FHRRIKA	Heparin binding domain	putative heparin-binding	Improve osteoblastic mineralization	117
KRSR	Heparin binding domain	Mainly integrins	Osteoblast adhesion	117
LRE	Laminin	integrin	adhesion of neurons	118
VTXG	Thrombospondin		Adhesion of platelets	119
HHLGGAKOAGDV	Fibrinogen	α_{IIb} β_3	platelets attachment	120
RKGSGRR/KKTR	Thrombospondin-1	HSPG-LRP-gp330 syndecan sulphated glycolipid	endocytosis	121
KQAGDV	Fibronectin	integrin	Smooth muscle cell adhesion	122
GFOGER	Collagen -1	Integrin α_2 β_1	Cell adhesion	123
VAPG(VGVAPG)	Elastin	67kDa protein(unknown smooth muscle cell receptor)	generate directed cell movements	124
MKKTRG	TSP-1	Decorin	Inhibits cell adhesion	125
RFK	TSP-1	Latent TGF-β	Activation of latent TGF-β	126
GEFYFDLRLKGDK	Collagen IV	integrins	Cell adhesion	108
WQPPRARI	Heparin-binding domain of fibronectin	Syndecan,heparin	enhance focal adhesion formation	109

LQVQLSIR	Laminin-1	Syndccan, heparin	Cell attachment and metastasis	127
GVQxR	TSP-1	CD36	migratory inhibition of TSP1	128
TWYKIAFQRNRK	Laminin-2	α_6 $\beta_1$integrin	Cell adhesion	129
KNRLTIELEVRT	laminin α2 chain	Syndccan-1	promotes cell adhesion and neurite outgrowth	130
LALERKDHSG	Thrombospondin-1	α_6 $\beta_1$integrin	increases macrophage recruitment and tumor cytotoxicity.	131
KAFAKLAARLYRKA	Anti –thrombin III	Heparin	Controls binding affinity and selectivity	132
ONV	Thrombospondin-1	α_3 $\beta_1$integrin	Cell adhesion to TSP-1 haemostasis	133
IDAPS	Fibronectin	α_4 β_1	Cell adhesion	134
CSVTCG	TSP-1	CD36	Anti-angiogenesis cell adhesion; involved in TSP-1 mediated tumor cell adhesion and metastasis	135
WSHWSPW	TSP-1	Protein glycosaminoglycan	Activation of latent TGF-β; Regulation of Angiogenesis and Tumor Growth	136

Table 2- 2 Different versions of diblock proteins with bioactive domains

Peptide Name	Peptide Length(aa)	Peptide M.W.(Da)	PI	Ext. co.	Peptide Sequence
BSS-spacer	73	7838	4.77	6970	M D Y E I K F H G D G D N F D L N L D D S G G D L Q L Q I R G P G G R V Q V H I H S S S G K V D F H V N N D G G D V E V K M H P W G S T S G S G T
BSS-**RGDS**	77	8253	4.80	6970	M D Y E I K F H G D G D N F D L N L D D S G G D L Q L Q I R G P G G R V Q V H I H S S S G K V D F H V N N D G G D V E V K M H P W G S T S G S G T **R G D S**
BSS-**YIGSR**	81	8684	4.80	8250	M D Y E I K F H G D G D N F D L N L D D S G G D L Q L Q I R G P G G R V Q V H I H S S S G K V D F H V N N D G G D V E V K M H P W G S T S G S G T D P G **Y I G S R**
BSL-spacer	84	8824	5.05	6970	M D Y E I K F H G D G D N F D L N L D D S G G D L Q L Q I R G P G G R V Q V H I H S S S G K V D F H V N N D G G D V E V K M H P W G S T S G S G K P G S G E G S T K G T
BSL-**RGDS**	88	9239	5.07	6970	M D Y E I K F H G D G D N F D L N L D D S G G D L Q L Q I R G P G G R V Q V H I H S S S G K V D F H V N N D G G D V E V K M H P W G S T S G S G K P G S G E G S T K G T **R G D S**
BSL-**YIGSR**	92	9670	5.07	8250	M D Y E I K F H G D G D N F D L N L D D S G G D L Q L Q I R G P G G R V Q V H I H S S S G K V D F H V N N D G G D V E V K M H P W G S T S G S G K P G S G E G S T K G T D P G **Y I G S R**

Table 2- 3 Different versions of diblock proteins with inorganic templating sequences

	Peptide Name	Peptide Length(aa)	Peptide M.W.(Da)	PI	Ext. co.	Peptide Sequence
Peptides with HA-binding domain	BSL-**5mer**	89	9385	4.77	6970	M D Y E I K F H G D G D N F D L N L D D S G G D L Q L Q I R G P G G R V Q V H I H S S S G K V D F H V N N D G G D V E V K M H P W G S T S G S G K P G S G E G S T K G T **E S Q E S**
	BSL-**7mer**	91	9568	5.46	6970	M D Y E I K F H G D G D N F D L N L D D S G G D L Q L Q I R G P G G R V Q V H I H S S S G K V D F H V N N D G G D V E V K M H P W G S T S G S G K P G S G E G S T K G T **M L P H H G A**
	BSL-**9mer**	93	9843	4.65	6970	M D Y E I K F H G D G D N F D L N L D D S G G D L Q L Q I R G P G G R V Q V H I H S S S G K V D F H V N N D G G D V E V K M H P W G S T S G S G K P G S G E G S T K G T **Q E S Q S E Q D S**
Peptide with silver-binding domain	BSL-**Ag4**	96	10203	5.07	8480	M D Y E I K F H G D G D N F D L N L D D S G G D L Q L Q I R G P G G R V Q V H I H S S S G K V D F H V N N D G G D V E V K M H P W G S T S G S G K P G S G E G S T K G T **N P S S L F R Y L P S D**

2.2.2 Generation of Recombinant DNA Encoding Diblock Proteins

To construct the recombinant DNA sequences encoding diblock proteins, the DNA fragment encoding β-sheet #17 was first annealed and amplified by PCR, then cloned into PQE-30 vector via EcoRI/BamHI restriction sites. The resulting clone was named vector PQE-β-sheet. Subsequently, DNA fragment encoding either short spacer or long spacer was ligated into the vector PQE-β-sheet via BamHI/KpnI restriction sites, resulting in vector PQE-BSS-spacer and PQE-BSL-spacer. Next, DNA fragment encoding bioactive sequence RGDS or YIGSR was ligated into vector PQE-BSS-spacer and PQE-BSL-spacer via KpnI/PstI restriction sites. After that, the whole constructs were cloned into pET-21d via NcoI/EcoRI restriction sites to generate vectors pET-21d(+)-BSS-spacer, pET-21d(+)-BSS-RGDS, pET-21d(+)-BSS-YIGSR, pET-21d(+)-BSL-spacer, pET-21d(+)-BSL-RGDS and pET-21d(+)-BSL-YIGSR. Inorganic templating sequences were cloned into pET-21d(+)-BSL-spacer vector via KpnI/ EcoRI restriction sites to generate vectors PET-21d(+)-BSL-5mer, PET-21d(+)-BSL-7mer, PET-21d(+)-BSL-9mer and PET-21d(+)-BSL-Ag4. The detailed methods to construct recombinant DNA are described in chapter 2.3. The whole gene maps are presented in Figure 2-8. The DNA sequences encoding β-sheet #17, short spacer, long spacer, RGDS and YIGSR are given in Table 2-4.

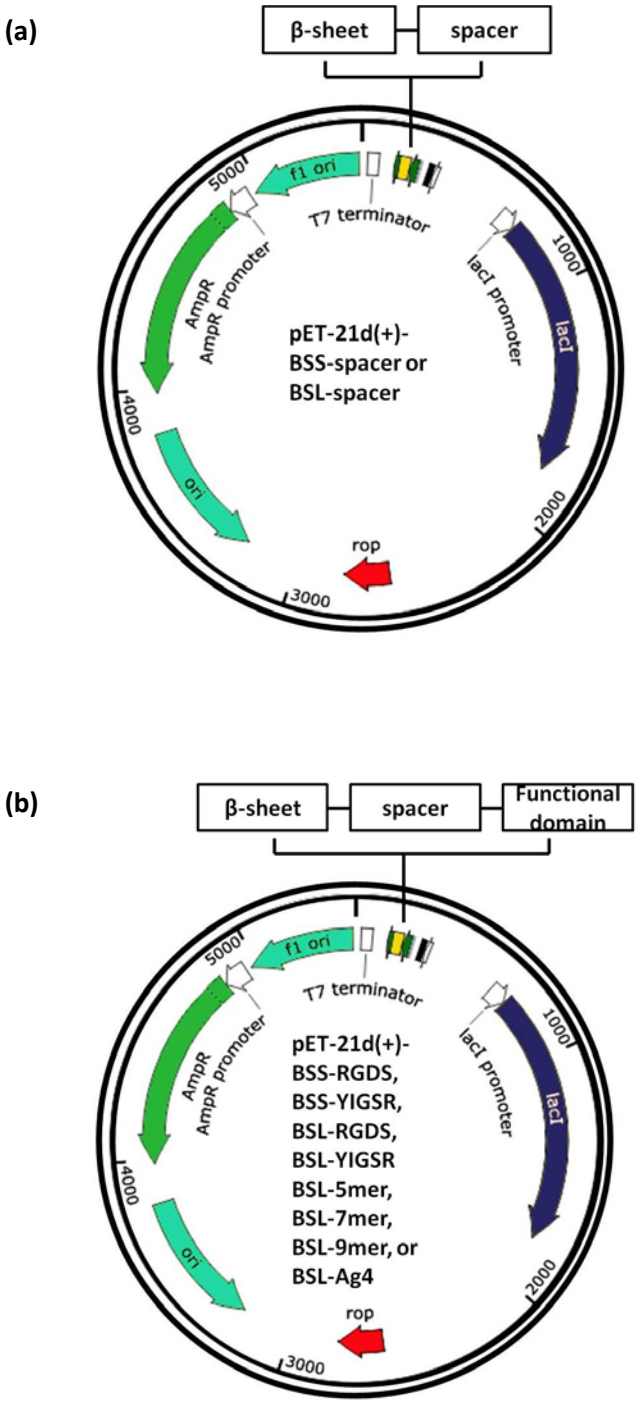

Figure 2-8 (a) The recombinant DNA map of BSS-spacer or BSL-spacer; (b) The recombinant DNA map of BSS-RGDS, BSS-YIGSR, BSL-RGDS, BSL-YIGSR, BSL-5mer, BSL-7mer, BSL-9mer or BSL-Ag4.

Table 2-4 DNA sequences for β-sheet #17, short spacer, long spacer, and functional domains.

Fragment name	DNA Sequences
β-sheet #17	M D Y E I K F H G D G D N F D L N L D D S G G EcoRI 5'…aa ttc atg gat tac gaa atc aaa ttt cat ggc gac ggt gat aac ttc gac ctg aat ctg gat gac agc ggc ggt…3' 3'… g tac cta atg ctt tag ttt aaa gta ccg ctg cca cta ttg aag ctg gac tta gac cta ctg tcg ccg cca…5' D L Q L Q I R G P G G R V Q V H I H S S S G K V D 5'… gat tta cag ctg caa att cgt gga cca ggt ggt cgt gtg cag gtt cac att cat agt tct agc ggc aag gtc gat…3' 3'… cta aat gtc gac gtt taa gca cct ggt cca cca gca cac gtc caa gtg taa gta tca aga tcg ccg ttc cag cta…5' F H V N N D G G D V E V K M H P W BamHI 5'…ttt cac gta aac aat gac ggt ggc gat gtg gaa gtt aaa atg cat ccg tgg g …3' 3'…aaa gtg cat ttg tta ctg cca ccg cta cac ctt caa ttt tac gta ggc acc cct ag…5'
Short spacer	G S T S G S G T BamHI KpnI 5'…ga tcc acc tct ggg tca ggt ac…3' 3'…g tgg aga ccc agt c…5'
Long spacer	G S T S G S G K P G S G E G S T K G T BamHI KpnI 5'…ga tcc acc tct ggg tca ggc aaa ccg ggt agc ggc gaa ggc tcg acg aag ggt ac…3' 3'…g tgg aga ccc agt ccg ttt ggc cca tcg ccg ctt ccg agc tgc ttc c…5'
RGDS	R G D S stop KpnI PstI 5'… c cgt ggt gat agc taa ctg ca …3' 3'…ca tgg gca cca cta tcg att g…5'
YIGSR	D P G Y I G S R Stop KpnI PstI 5'…c gat cca ggt tac atc ggc agc cgt taa ctg ca…3' 3'…ca tgg cta ggt cca atg tag ccg tcg gca att g…5'
ESQES	E S Q E S Stop KpnI EcoRI 5'…c gaa agc cag gaa agc taa g …3' 3'…ca tgg ctt tcg gtc ctt tcg att ctt aa …5'

MLPHHGA	M L P H H G A Stop KpnI EcoRI 5'…c atg ctg ccg cat cat ggc gcg taa g …3' 3'…ca tgg tac gac ggc gta gta ccg cgc att ctt aa …5'
QESQSEQDS	Q E S Q S E Q D S Stop KpnI EcoRI 5'…c cag gaa agc cag agc gaa cag gat agc taa g …3' 3'…ca tgg gtc ctt tcg gtc tcg ctt gtc cta tcg att ctt aa …5'
AG4	N P S S L F R Y L P S D Stop KpnI EcoRI 5'…c aac ccg agc agc ctg ttt cgt tat ctg ccg agc gat taa g …3' 3'…ca tgg cta ggt cca atg tag ccg tcg gca att aat tc…5'

2.3 Methodology for Creating Diblock Proteins

2.3.1 Construction of DNA Plasmids for Protein Expression

2.3.1.1 Fragment-Vector Enzymatic Ligation

The fragment-vector enzymatic ligation technique is a basic method to clone foreign genes into expression vectors. The general method is described as follows [137]. A foreign DNA fragment is first obtained either by annealing equal molar forward and reverse DNA oligonucleotides or by PCR of genes from other vectors. It is then digested with two different restriction enzymes to generate noncomplementary protruding termini, and treated with the T4 polynucleotide kinase (T4 PNK) to add phosphate groups to the oligos for ligation. The expression vector is also digested with these two enzymes to generate termini

compatible with the termini of the foreign DNA fragment. The digested DNA fragment and vector are visualized on a TAE-agarose gel and extracted by a gel extraction kit. The DNA fragment encoding the desired gene is ligated into the digested expression vector at a molar ratio of 3:1 using 1 unit of the T4 DNA ligase (NEB) in a total volume of 20 µl. The ligation mixture is then incubated at 16 °C for 16 hours. A ligation negative control sample is also prepared by mixing the digested expression vector with the same volume of ddH_2O instead of the DNA fragment.

In our experiment, the DNA fragment encoding β-sheet #17 was first inserted into PQE-30 vector via EcoRI/BamHI restriction sites. The resulting clone was named vector PQE-β-sheet. Subsequently, the DNA fragment encoding either the short spacer or the long spacer was ligated into the vector PQE-β-sheet via BamHI/KpnI restriction sites, resulting in vector PQE-BSS-spacer and PQE-BSL-spacer. Next, the DNA fragment encoding bioactive sequence either RGDS or YIGSR was inserted into the vector PQE-BSS-spacer and PQE-BSL-spacer via KpnI/PstI restriction sites, respectively. After that, the whole constructs were cloned into the vector pET-21d via NcoI/EcoRI restriction sites to generate a set of DNA plasmids including PET-21d(+)-β-sheet, PET-21d(+)-BSS-spacer (β-sheet-short spacer), PET-21d(+)-BSL-spacer (β-sheet-long spacer), PET-21d(+)-BSS-RGDS (β-sheet-short spacer-RGDS), PET-21d(+)-BSL-RGDS (β-sheet-long spacer-RGDS), PET-21d(+)-BSS-YIGSR (β-sheet-short spacer-YIGSR), and PET-21d(+)-BSL-YIGSR (β-sheet-long spacer-YIGSR).

The DNA fragments encoding HA-binding domains (ESQES, MLPHHGA, QESQSEQDS) and a silver-binding domain (NPSSLFRYLPSD) were also cloned into the

PET-21d(+)-BSL-spacer vector via kpnI/ EcoRI restriction sites using the fragment-vector enzymatic ligation technique. The resulting DNA plasmids were named as PET-21d(+)-BSL-5mer(β-sheet-long spacer-5mer), PET-21d(+)-BSL-7mer (β-sheet-long spacer-7mer), PET-21d(+)-BSL-9mer (β-sheet-long spacer-9mer) and PET-21d(+)-BSL-Ag4 (β-sheet-long spacer-AG4).

2.3.1.2 Transformation of DNA Plasmids into XL1-Blue Competent Cells

The reaction mixture, enriched with designed DNA, was incubated with 50 µl of XL1-blue competent cells in a 1.5 ml microcentrifuge tube on ice for 30 min. The tubes were then heat-shocked for 45 seconds in a water bath at 42 °C before being put back on ice for 2 min. 500µl LB media (without antibiotics) were then added to each mixture and the mixture was incubated at 37 °C for 1 hour. Since pET 21d+ is ampicillin-resistant and XL 1-blue cell is tetracycline-resistant, 100 µl of culture was spread onto an LB agar plate containing 100 µg/ml ampicillin and 12.5 µg/ml tetracycline. The plates were incubated overnight at 37 °C.

2.3.1.3 Recombinant DNA Screening

DNA screening, using colony PCR and double digestion of sequences, was used to identify the positive recombinant DNA sequences. Colony PCR used a single colony from an agar plate as the template. T7 promoter and T7 Terminator primers were formulated for up to 96 reactions and aliquoted into PCR tubes. The PCR annealing temperature was set at 56^{o} C to ensure high specificity. PCR products were then loaded onto a 2% TAE-agarose gel

for visualization. Positive colonies identified by colony-PCR screening were inoculated in 10 ml LB medium with 100 µg/ml ampicillin and 12.5 µg/ml tetracycline and grown overnight at 37 °C in a shaker-incubator. Plasmid DNA was then isolated from 10 ml of the overnight culture by using a Wizard® plus SV minipreps DNA purification system (Promega, Madison, USA). Simultaneous double digestion with KpnI and EcoRI was set up in the same way as described previously to confirm the positive samples. Confirmed positive samples containing 10 µl of 12.5 ng/µl of DNA and 5 µl of 2 µM T7 promoter and 5 µl of T7 Terminator primer in a total volume of 15uL were sent to OHRI Stemcore laboratories DNA sequencing Facility to identify clones bearing the desired genes without undesired mutations.

2.3.1.4 Transformation of Recombinant Protein Vectors into Expression Cells

The pET-21d+ vector containing the genes was transformed into the calcium chloride treated competent cells of the E. coli expression strain BLR, and the transformants were selected on plates containing both 100 µg/ml ampicillin and 12.5 µg/ml tetracycline due to the ampicillin-resistance of pET 21d+ vectors and tetracycline-resistance of BLR cells.

2.3.2 Protein Expression in E. coli

Protein expression was performed both in small and large scales. Small scale expression in shake flasks was carried out at 37 °C in 1L of LB media containing 100 µg/ml ampicillin and 12.5 µg/ml tetracycline, and induced with isopropyl-D-thiogalactoside (IPTG)

(final concentration 1 mM) for a period of 4 h when the optical density at 600 nm (OD_{600}) approached 0.8. Cells were then harvested by centrifugation at 8000 g for 15 minutes at 4 °C. Large scale expression (5 L) was performed at 37 °C and with 35% of oxygen saturation using a BioFlo 110 Modular Benchtop Fermentor (New Brunswick Scientific Co. Inc., Enfield, USA). The media for 5 L protein expression consisted of the following: 50 g glucose, 100 g yeast extract, 10 g $(NH_4)_2HPO4$, 33.75 g KH_2PO_4, 4.25 g citric acid, 3.5 g $MgSO_4 \cdot 7H_2O$, 25 ml trace metals, 500 mg Ampicillin (100 mg/ml), 62.5 mg tetracycline (12.5mg/ml), and 0.5 ml antifoam. A feed solution containing glucose (500 g/L), yeast extract (100 g/L), MgSO4·7H2O (15 g/L), ampicillin (100 mg/L), and tetracycline (12.5 mg/L) was automatically added into the fermentor as needed to maintain pH neutral after about 5 h of fermentation. Cultures were induced by IPTG for a period of 4 h when the OD_{600} reached approximately 15. Cells were then harvested by centrifugation at 8000 g for 30 minutes at 4 °C.

2.3.3 Protein Purification

Proteins were first purified using a well-established inclusion body purification method as follows [71]. After being harvested by centrifugation, the pellet was fully re-suspended in a buffer solution with 50 mM Tris-HCl, PH 8.0, 25%sucrose (w.t.), and 1mM EDTA. Cells were then subjected to three freeze-thaw cycles and sonicated for 2 min. The suspension was incubated by stirring at room temperature for 30 min after lysozyme was added at a final concentration of 0.5 mg/ml. Subsequently, $MgCl_2$, $MnCl_2$ and DNaseI were added with final concentration of 10 mM, 1 mM, 20 ug/ml, respectively, and the suspension was incubated at room temperature for another 30 min. Inclusion body wash buffer

containing 0.2 M NaCI, 1% Deoxycholic Acid, I% IGEPAL CA-630 , 20 mM Tris-HCI, 0.2 mM EDTA was then added for another 30 min of incubation at room temperature, and the inclusion body was separated from soluble portion by centrifugation at 20,000 rpm for 15 min. The inclusion body was further washed by dH_2O and re-solubilized in dH_2O at pH11. The re-solubilized inclusion body was further purified with the gel filtration method under denaturing condition using Sephadex^{TM} G-50 Fine medium (GE healthcare, Toronto, Canada). The expression and purification of proteins were checked by SDS-PAGE. Pure proteins were then loaded into Spectra/Pro dialysis tubing (1 K MWCO, Fisher Scientific, Ottawa, ON, Canada), dialyzed again against MiliQ water (above 15 mΩ) at pH 11 for 48 h, and then lyophilized.

2.3.4 MALDI-TOF and Amino Acid Composition Analysis

Molecular weights of proteins were determined by matrix-assisted laser desorption ionization-time-of-flight mass spectroscopy (MALDI-TOF microflex, Bruker Daltonics Ltd. , Canada). To determined protein molecular weight by MALDI-TOF, samples were prepared at concentrations of 1 mM, 100 µM, 10 µM and 1 µM to obtain high quality signals. MALDI matrix was prepared by dissolving 25 mg sinapinic acid in 1 ml of 50% acetonitrile, 50% proteomics grade water and 0.1% TFA. Samples and Matrices were then mixed in a 1:1 ratio, and applied onto a MSP 96 target ground steel sample plate. Subsequently, the mixtures were dried and co-crystallized through evaporation at room temperature. Finally, the molecular weights were studied with MALDI-TOF.

Sequence information for the various diblock protein designs were obtained using Amino acid composition analysis (AAA). Samples for AAA were prepared by excising corresponding bands from an SDS-PAGE gel. The excised gel bands were sent to W.M. Keck foundation biotechnology Resource Laboratory (Yale University, New Haven, USA) for amino acid analysis.

Chapter 3

Preparation and Characterization of Bioactive Diblock Proteins

3.1 Introduction

As discussed in chapter 2, the central objective of this study is to design and synthesize proteins for biofunctional interfaces based on a diblock motif which is composed of a surface-active, amphiphilic β-sheet structure ligated to a disordered and water soluble block named spacer with an end terminal bioactive domain. The focus of this chapter is on the biophysical properties of these diblock proteins. One of the most important questions relates to the structure of these proteins. Can the associating end of these proteins form β-sheet structures under ambient, physiological conditions? Does the water soluble disordered chain or bioactive domain affect the β-sheet structure of the associating end? Under what conditions do these β-sheet structures denature and adopt a disordered coil conformation? What are the denaturation (melting) temperature of these β-sheet domains and the free energy changes during the denaturation process? Several physical detection techniques including circular dichroism (CD), Fourier transform infrared spectroscopy (FT-IR), and differential scanning calorimetry (DSC) were used to find answers to these questions. In addition, analytical methods, including electrophoresis, MALDI mass spectroscopy, and

amino acid composition analysis, were used to confirm the sequence, molecular weight, and purity of the proteins.

CD spectroscopy is a widely used technique for assessment of protein secondary structure in solution due to its utility for rapid and facile data collection. It is a form of light absorption spectroscopy which measures the differential absorption of right-hand and left-hand circularly polarized components [138]. There are unambiguous differences in CD spectra of various protein secondary structures, including α-helix, parallel and antiparallel β-sheet and random coils, which are qualitatively demonstrated by analysis of CD spectra between 260 and 180 nm [139,140]. The mean residue ellipticity (defined precisely below) is proportional to the difference in absorbance between left (A_L) and right (A_R) circularly polarized light, as measured by a spectropolarimeter. Figure 3-1 shows the different forms of the mean residue ellipticity of common protein secondary structures. α-helical structures are characterized by negative bands between approximately 203 nm and 240 nm with two minima near 209 nm and 222 nm. The CD spectra for β-sheets show a minimum band between 210 nm and 225 nm and a maximum band between 190 nm and 200 nm. The CD spectra for random coils also display a strong negative band at about 200 nm, and a weak positive or negative band above 210 nm [141].

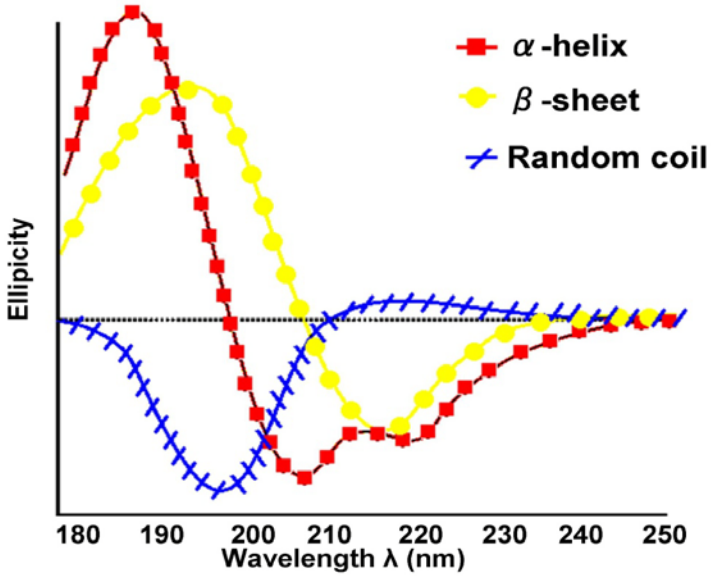

Figure 3-1 Schematic diagram of the various forms of the mean residue ellipticity taken for common protein secondary structures.

While CD spectroscopy has certain advantages for the characterization of protein secondary structure, it has several limitations. The main one is the difficulty for quantitative determination of secondary structure content. A complementary approach for study of protein secondary structure, Fourier transform infrared spectroscopy (FTIR), provides several prominent advantages including high resolution, sensitivity, high signal-to-noise ratio (S/N) and frequency accuracy, which in term allow for the possibility of quantitative study of secondary structure [142]. It also allows for studying the secondary structure of adsorbed monolayers of the diblock proteins. FTIR spectroscopy is a technique that simultaneously collects infrared spectra of absorption, emission and photoconductivity of materials in a wide spectral range. Proteins respond to IR in nine characteristic absorption bands including amide A, B and amide I-VII bands in the infrared region [141]. The amide I (~1600-1690 cm^{-1}) bands have been widely used for protein structure studies. Secondary structures of proteins can be characterized since α-helix, β-sheet, turn and random coil

structures present different amide bond geometric orientations, thereby allowing for different vibrational frequencies and distinct IR signals.

Differential scanning calorimetry (DSC) is generally accepted as a thermal analysis technique that has contributed significantly to understanding of temperature-induced transitions in biological systems and the thermodynamic mechanisms underlying those transitions. For example, DSC studies of protein and nucleic acid folding-unfolding transitions have revealed not only thermodynamic properties of these transitions, but also the complexity of the unfolding process [143,144]. DSC measures the changes of apparent molar heat capacity related to phase transitions and chemical reactions as a function of temperature by monitoring heat flow during these processes and comparing this to heat flow in a reference cell maintained at the same temperature as the sample. In an endothermic process, more heat flows in the sample than in the reference; while in an exothermic process, less heat flows in the sample than in the reference. Subsequent manipulation of the difference in heat flow provides a complete thermodynamic characterization of a transition.

3.2 Characterization Methods for Diblock Proteins

3.2.1 Circular Dichroism

CD spectra were measured for 20 μM solutions of diblock proteins in 10 mM phosphate buffer at pH 7.5 and in 10mM phosphate buffer with 1 M NaCl buffer at pH 7.5 in a 1 mm path length quartz cuvette using a Jasco 710 spectropolarimeter (Jasco Inc., Easton, USA). Protein concentrations were calibrated using UV absorption spectroscopy with a

NanoDrop spectrophotometer (Thermo Scientific Inc., Mississauga, Canada) and molar extinction coefficients were estimated from primary sequences of proteins using software package Vector NTI(Life Technologies, Burlington, USA) . Two kinds of measurements were carried out. In a wavelength scan, the CD signal was collected as a function of wavelength at constant temperature. In a temperature scan, the CD signal was collected as a function temperature for a selected wavelength. Wavelength scans were conducted for each protein from 190nm to 250nm at a temperature of 20 °C to determine the global secondary structure profile of the protein in ambient conditions. Ten scans were recorded and averaged for each sample. Thermally induced denaturation of the β-sheet domains of the diblock proteins was studied by monitoring the CD signal at 217 nm (indicative of β-sheet content) as a function of temperature from 20 to 80 °C at a rate of 1 °C/min. Data were converted into mean residue molar ellipticity [θ] defined by the equation

$$[\theta] = \theta(\lambda)_{obs} / (10 \bullet c \bullet l \bullet n),$$

where $\theta_{obs}(\lambda) \propto (A_L(\lambda) - A_R(\lambda))$ is the observed ellipticity in mdeg, c is the protein concentration in M, *l* is the path length in cm, and n is the number of amino acid residues in a protein.

The fractional β-sheet contents of proteins were estimated using online SOMCD software [145]. The fraction of folded β-sheet structure at a given temperature T was determined from the melting curves using equation $f(T) = ([\theta_{Den}(T)] - [\theta(T)]) / ([\theta_{Den}(T)] - [\theta_{Nat}(T)])$, where [θ] is the observed ellipticity, $[\theta_{Den}]$ is the ellipticity of the denatured state of the proteins and $[\theta_{Nat}]$ is the ellipticity of the natively folded proteins, respectively.

3.2.2 Fourier Transform Infrared Spectroscopy

Monolayers formed by BSL-spacer and BSL-RGDS were evaluated by employing an attenuated total reflectance (ATR) accessory along with FTIR spectroscopy (FTS-40, Biorad, Mississauga, Canada) to provide high sensitivity. 20 μM of BSL-spacer and BSL-RGDS were prepared in 10 mM phosphate buffer (in D_2O) at pH 7.5. For each protein, 10 μL of sample was placed onto the diamond element of ATIR for a time interval of 25 min to form an adsorbed layer on the surface. Afterwards, the remaining liquid was carefully removed, and the diamond element was gently washed with 10 mM deuterated phosphate buffer at pH 7.5 three times to remove protein that was not part of the monolayer. Finally, the sample was dried under nitrogen and spectra were measured three times to obtain the average data.

3.2.3 Differential Scanning Calorimetry

DSC studies were carried out on solutions of the diblock proteins at various concentrations (from 20-600 μM) in 10 mM phosphate buffer at pH 7.5 using a nano-DSC III calorimeter (Calorimetry Sciences, Lindon, USA). The samples were first equilibrated with 10 mM phosphate buffer at pH 7.5 by overnight dialysis, followed by degassing. Heat rate scans were recorded at the rate of 1 °C/min as temperature increased from 10 to 90 °C, and 3 scans for each sample were measured to acquire an average value. Data were then analyzed with the software package Cpcalc (Calorimetry Sciences, Lindon, USA) to determine the dependence of heat capacity on temperature.

3.3 Results and Discussion

3.3.1 Preparation of Diblock Proteins

Diblock proteins were expressed and purified using the methods described in Chapter 2. Specifically, proteins recovered from inclusion bodies were purified using gel filtration with an FPLC (an AKTApurifier 100, GE Healthcare Life Sciences, Toronto, Canada). A representative FPLC gel filtration purification trace is shown in Figure 3-2a. Gel filtration, also known as size-exclusion chromatography, separates proteins according to their sizes with large molecules eluting faster than small ones. All fractions were visualized with SDS-PAGE gels and the fractions A8-A12, B12-B8, B2, B1, C3, C4 were demonstrated in Figure 3-2b. Proteins with the molecular weight of around 8 kDa were separated from other molecules starting at fraction A12, indicating that the desired pure proteins were collected after this fraction. Protein samples with fractions of A12, B12-B1, C1-C4 were then lyophilized. Figure 3-3 presents an overview of expression and purification of the diblock proteins. For 5L of E.coli protein expression with the bioreactor, all type of the BSL proteins yield around 400 mg proteins with the purity as shown in Figure 3-3. Comparison of pre-induction and post-induction samples demonstrates good expression of the proteins, and high-level purity of proteins (greater than 90%) was achieved using FPLC.

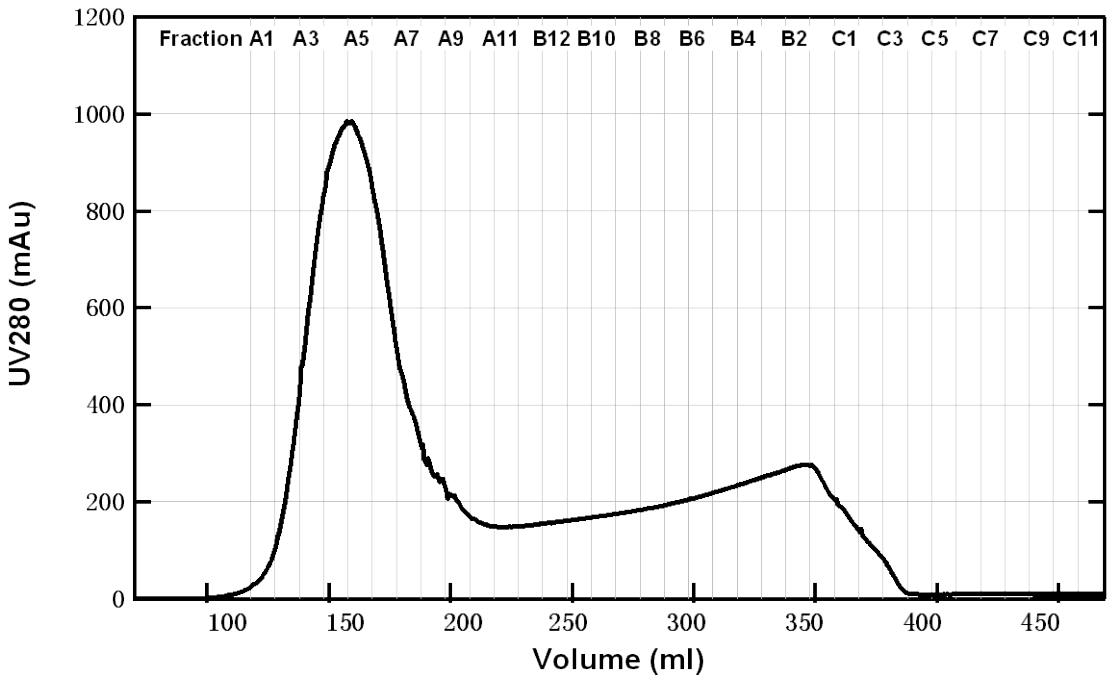

Figure 3-2a A representative purification trace of BSL-RGDS using Gel-filtration with FPLC. The fractions fractions A8-A12, B12-B8, B2, B1, C3, C4 were visualized with SDS-PAGE as in Figure 3-2b.

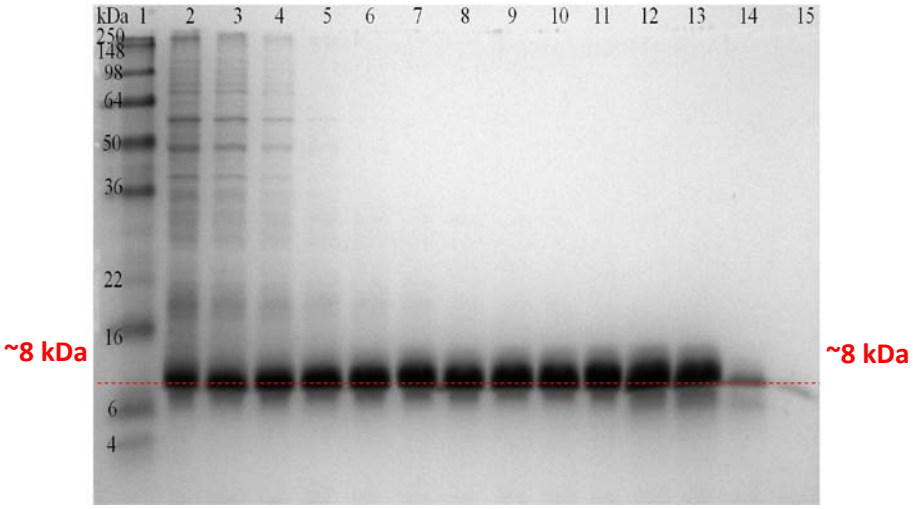

Figure 3-2b A representative coomassie stained SDS-PAGE gel to show purification of BSL-RGDS with Gel-filtration. lane1: SeeBlue Plus 2 standard. Lane2-15: fractions A8-A12, B12-B8, B2, B1, C3, C4 from FPLC gel filtration purification of BSL-RGDS.

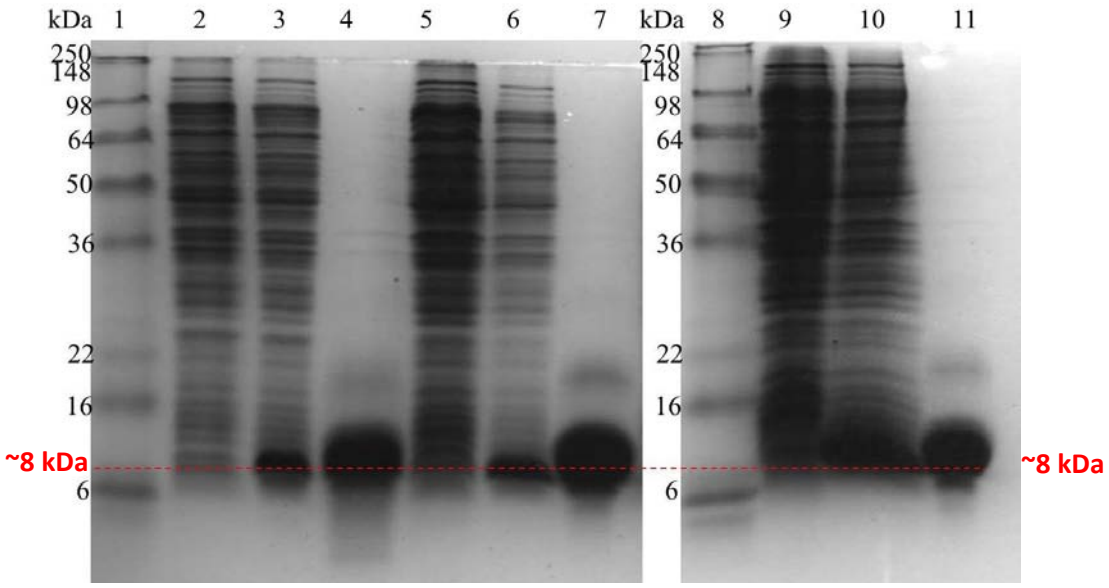

Figure 3-3a A coomassie stained SDS-PAGE gel to show the expression and purification of BSS-spacer (Lanes 2-4), BSS-RGDS (Lanes 5-7), and BSS-YIGSR (Lanes 9-11). The lanes contain the following: lane1,8: SeeBlue Plus 2 standard. Lane2: BSS-spacer pre-induction. Lane 3: BSS-spacer 4h post-induction. Lane 4: purified BSS-spacer. Lane5: BSS-RGDS pre-induction. Lane 6: BSS-RGDS 4h post-induction. Lane 7: purified BSS-RGDS. Lane9: BSS-YIGSR pre-induction. Lane 10: BSS-YIGSR 4h post-induction. Lane 11: purified BSS-YIGSR.

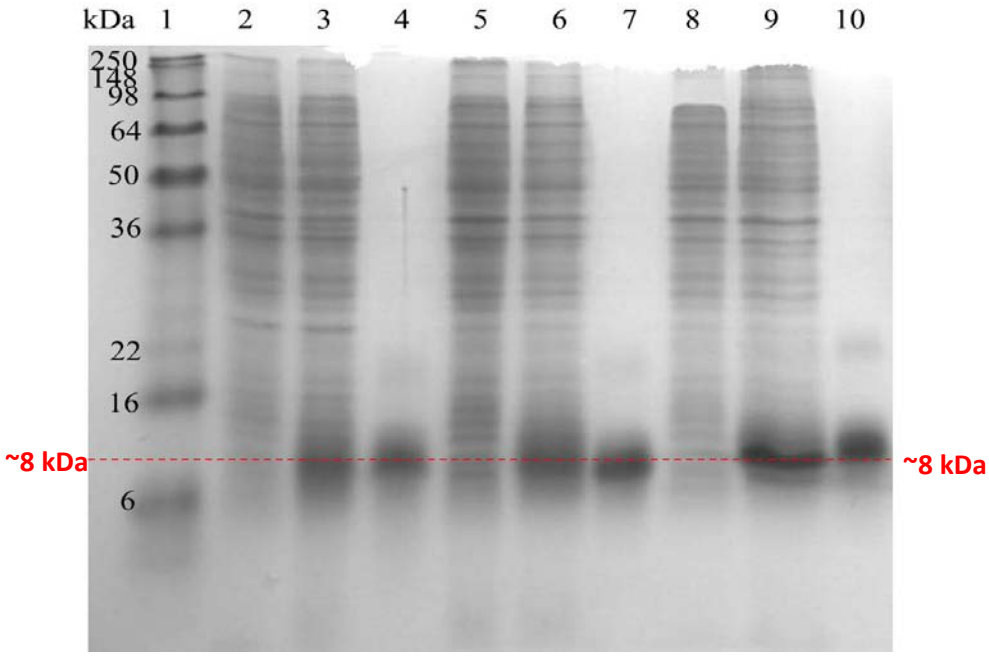

Figure3-3b A coomassie stained SDS-PAGE gel to show the expression and purification of BSL-spacer (Lanes 2-4), BSL-RGDS (Lanes 5-7), and BSL-YIGSR (Lanes 8-10). The lanes contain the following: lane1: SeeBlue Plus 2 standard. Lane2: BSL-spacer pre-induction. Lane 3: BSL-spacer 4h post-induction. Lane 4: purified BSL-spacer. Lane5: BSL-RGDS pre-induction. Lane 6: BSL-RGDS 4h post-induction. Lane 7: purified BSL-RGDS. Lane8: BSL-YIGSR pre-induction. Lane 9: BSL-YIGSR 4h post-induction. Lane 10: purified BSL-YIGSR.

The molar mass of the diblock proteins was verified using Matrix-assisted laser desorption mass spectrometry (MALDI). Results along with protein sequences are shown in Figure 3-4. BSS-spacer has a single, sharp peak at 7848 Da, BSS-RGDS has a single, sharp peak at 8271 Da, and BSS-YIGSR has a single, sharp peak at 8703 Da. Compared with the theoretical molecular weight calculated with software package Vector NTI (7838 Da for BSS-spacer, 8254 Da for BSS-RGDS, and 8684 Da for BSS-YIGSR), deviations were 0.1% for BSS-spacer and 0.2% for BSS-RGDS and BSS-YIGSR. For BSL-spacer, the dominant

peak is at 8834 Da, with deviation of 0.1% from the Vector NTI theoretical value at 8824 Da. Likewise, deviation was 0.09% for BSL-RGDS with 9240 Da calculated with Vector NTI and 9247 Da measured with MALDI (in this case a secondary peak at 4623 in MALDI was due to doubly-charged ions). Finally, the molecular weight determined by MALDI for BSL-YIGSR was 9688 Da, which is within 0.2% of its expected theoretical value of 9670 Da. The MALDI results demonstrated that the synthesized proteins have almost identical molecular mass as designed.

The amino acid composition of the diblock proteins was analyzed by the W.M. Keck Foundation Biotechnology Resource Laboratory at Yale University. The results shown in Table 3-1 demonstrated the expected compositions of proteins with acceptable errors. Together, the MALDI results and amino acid analysis indicated that the synthesized proteins had the sequences that were intended by design. Therefore, subsequent characterization of their physical properties was carried out.

BSS-spacer:

M D Y E I K F H G D G D N F D L N L D D S G G D L Q L Q I R G P G G R V Q V H I H S S S G K V D F H V N N D G G D V E V K M H P W *G S T S G S G T*

Length= 73aa, MW=7838Da, PI= 4.77

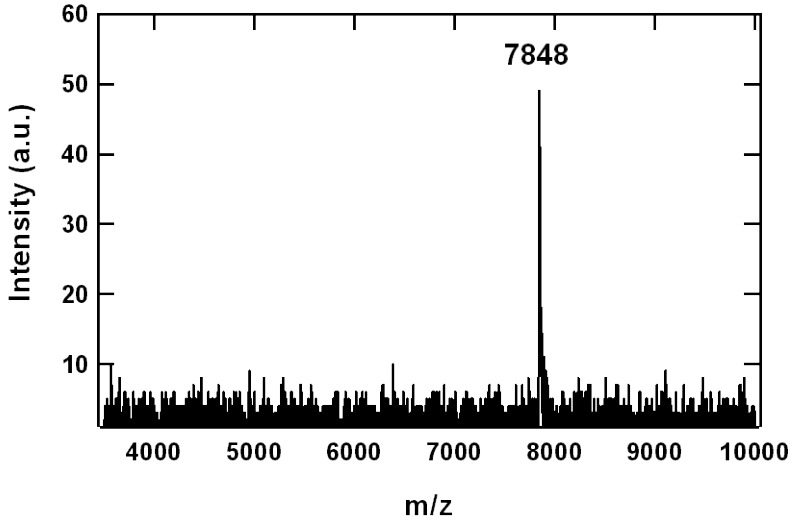

Figure 3-4a Sequence and MALDI spectrograph of BSS- spacer with a significant peak of 7848.

BSS-RGDS:

M D Y E I K F H G D G D N F D L N L D D S G G D L Q L Q I R G P G G R V Q V H I H S S S G K V D F H V N N D G G D V E V K M H P W *G S T S G S G T* **R G D S**

Length= 77aa, MW=8254Da, PI=4.80

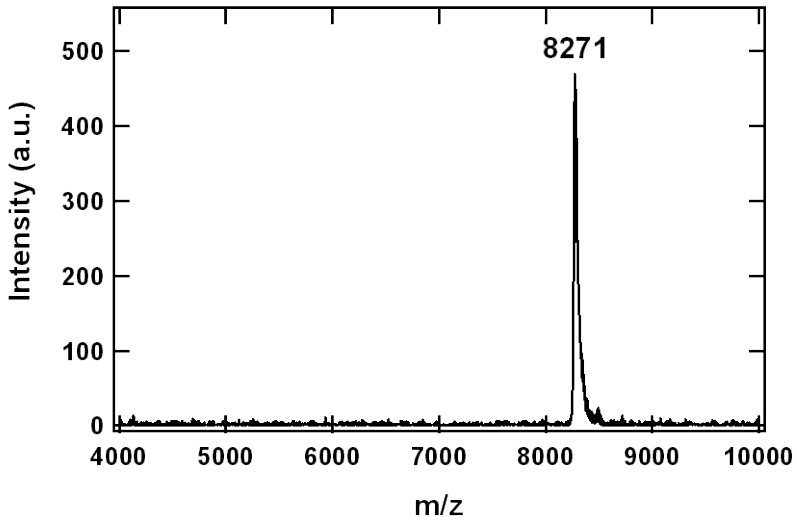

Figure 3-4b Sequence and MALDI spectrograph of BSS-RGDS with a significant peak of 8271.

BSS-YIGSR:

M D Y E I K F H G D G D N F D L N L D D S G G D L Q L Q I R G P G G R V Q V H I H S S S G K V D F H V N N D G G D V E V K M H P W *G S T S G S G T* D P G **Y I G S R**

Length= 81aa, MW=8684Da, PI=4.80

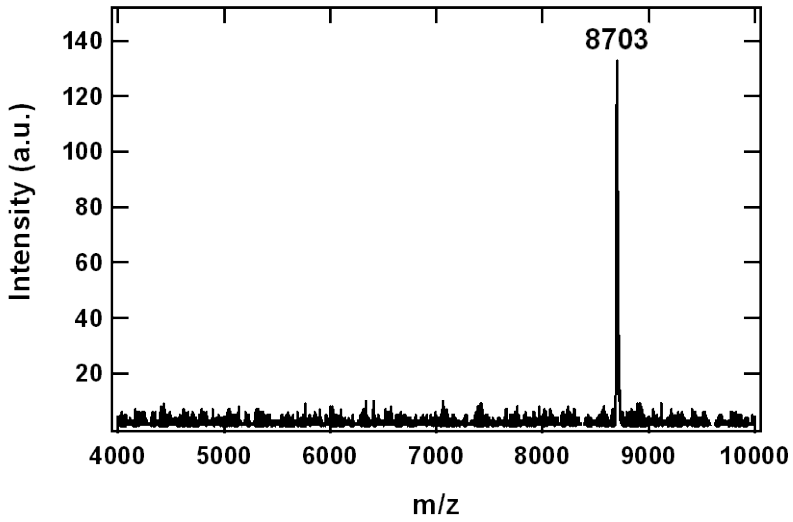

Figure 3-4c Sequence and MALDI spectrograph of BSS- YIGSR with a significant peak of 8703.

BSL-spacer:

M D Y E I K F H G D G D N F D L N L D D S G G D L Q L Q I R G P G G R V Q V H I H S S S G K V D F H V N N D G G D V E V K M H P W *G S T S G S G K P G S G E G S T K G T*

Length=84aa, MW=8824Da, PI=5.05

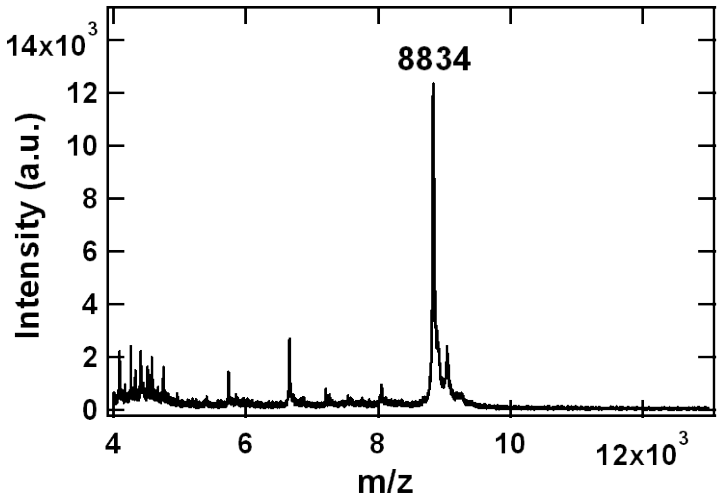

Figure 3-4d Sequence and MALDI spectrograph of BSL- spacer with a significant peak of 8834.

BSL-RGDS:

M D Y E I K F H G D G D N F D L N L D D S G G D L Q L Q I R G P G G R V Q V H I H S S S G K V D F H V N N D G G D V E V K M H P W *G S T S G S G K P G S G E G S T K G T* **R G D S**

Length=88aa, MW=9240Da, PI=5.07

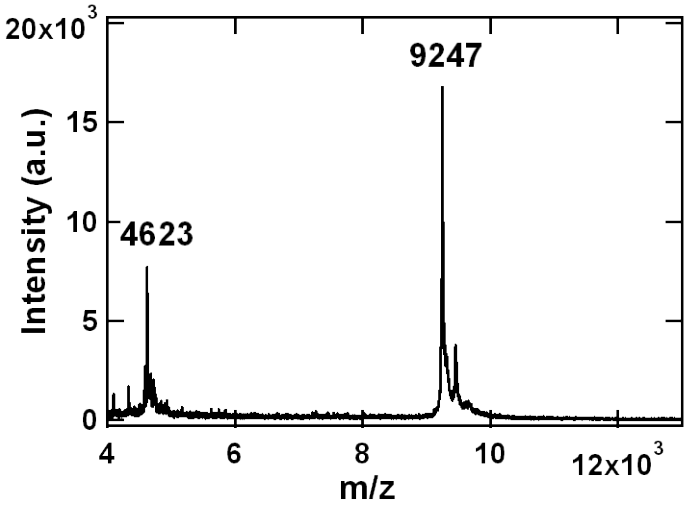

Figure 3-4e Sequence and MALDI spectrograph of BSL-RGDS with a significant peak of 9247.

BSL-YIGSR:

M D Y E I K F H G D G D N F D L N L D D S G G D L Q L Q I R G P G G R V Q V H I H S S S G K V D F H V N N D G G D V E V K M H P W *G S T S G S G K P G S G E G S T K G T* D P G **Y I G S R**

Length=92aa, MW=9670Da, PI=5.07

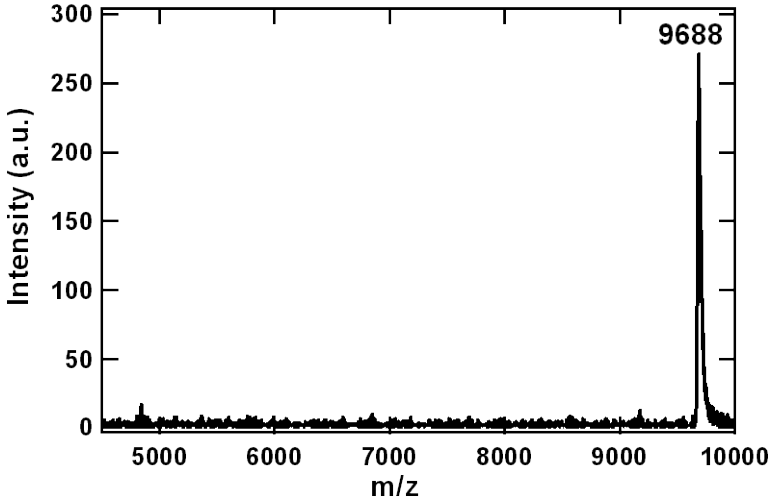

Figure 3-4f Sequence and MALDI spectrograph of BSL- YIGSR with a significant peak of 9688.

Table 3-1a Amino Acid Analysis of BSS-spacer (without cys and trp).

Amino acid	Mole %	Expected mole %	# Residues	Expected #residues
asx	20.1%	19.2%	15	14
thr	2.7%	2.7%	2	2
ser	7.4%	9.6%	5	7
glx	8.2%	6.9%	6	5
gly	19.3%	17.8%	14	13
val	8.6%	8.2%	6	6
met	1.7%	2.7%	1	2
ileu	4.1%	4.1%	3	3
leu	6.0%	5.5%	4	4
tyr	1.7%	1.4%	1	1
phe	4.0%	4.1%	3	3
lys	4.0%	4.1%	3	3
his	6.5%	6.9%	5	5
arg	2.9%	2.7%	2	2
pro	2.6%	2.7%	2	2
Total	99.8%	98.6%	72	72

Table 3-1b Amino Acid Analysis of BSS-RGDS (without cys and trp).

Amino acid	Mole %	Expected mole %	# Residues	Expected #residues
asx	16.8%	19.5%	13	15
thr	3.8%	2.6%	3	2
ser	8.0%	10.4%	6	8
glx	9.7%	6.5%	8	5
gly	17.2%	18.2%	13	14
val	8.2%	7.8%	6	6
met	1.4%	2.6%	1	2
ileu	3.9%	3.9%	3	3
leu	6.4%	5.2%	5	4
tyr	2.1%	1.3%	2	1
phe	3.8%	3.9%	3	3
lys	3.7%	3.9%	3	3
his	5.2%	6.5%	4	5
arg	4.1%	3.9%	3	3
pro	3.8%	2.6%	3	2
Total	98.1%	98.8%	76	76

Table 3-1c Amino Acid Analysis of BSS-YIGSR(without cys and trp).

Amino Acid	mole %	expected mole %	# residues	expected #residues
asx	19.8%	18.5%	16	15
thr	2.4%	2.5%	2	2
ser	7.5%	9.9%	6	8
glx	7.3%	6.2%	6	5
gly	19.9%	18.5%	16	15
val	8.0%	7.4%	6	6
met	1.5%	2.5%	1	2
ileu	4.9%	4.9%	4	4
leu	5.5%	4.9%	4	4
tyr	2.4%	2.5%	2	2
phe	3.8%	3.7%	3	3
lys	3.8%	3.7%	3	3
his	6.2%	6.2%	5	5
arg	3.8%	3.7%	3	3
pro	3.4%	3.7%	3	3
Total	100%	98.8%	80	80

Table 3-1d Amino Acid Analysis of BSL-spacer (without cys and trp).

Amino Acid	mole %	expected mole %	# residues	expected #residues
asx	17.7%	16.7%	15	14
thr	3.9%	3.6%	3	3
ser	9.8%	10.7%	8	9
glx	8.9%	7.1%	8	6
gly	21.1%	20.2%	18	17
val	7.2%	7.1%	6	6
met	1.1%	2.4%	1	2
ileu	3.4%	3.6%	3	3
leu	5.5%	4.8%	5	4
tyr	1.1%	1.2%	1	1
phe	3.2%	3.6%	3	3
lys	5.8%	5.9%	5	5
his	5.4%	5.9%	5	5
arg	2.5%	2.4%	2	2
pro	3.2%	3.6%	3	3
Total	99.8%	98.8%	86	83

Table 3-1e Amino Acid Analysis of BSL-RGDS (without cys and trp).

Amino Acid	mole %	expected mole %	# residues	expected #residues
asx	18.4%	17.1%	16	15
thr	3.7%	3.4%	3	3
ser	9.9%	11.4%	9	10
glx	8.0%	6.8%	7	6
gly	21.5%	20.5%	19	18
val	7.1%	6.8%	6	6
met	0.0%	2.3%	0	2
ileu	3.4%	3.4%	3	3
leu	5.1%	4.6%	5	4
tyr	1.2%	1.1%	1	1
phe	3.2%	3.4%	3	3
lys	5.8%	5.7%	5	5
his	5.6%	5.7%	5	5
arg	3.4%	3.4%	3	3
pro	3.8%	3.4%	3	3
Total	100%	99.0%	88	87

Table 3-1f Amino Acid Analysis of BSL-YIGSR (without cys and trp).

Amino Acid	mole %	expected mole %	# residues	expected #residues
asx	17.4%	17.1%	16	15
thr	3.3%	3.4%	3	3
ser	9.4%	11.4%	9	10
glx	7.4%	6.8%	7	6
gly	21.4%	20.5%	19	18
val	6.8%	6.8%	6	6
met	1.3%	2.3%	0	2
ileu	4.2%	3.4%	3	3
leu	4.7%	4.6%	5	4
tyr	2.0%	2.2%	2	2
phe	3.1%	1.1%	1	1
lys	5.6%	3.4%	3	3
his	5.5%	5.7%	5	5
arg	3.3%	5.7%	5	5
pro	4.4%	3.4%	3	3
Total	99.8%	97.8%	87	86

3.3.2 CD Studies of Secondary Structure of Diblock Proteins

CD wavelength scans were carried out for 20 μM of BSS-spacer, BSS-RGDS, BSS-YIGSR, BSL-spacer, BSL-RGDS and BSL-YIGSR in 10mM phosphate buffer at pH 7.5. Figures 3-5a,b show plots of the mean residue molar ellipticity [θ] of the BSS proteins (BSS-spacer, BSS-RGDS and BSS-YIGSR) at 20 ˚C as a function of wavelength λ in buffers with or without or 1 M NaCl. Figures 3-5c,d show the analogous plots for the BSL proteins (BSL-spacer, BSL-RGDS and BSL-YIGSR). The characteristic shapes of the wavelength scans resulted from a combination of the spectra generated by the β-sheet, random coil and turn secondary structural elements of the proteins. In particular, a pronounced single minimum at λ= 217 nm demonstrated that all BSS and BSL diblock proteins have robust β-sheet structures, presumably due to their associating block domains. The similarity of all the CD spectra suggests that the secondary structure of the associating block is not sensitive to the sequence composition of the soluble, disordered, bioactive block. This apparent independence of the two blocks is a desired feature of the designs: the biofunctional domains should not interfere with the assembly domain. From the point of view of secondary structure, this seems to be the case. Moreover, the data all show that added NaCl has the ability to strengthen β-sheet structure in the proteins relative to salt-free buffers (as indicated by the enhanced depth of the minimum at λ= 217 nm). This enhancement is presumably due to screening of repulsive electrostatic interactions in the β-sheet elements by elevated salt levels.

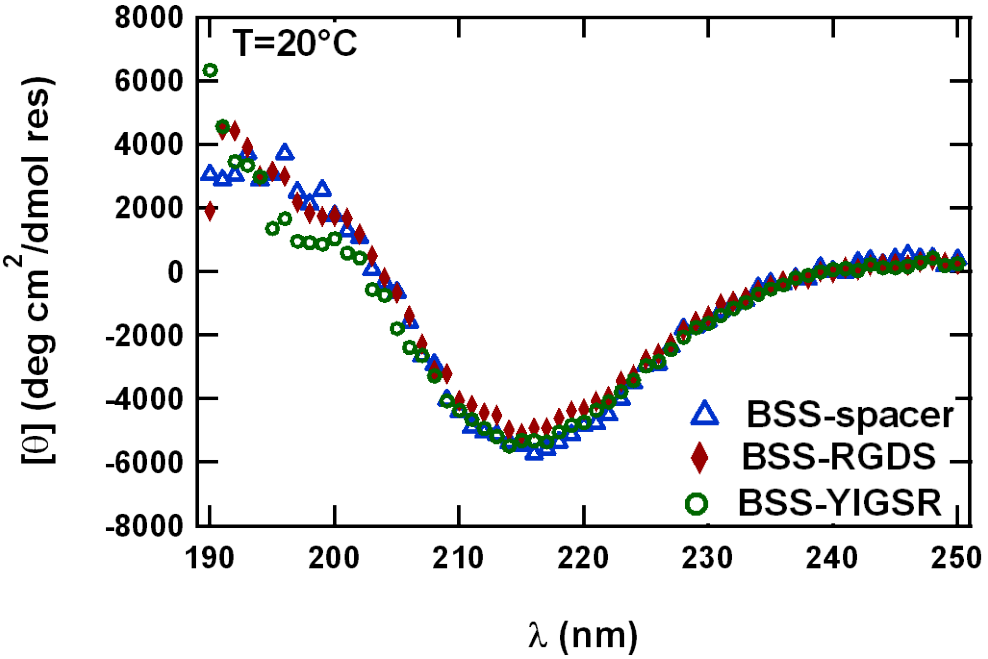

Figure 3-5a CD wavelength scans for 20 μM solutions of BSS proteins in 10 mM phosphate buffer, pH 7.5 at 20 °C.

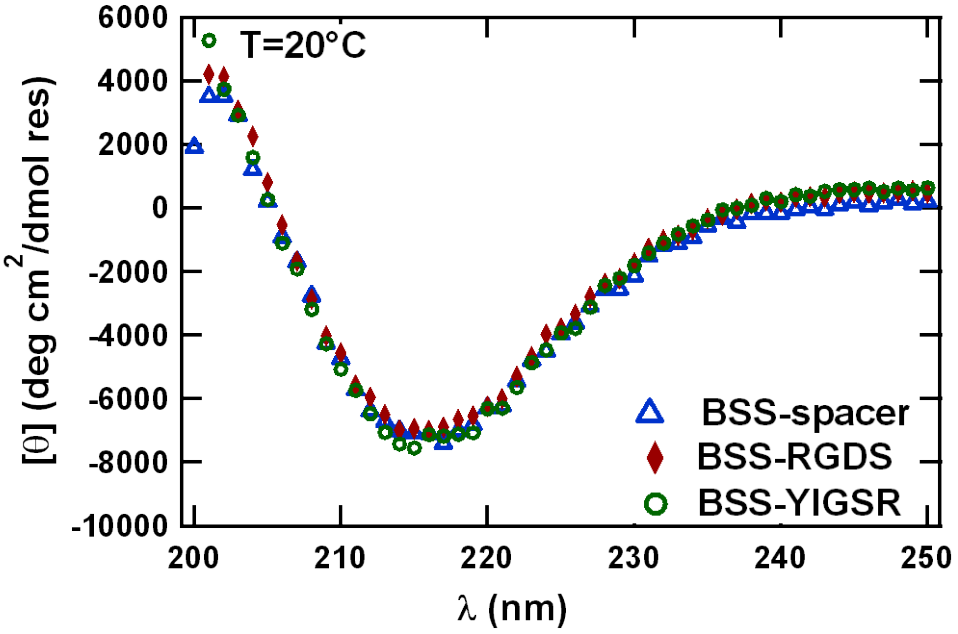

Figure 3-5b CD wavelength scans for 20 μM solutions of BSS proteins in 10 mM phosphate buffer, 1 M NaCl**,** pH 7.5 at 20 °C.

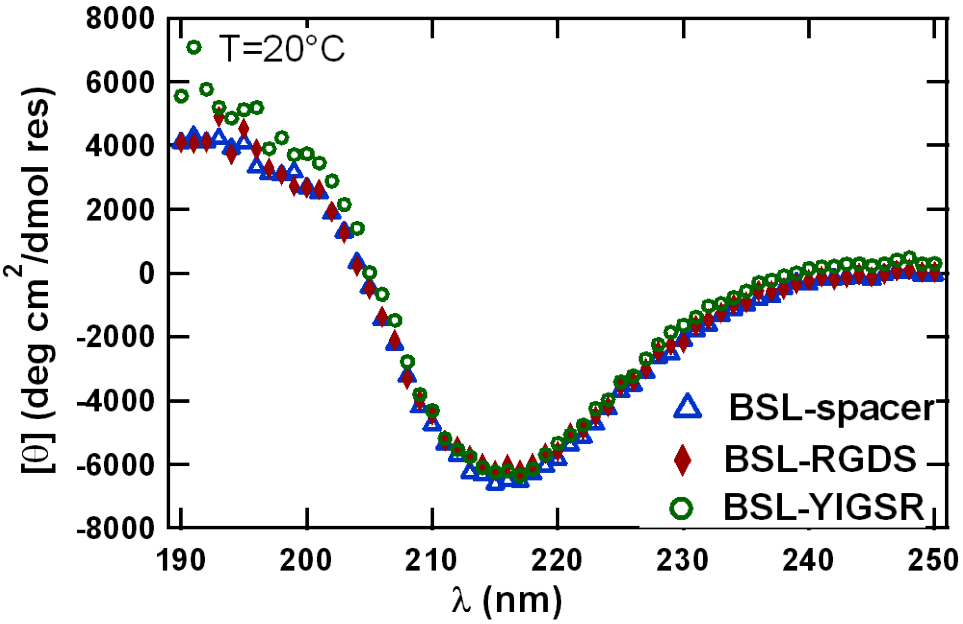

Figure 3-5c CD wavelength scans for 20 μM solutions of BSL proteins in 10 mM phosphate buffer, pH 7.5 at 20 °C.

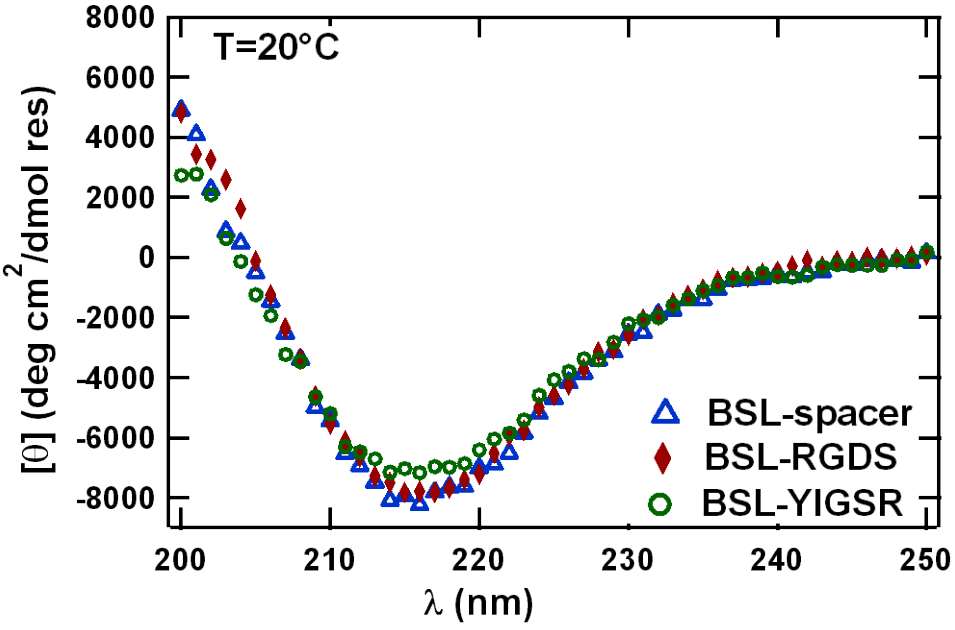

Figure 3-5d CD wavelength scans for 20 μM solutions of BSL proteins in 10 mM phosphate buffer, 1 M NaCl, pH 7.5 at 20 °C.

Since CD spectroscopy is most suitable for qualitative determination of the secondary structure of proteins, we can only roughly estimate β-sheet contents of the diblock proteins from these data. The approximate β-sheet content, determined by the software SOMCD software package [145], for all diblock constructs was between 40%-50% of the content of a homogeneous β-sheet protein. These estimates were somewhat lower than expected values. The fraction of β-sheet content for BSS-spacer was estimated at 45%, a 13% deviation from the theoretical calculation of 58% based on sequence. Likewise, the β-sheet contents were 46% for BSS-RGDS (a 9% deviation compared with theoretical value of 55%) and 48% for BSS-YIGSR (a 4% from the theoretical calculation of 52%). This trend of underestimation of β-sheet content was also observed for the BSL constructs. The estimated fraction of β-sheet contents using SOMCD for BSL-spacer, BSL-RGDS and BSL-YIGSR were 44%, 41% and 39%, respectively, corresponding to deviations from the expected design values of 6%, 7%, and 7%, respectively. The differences between β-sheet contents from theoretical calculations based on protein design and estimation by SOMCD based on CD wave scans are most likely due to the difficulty in de-convolution of CD spectra into contributions from different secondary structures (a difficult inverse problem). For this reason, FTIR was used to determine quantitative secondary structure of these proteins, as will be described later in this chapter.

Solution pH and temperature affect the secondary structure of these diblock proteins. Figure 3-6 shows the wavelength scans of BSS-YIGSR in two buffers: dH2O at pH 11 and 10 mM phosphate buffer with 1 M NaCl at pH 7.5. For wavelength scans of these solutions at 20 ˚C, the figure shows that the pH 11 sample exists in a denatured state of the protein

when compared to the native state of the protein in the phosphate buffer at pH 7.5. Moreover, subsequent wavelength scans of the protein in phosphate buffer after heating to 80 ˚C and again after cooling to 20 ˚C clearly show thermal denaturation of protein secondary structure upon heating followed by recovery of secondary structure upon cooling. Importantly, the wavelength scans at the initial and final 20 ˚C temperatures coincide, indicating full reversibility of these proteins after a denaturation process. The thermal reversibility of the native and denatured states is important for protein utility. The protein denatured in high pH solutions is also useful for protein preparation and protein application, and is also reversible by lowering pH.

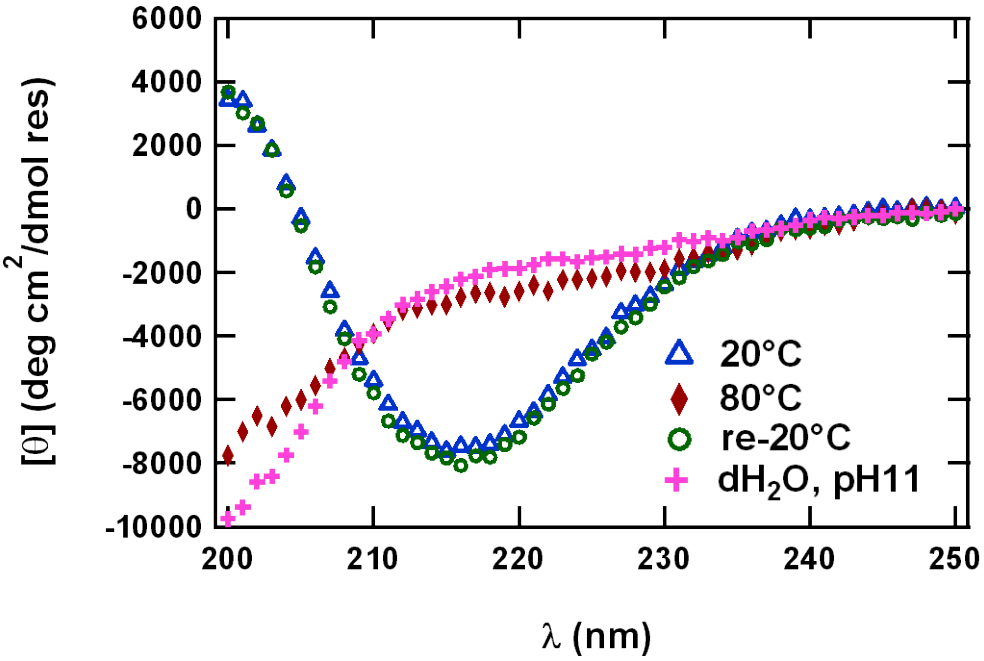

Figure 3-6 CD wave scans of BSS-YIGSR in buffer dH_2O, pH 11, and BSS-YIGSR in 10 mM phosphate buffer, 1 M NaCl, pH 7.5 at 20 ˚C→80 ˚C→re-20 ˚C.

To further explore the thermal behavior of these proteins, CD thermal scans were performed for 20 μM diblock protein solutions in 10 mM phosphate buffer at pH 7.5 with or

without 1 M NaCl by monitoring the CD signals at 217 nm, the characteristic minimum position indicative of β-sheet secondary structure in wavelength scans. Thermally-induced denaturation is exhibited by plots of mean residue molar ellipticity [θ] at λ = 217 nm for each protein as a function of temperature in Figure 3-7. These results demonstrate the essentially identical temperature dependence of secondary structure of all the diblock proteins in the same buffer. These data indicate that the insertion of different bioactive domains does not significantly affect secondary structure in these diblock proteins. Values of [θ] obtained from these melting curves were used to calculate the relative fraction (f) of folded β-sheet structure. Plots of fractions as a function of temperature for each protein are shown in Figure 3-8. Overall, well folded β-sheets at room temperature become progressively more disordered with increasing temperature and then fully recovered their β-sheet structure when the temperature decreased back to room temperature. The melting temperature for the secondary structure was defined as the temperature at which f = 0.5. Analysis of the folded fraction data indicated melting temperatures of 43±1° for BSS and 45±1°C for BSL proteins in 10 mM phosphate buffer at pH 7.5 without salt, and 67±1° for BSS and BSL proteins in 10 mM phosphate buffer at pH 7.5 with 1M NaCl. These results show that added NaCl is capable of substantially increasing the stability of β-sheet structure relative to the protein solutions without added salt, a conclusion that is consistent with the previous results for wavelength scans at fixed temperature.

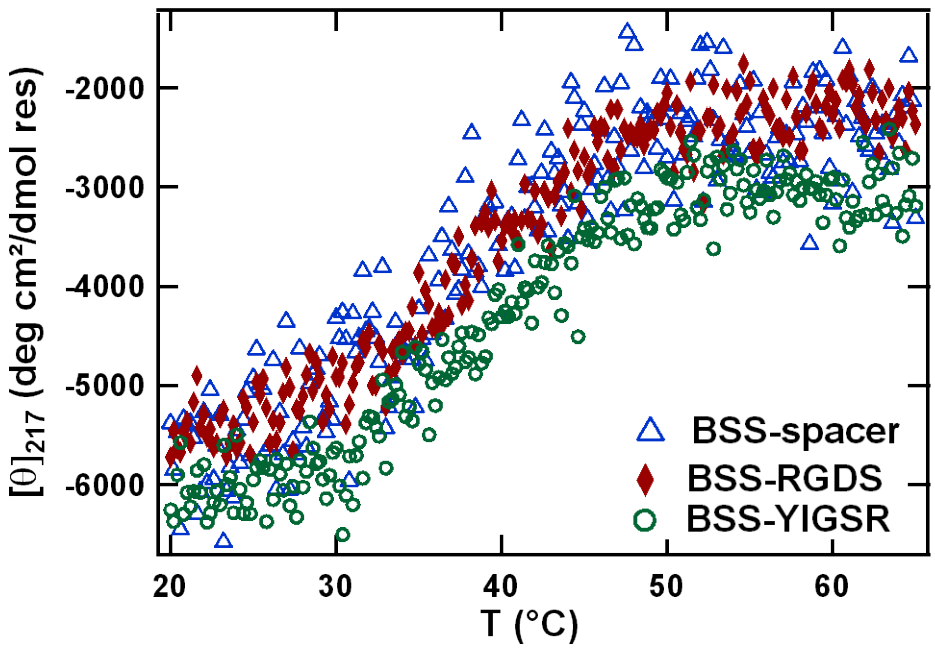

Figure 3-7a CD thermal scans for 20 μM solutions of BSS proteins in 10 mM phosphate buffer,pH 7.5.

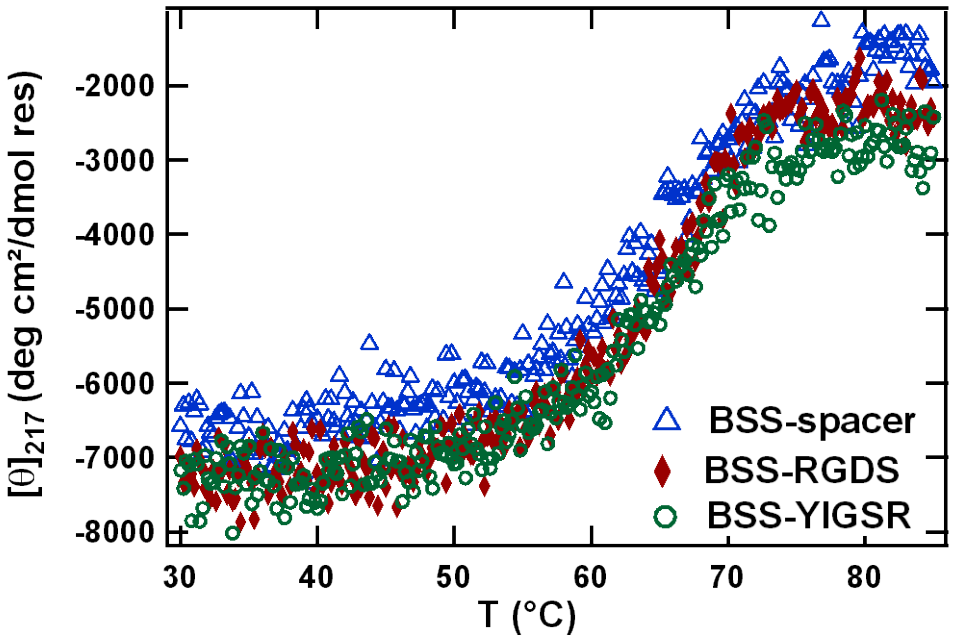

Figure 3-7b CD thermal scans for 20 μM solutions of BSS proteins in 10 mM phosphate buffer, 1 M NaCl, pH7.5.

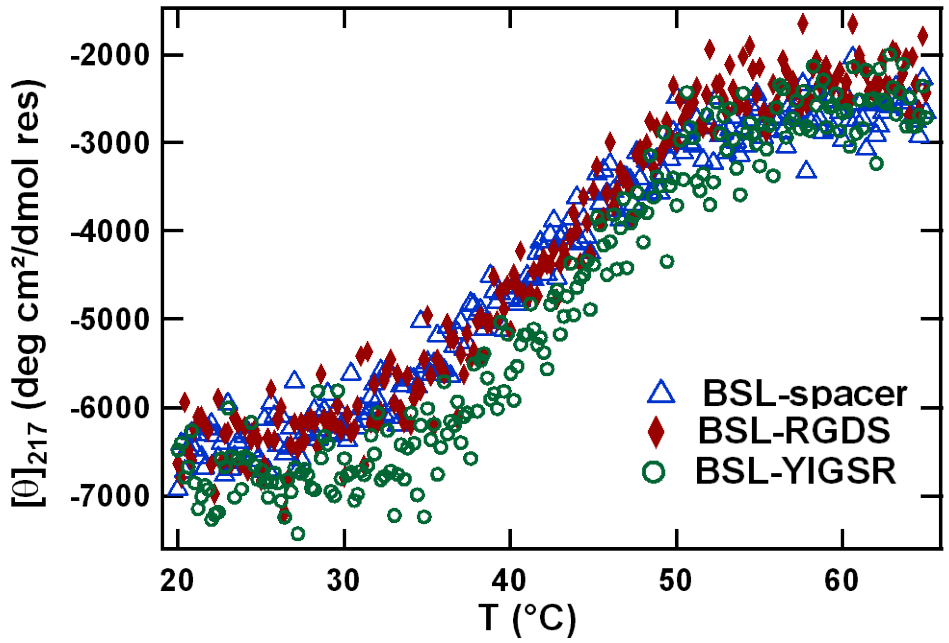

Figure 3-7c CD thermal scans for 20 μM solutions of BSL proteins in 10 mM phosphate buffer, pH 7.5.

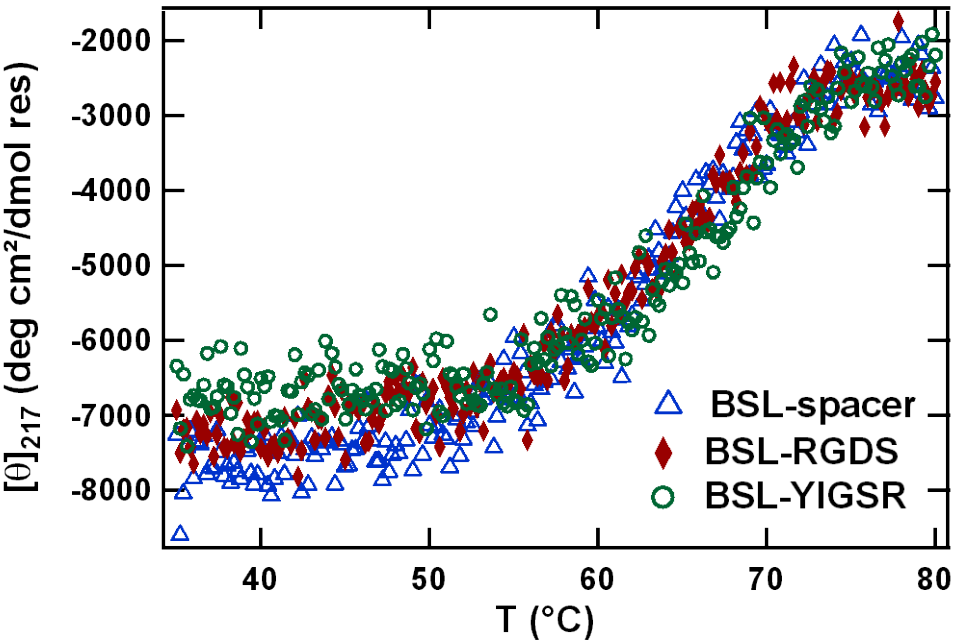

Figure 3-7d CD thermal scans for 20 μM solutions of BSL proteins in 10 mM phosphate buffer, 1 M NaCl, pH 7.5.

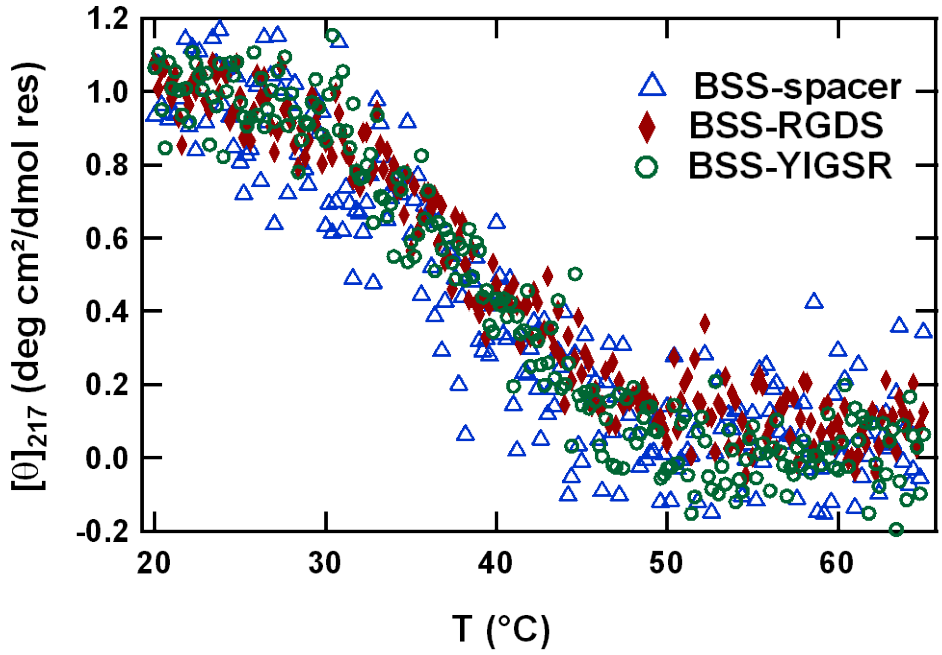

Figure 3-8a Fractions of folded β-sheet contents for 20 μM solutions of BSS proteins in 10 mM phosphate buffer, pH 7.5.

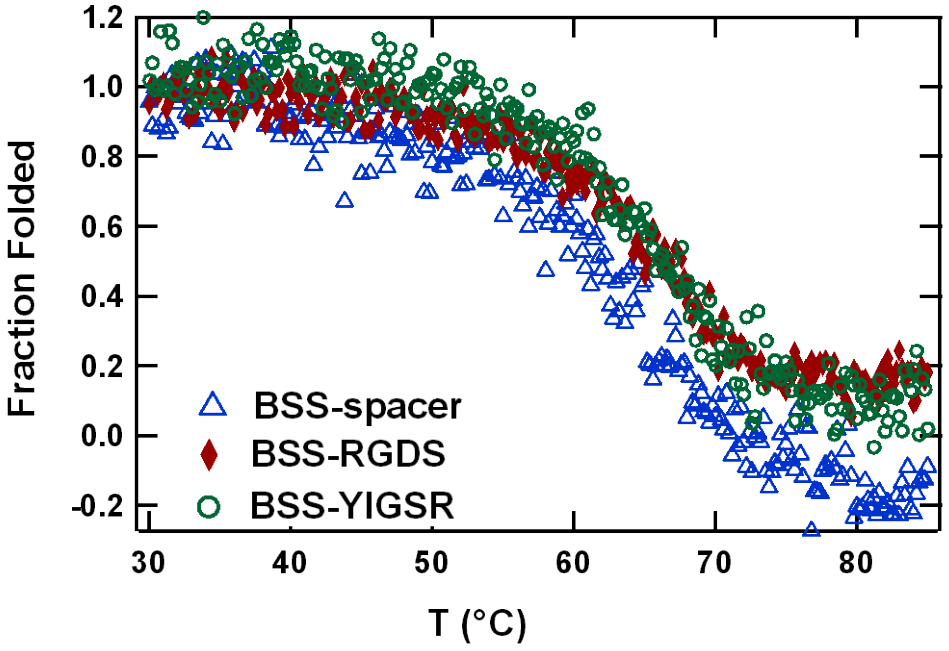

Figure 3-8b Fractions of folded β-sheet contents for 20 μM solutions of BSS proteins in 10 mM phosphate buffer, 1 M NaCl, pH 7.5.

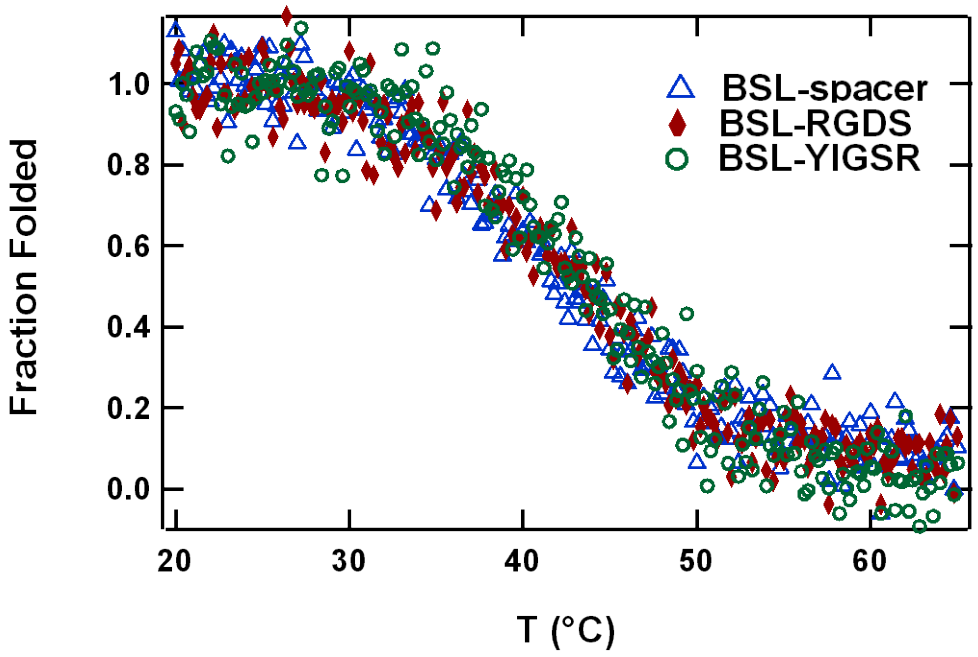

Figure 3-8c Fractions of folded β-sheet contents for 20 μM solutions of BSL proteins in 10 mM phosphate buffer, pH 7.5.

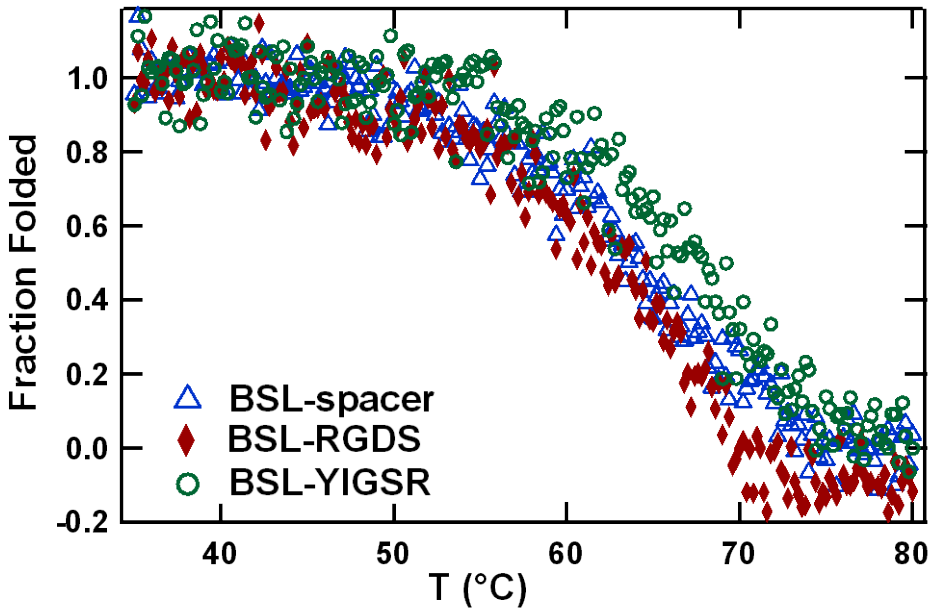

Figure 3-8d Fractions of folded β-sheet contents for 20 μM solutions of BSL proteins in 10 mM phosphate buffer, 1 M NaCl, pH 7.5.

Based on CD spectroscopy studies, all designed diblock proteins demonstrated similar secondary structures and almost identical thermodynamic properties. They all had distinct β-sheet structures with a pronounced minimum signal at λ= 217 nm. All diblock proteins undergo order-disorder transitions in secondary structure when temperature increased and presented very similar secondary structure melting temperatures in equivalent buffers. Since later studies were focused on BSL-spacer and BSL-RGDS, more detailed studies of their secondary structure with FTIR and their thermal behavior with DSC are discussed next.

3.3.3 FTIR Analysis of Structures of Diblock Proteins

Since the intended application of these proteins is for adsorbed biofunctional coatings on surfaces, it is of interest to characterize the secondary structure of the proteins in a monolayer configuration. Monolayers formed by BSL-spacer or BSL-RGDS were evaluated with ATR-FTIR spectroscopy. Based on the analysis of the amide I band (~1600-1690 cm^{-1}), which is associated with the C=O stretching vibration and backbone conformation, the secondary structures of these proteins in monolayers were then determined. Figure 3-9 shows the IR spectra of monolayers of BSL-spacer and BSL-RGDS in deuterated 10 mM phosphate buffer at pH 7.5. The spectra exhibited similar shapes for both BSL-spacer and BSL-RGDS, which indicated that both proteins possess similar secondary structure. Significant peaks at around 1626 cm^{-1} corresponded to high contents of β-sheet conformers.

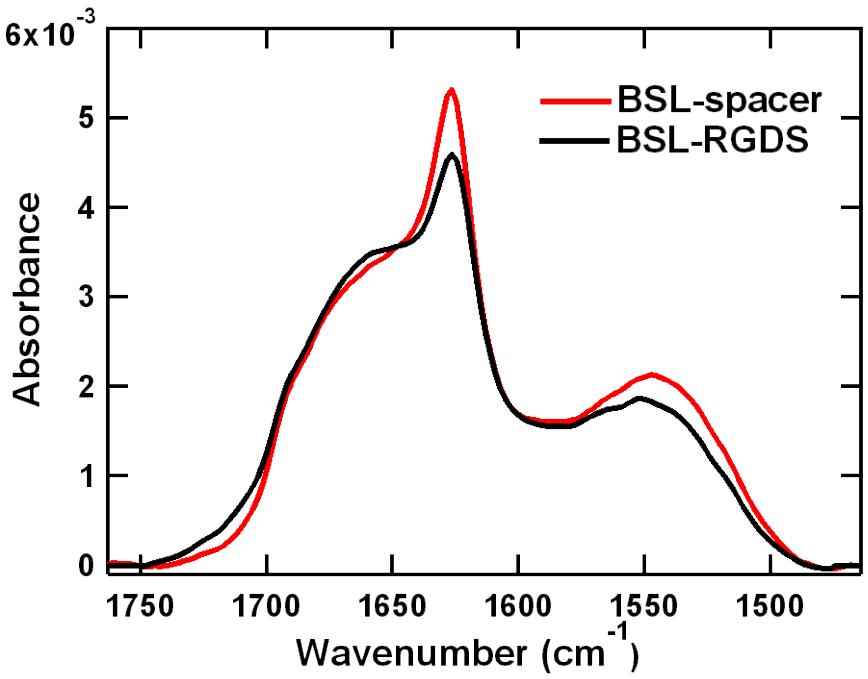

Figure 3- 9 IR spectra of BSL-spacer and BSL-RGDS in 10 mM phosphate buffer, pH 7.5.

To obtain clearly resolved peaks, Fourier self-deconvolution and second derivative analysis of IR spectra were performed, as shown in Figure 3-10. These peaks were associated with secondary structures such as β-sheets, turns and random coils, thereby characterizing the secondary structures of these two diblock proteins. Both Fourier self-deconvolution and the second derivative of IR spectra made the underlying features of the spectra more evident than in the original, unprocessed IR spectra in the range of the amide I band. The signals of Fourier self-deconvolution of IR spectra for both BSL-spacer and BSL-RGDS exhibited a broad but distinct peak at approximately 1660 cm^{-1} in addition to the peak at 1626 cm^{-1} that was also seen in the unprocessed IR spectra. The second derivative of IR spectra also uncovered a peak near 1692 cm^{-1} for both BSL-spacer and BSL-RGDS. BSL-spacer and BSL-RGDS demonstrated very similar IR spectra in amide I band range. The BSL-spacer data is first discussed. An intense absorption at approximately 1626 cm^{-1} for

BSL-spacer corresponds to its high content of β-sheet conformers. Another peak near 1660 cm^{-1} identified from Fourier self-deconvolution was assigned to random coil conformers. It is possible that this broad peak is actually a combination of poorly resolved multiple peaks between 1650 cm^{-1} and 1670 cm^{-1}, as was also found using second derivative analysis. However, it was hard to accurately distinguish these peaks from the background noise. Another peak near 1692 cm^{-1} suggested by second derivative analysis is characteristic of aggregated anti-parallel β-sheet strands. For BSL-RGDS, the signal near 1626 cm^{-1} is also attributed to a high content of β-sheet structure. The peak near 1659 cm^{-1} identified from Fourier self-deconvolution is an indication of random coil conformers (or, as before, a combination of multiple peaks between 1650 cm^{-1} and 1670 cm^{-1} due to the broad peak). The peak near 1692 cm^{-1} suggested by second derivative analysis is an indication of antiparallel β-sheet strands.

Fourier self-deconvolution and second derivative analysis of IR spectra were of great utility for locating minor peaks, as discussed above. For example, the peak near 1691 cm^{-1} that was assigned to antiparallel β-sheet strands, was only present in second derivative IR spectra for both BSL-spacer and BSL-RGDS. Moreover, the Fourier self-deconvolution analysis uncovered a distinct peak near 1660 cm^{-1} which was not evident in the original, unprocessed data. Based on analysis of Fourier self-deconvolution and second derivative of IR spectra, it can be inferred that both BSL-spacer and BSL-RGDS secondary structures are a combination of β-sheets and random coils, and had a very high portion of β-sheets, irrespective of the presence of the RGDS residues at the terminus of the disordered block.

However, the slightly higher peaks at around 1626 cm^{-1} for the BSL-spacer system indicated relative higher fraction of β-sheet content relative to the BSL-RGDS system.

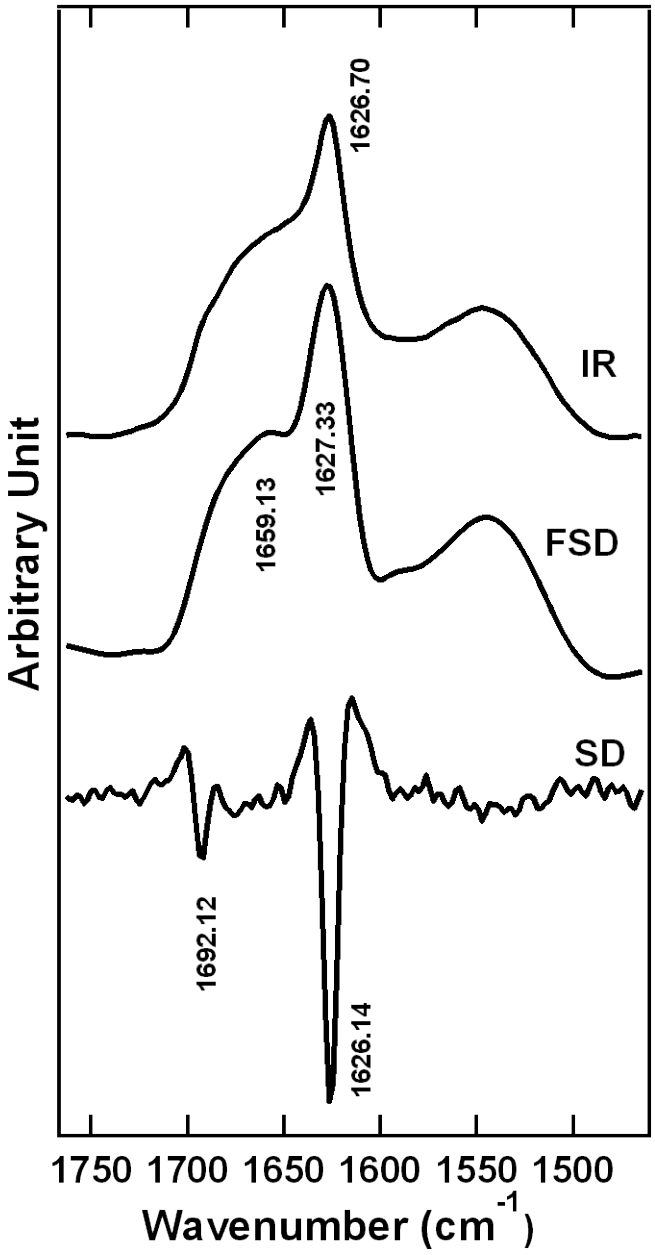

Figure 3-10a IR spectra, Fourier self-deconvolution and second derivative of BSL-Spacer

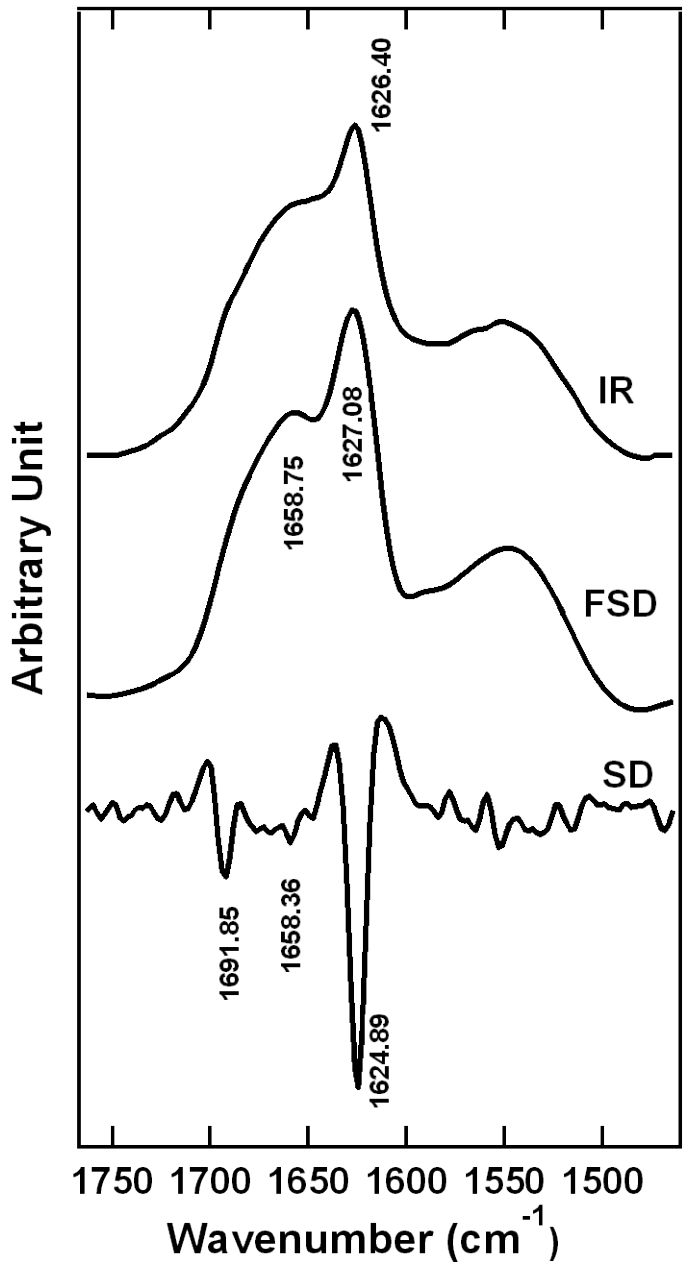

Figure 3-10b IR spectra, Fourier self-deconvolution and second derivative of BSL-RGDS.

Through peak analysis of FTIR spectroscopy data, it is possible to assign a quantitative estimate of the fraction of different secondary structure contributions. Based on the assumptions that IR spectra of proteins are a linear sum of spectra of fundamental

secondary structural elements, and the percentage of each element is only related to the spectral intensity, IR spectra of proteins can be deconvolved into several elements. IR spectra of BSL-spacer and BSL-RGDS were deconvolved and fitted with Gaussian-Lorentzian functions, as shown in Figure 3-11. The fitting parameters are shown in Table 3-2. The areas of deconvolved peaks correspond to fractions of different types of secondary structural components. Based on curve fitting results, the secondary structure of the BSL-spacer protein consists of 51% of β-sheets, 25% of β-turns and 24% of random coil. This is in excellent agreement with the theoretical values from the design sequence (50% of β-sheets, 24% of β-turns and 26% of random coil), indicating a 1% of deviation for β-sheets and β-turns, and a 2% deviation for random coils. Curve fitting data for BSL-RGDS suggests a secondary structure composed of 49% of β-sheets, 23% of β-turns and 28% of random coil. Compared with theoretical values from the design sequence (47% of β-sheets, 23% of β-turns and 30% of random coil), a 2% of deviation for β-sheets and random coils was found. In order to evaluate the reliability of the IR deconvolution results for these two diblock proteins, other curve fittings with different combination of peak location, area, FWHM and height were performed (The data are not shown in the thesis). All curve fittings of IR spectra yielded precise secondary structures that closely agreed with design values (less than 5% deviation).

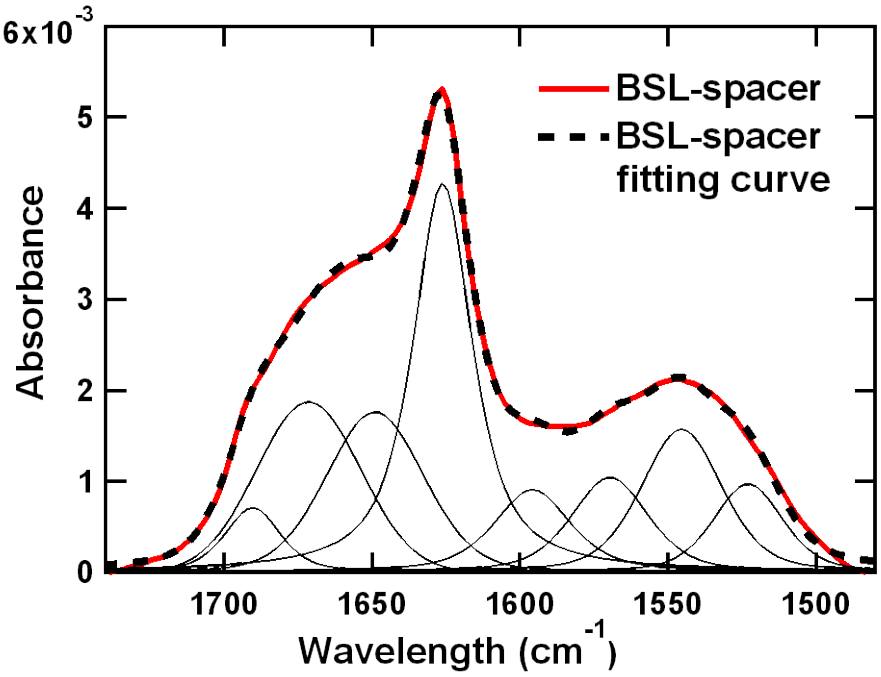

Figure 3-11a Curve fitting of IR spectra of BLS-spacer (dash line).

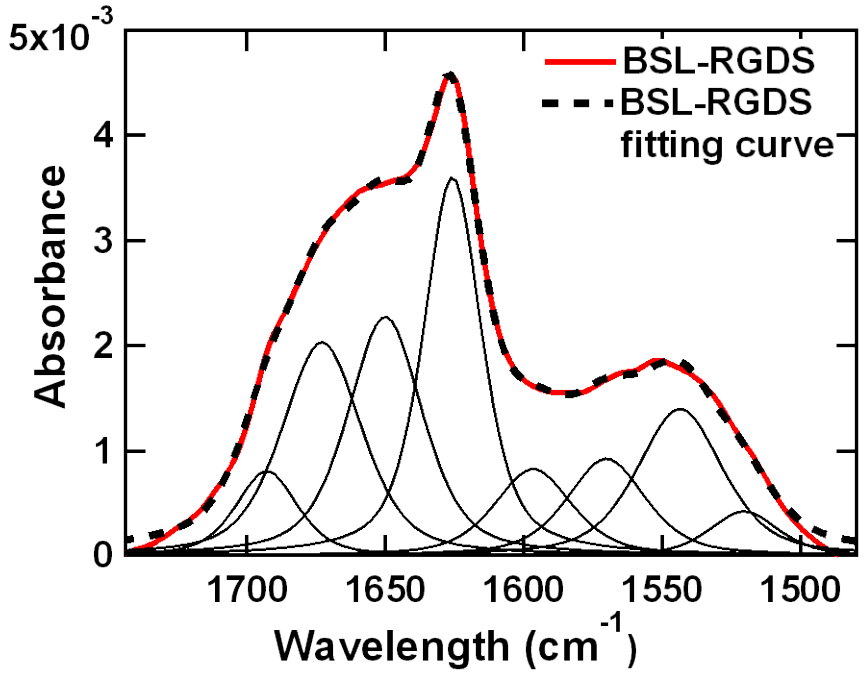

Figure 3-11b Curve fitting of IR spectra of BLS-RGDS (dash line).

Table 3-2a Fitting parameters for IR spectra of BSL-spacer

Peak#	Peak type	Location(center)	height	FWHM	area
1	Gaussian-Lorentzian	1522.87	0.00097	27.73	0.034
2	Gaussian-Lorentzian	1545.36	0.00157	32.25	0.063
3	Gaussian-Lorentzian	1569.57	0.00104	30.74	0.042
4	Gaussian-Lorentzian	1595.82	0.00091	30.75	0.038
5	Gaussian-Lorentzian	1626.14	0.00428	23.98	0.149
6	Gaussian-Lorentzian	1649.51	0.00176	38.84	0.079
7	Gaussian-Lorentzian	1671.45	0.00187	41.40	0.082
8	Gaussian-Lorentzian	1690.39	0.00071	22.13	0.021

Table 3-2b Fitting parameters for IR spectra of BSL-RGDS

Peak#	Peak type	Location(center)	height	FWHM	area
1	Gaussian-Lorentzian	1520.42	0.00054	29.54	0.019
2	Gaussian-Lorentzian	1543.55	0.00134	36.57	0.052
3	Gaussian-Lorentzian	1570.16	0.00094	33.73	0.037
4	Gaussian-Lorentzian	1596.62	0.00101	33.23	0.051
5	Gaussian-Lorentzian	1625.80	0.00367	24.92	0.122
6	Gaussian-Lorentzian	1650.08	0.00228	32.08	0.093
7	Gaussian-Lorentzian	1672.98	0.00195	34.19	0.077
8	Gaussian-Lorentzian	1692.92	0.00094	26.41	0.038

3.3.4 DSC Studies of Thermodynamic Properties

Quantitative thermodynamic properties of a protein in solution can be acquired by measuring its molar heat capacity at constant pressure ($C_{p)}$ as a function of temperature (T) using DSC. In this chapter, DSC studies were carried out for BSL-spacer and BSL-RGDS in 10 mM phosphate buffer at pH 7.5 with a scan rate at 1 °C/min as temperature increased from 10 to 90 °C. Three scans were collected and averaged for each protein.

Figure 3-12a shows an example of raw data obtained for the BSL-spacer protein in a DSC experiment with the heat flow rate as a function of the temperature. The heat flow can be converted to the molar heat capacity at a constant pressure by the equation $C_p = (\frac{\partial H}{\partial T})_p$.

The corresponding curve, illustrated in Figure 3-12b, shows the molar heat capacity of the protein as a function of the temperature. The change of molar heat capacity ΔC_p can be split into two terms, described as $\Delta C_p = \Delta C_{p,\,tran.} + \Delta C_{p,base.}$ [141]. $\Delta C_{p,\,tran}$ is the change of the molar heat capacity related to the transition peak, and $\Delta C_{p,base}$ is the change of the molar heat capacity related to the shift of the baseline from $C_{p,n}$ (molar heat capacity at the native state) to $C_{p,d}$ (molar heat capacity at the denatured state) due to the transition. Curves of the change of molar heat capacity as a function of temperature were generated by correction with the Linear-polynomial (sigmoidal) baseline, as illustrated in Figure 3-13. Both BSL-spacer and BSL-RGDS demonstrated similar curves of ΔC_p versus temperature, which indicated a similar ordered-disordered transition process for both.

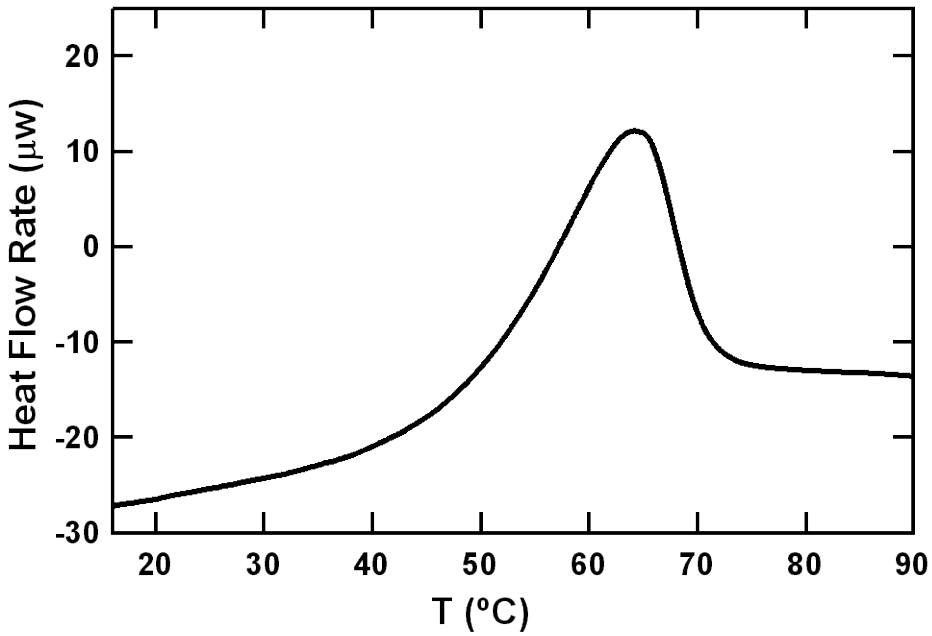

Figure 3-12a A curve of heat flow rate versus temperature for 0.45 mM solutions of BSL-spacer in 10 mM phosphate buffer, pH 7.5.

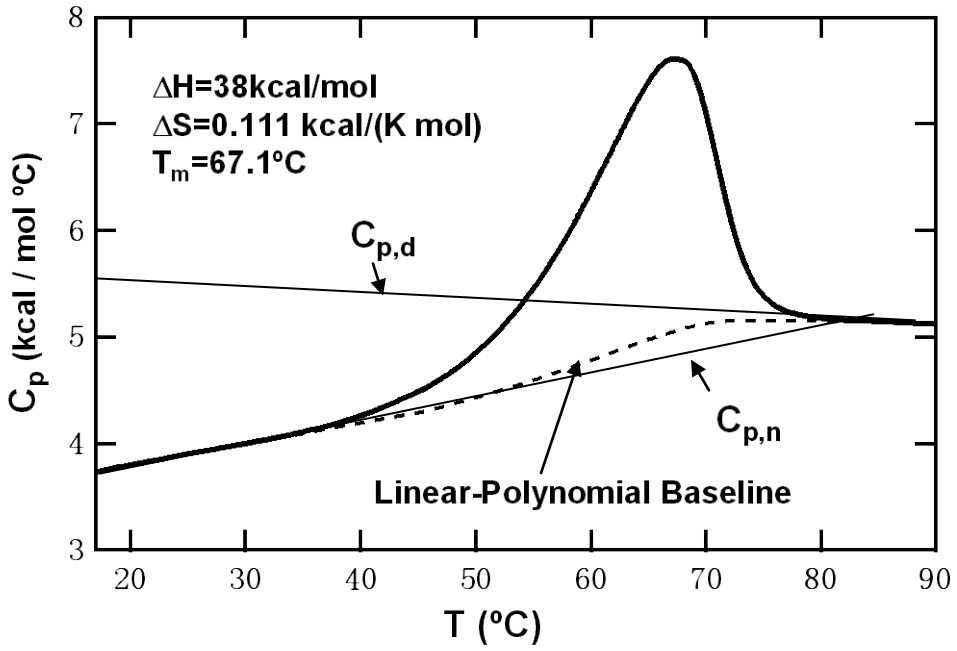

Figure 3-12b A curve of the molar heat capacity versus temperature for 0.45 mM solutions of BSL-spacer in 10 mM phosphate buffer, pH 7.5. $C_{p,n}$ refers to molar heat capacity at native state; $C_{p,d}$ refers to molar heat capacity at denatured state.

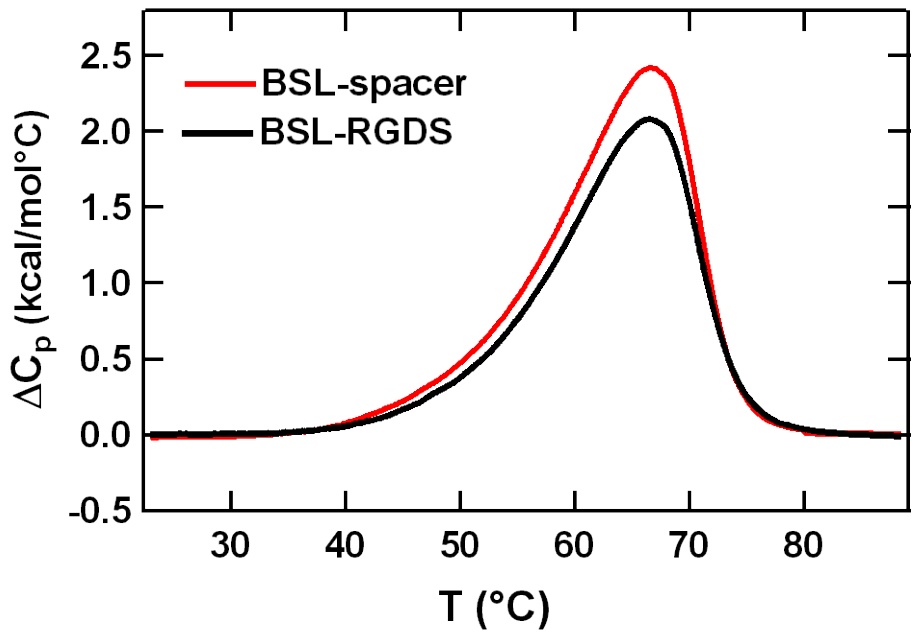

Figure 3- 13 Curves of the change of molar heat capacity versus temperature for 0.45 mM solutions of BSL proteins in 10 mM phosphate buffer, pH 7.5.

Quantitative thermodynamic properties were also presented with the corresponding change in enthalpy ΔH(T) and change in entropy ΔS(T). ΔH(T) of a system is related to the amount of the heat absorbed or released in a reaction carried out at constant pressure [146]. The entropy change of a system (ΔS) was originally defined for a thermodynamically reversible process as the heat transferred into the system divided by temperature (T) at which the process occurs. It is described as equation: $\Delta S = \int \frac{dQ}{T}$ [146]. In statistical thermodynamics, Boltzmann quantitatively defined the entropy and related it to the number of possible microscopic configurations available to the system by the equation $S = k_B \ln P$, where P is the number of configurations. The statistical definition extends the concept of entropy as a measure of "disorder" or “randomness” of a system [141, 146]. In DSC

experiments, the changes in enthalpy and in entropy are obtained by integrating ΔC_p in the temperature range.

$$\Delta H(T) = \Delta H(T_m) + \int_{T_m}^{T} \Delta C_p(T) dT$$

$$\Delta S(T) = \Delta S(T_m) + \int_{T_m}^{T} \frac{\Delta C_p(T)}{T} dT$$

In the DSC studies, the BSL-spacer and BSL-RGDS were analyzed with Cpcalc software package, and the changes of enthalpy and the changes of entropy (provided in the inset to Figure 3-14) were determined. Both diblock proteins had almost identical melting temperature of approximately 67 °C. The changes of enthalpy were ΔH=38±1 kcal/mol for BSL-spacer and ΔH=32.3±0.2 kcal/mol for BSL-RGDS, respectively. The relatively higher change in enthalpy inferred for BSL-spacer is presumably the cause of the larger external heat absorbed during the phase transition to break β-sheet content in BSL-spacer compared with the BSL-RGDS. It is consistent with the theoretical protein design for which a higher fraction of β-sheet content is expected in the BSL-spacer. The changes of entropy were ΔS=0.112±0.004 kcal/(K·mol) for the BSL-spacer and ΔS=0.0949±0.0006 kcal/(K·mol) for the BSL-RGDS, respectively. As we have already discussed, the entropy is related to the number of the possible microscopic configurations (microstates) available to the system. The increase in the entropy for both the BSL-spacer and BSL-RGDS indicated the increase of the possible configurations during the transitions. In another word, proteins undergo an order-disorder transition from folded β-sheets with specific configurations to denatured random coils with many configurations.

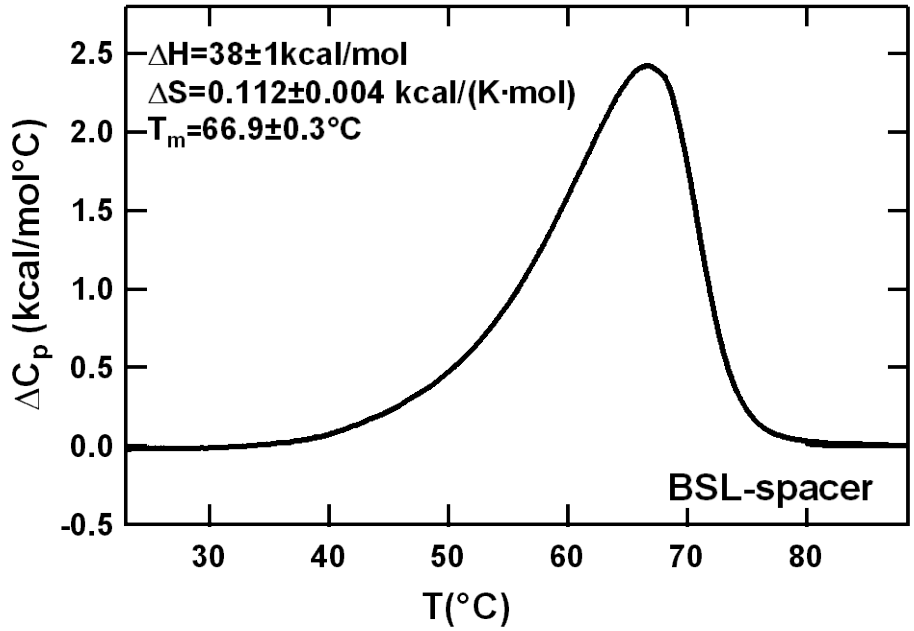

Figure 3-14a The change of molar heat capacity versus temperature for 0.45mM BSL-spacer solution in 10 mM phosphate buffer, pH7.5 with thermodynamic properties presented.

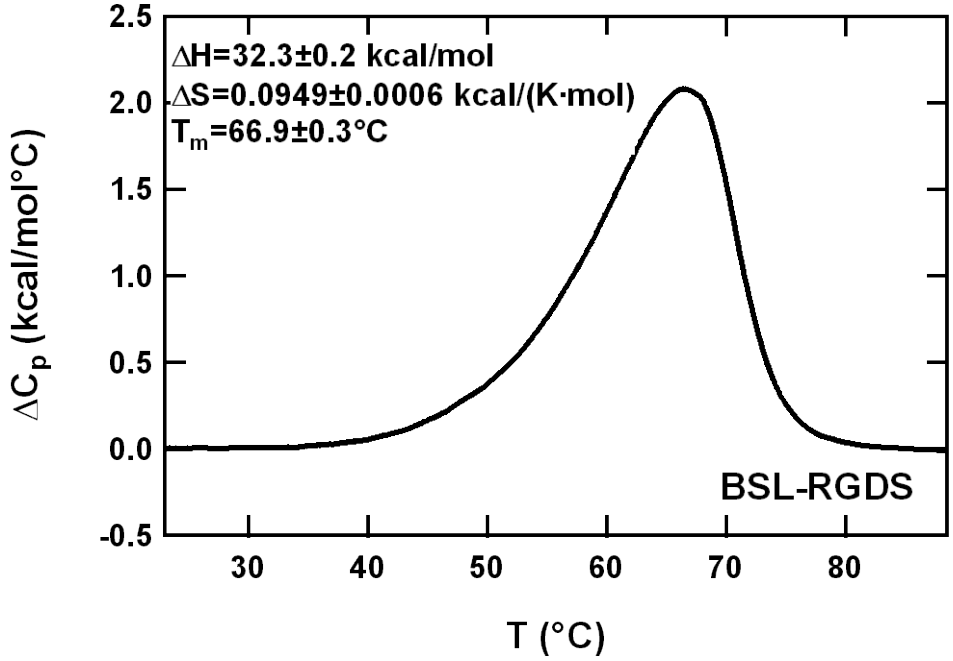

Figure 3-14b The change of molar heat capacity versus temperature for 0.45 mM BSL-RGDS solution in 10 mM phosphate buffer, pH 7.5 with thermodynamic properties presented.

The concentration dependence of the melting temperature was also studied by performing DSC measurements of BSL-spacer solutions at various concentrations. As before, the melting temperatures were determined by Cpcalc software. Figure 3-15 shows that the melting temperature increases with increasing concentration of proteins. The inferred melting temperature data was fit to a LogNormal function using the Igor Pro software package (Wave metrics, Inc., Oregon, USA). It is evident from the fit to the data (Linear curve in Figure 3-15) that the melting temperature of the BSL-spacer proteins increased logarithmically with the increase of concentration of proteins. The melting temperature was approximately 47 °C for 20 µM protein solutions which was consistent with the result from CD studies. The close correspondence at 47 °C between the loss of secondary structure from CD and the transition in the DSC is an indication that DSC is primarily monitoring the thermal behavior of secondary structure near the order-disorder transition in this system.

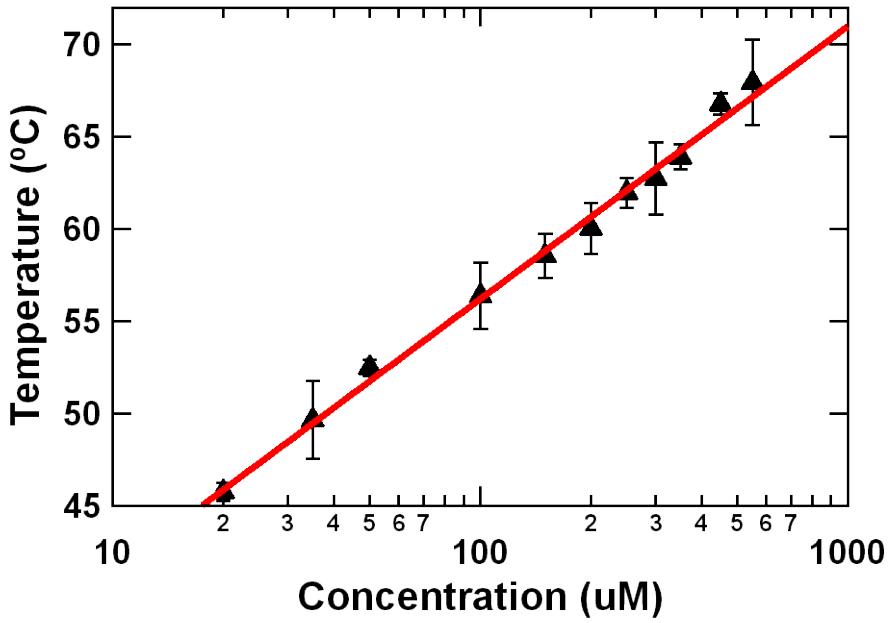

Figure 3-15 Concentration-dependent melting temperature of BSL-spacer in 10 mM phosphate buffer, pH 7.5.

3.4 Conclusions

Basic characterization of the molecular properties of the β-sheet-based proteins was presented in this chapter. The primary structures of proteins were confirmed using both MALDI-TOF mass spectroscopy and amino acid composition analysis. Techniques of CD, FTIR and DSC were used to study the secondary structure of the proteins. It is demonstrated that the proteins are composed of β-sheet, β-turn, and disordered coil secondary structures in ambient and physiological temperature conditions. The fraction of β-sheet content was shown by FTIR studies to be close to the designed β-sheet content. Thus, the disordered coil domains attached to the β-sheet structures were demonstrated to not dramatically affect secondary structure of the β-sheet domains. In particular, this suggests that the insertion of bioactive domains, such as RGDS, YIGSR, at the terminus of the disordered coil module did not affect secondary structures of proteins. This suggests that the inclusion of other domains, including the silver-binding domain and hydroxyapaptite-binding domain discussed in later chapters, would also not adversely affect the function of the associating β-sheet domain.

CD thermal scans and DSC studies also demonstrated that diblock proteins undergo reversible order-disorder transitions associated with loss of β-sheet secondary structure as temperature increased. Importantly, it was found that β-sheet structure was fully restored after denaturation by temperature decrease below the melting point. Such a reversible order-disorder transition is useful for manipulation of proteins during the experiments and for future applications of these materials. Moreover, the presence of NaCl in diblock protein solutions caused the reinforcement of minimal mean residue molar ellipticity in CD

wavelength scans and the increase of melting temperature in CD thermal scans. Both phenomena indicate that added NaCl is capable of increasing the stability of β-sheet structure relative to the salt-free diblock protein solutions.

Chapter 4

Biofunctional Surface Coatings with Diblock Proteins

4.1 Introduction

The interactions between material surfaces and cells play an important biological role in cellular behavior. These interactions influence or determine many aspects of cell physiology such as cell adhesion, spreading, migration, proliferation, and differentiation [147,148]. Investigation of cell-surface interactions is paramount to biomedicine and bioengineering including tissue engineering, biomaterials design and developmental biology. The cell-surface interactions strongly depend on the biophysical and biochemical properties of surfaces including roughness, surface energy, hydrophilicity, topography and presence of functional groups [149-153].

Several techniques to carefully control biofunctional properties of substrate surfaces have been developed. One strategy to regulate cell–substrate interactions is to physically change the morphology of the materials by introducing patterned surfaces [154]. Another approach is to modify surfaces using chemical treatments. There are numerous examples of this approach in the literature. Reactive groups for bioconjugation of ligands can be introduced to polymeric materials via plasma treatment or wet chemical methods [155,156].

Carboxylated polyurethanes can be produced using a bimolecular nucleophilic substitution [98]. Silane treatments are able to modify hydroxylated surfaces such as silicon and glass with stable monolayers of amines, thiols, epoxides or carboxylic acids that may in turn be used to attach biofunctional agents such as peptides and proteins [157-159]. Photochemical methods have also been used for functionalizing polytetrafluoroethylene with reactive groups [160,161]. Chemical functional moieties like amines, carboxyl, hydroxyl or other groups can also be grafted to the relatively hydrophobic polymer surfaces using ionizing radiation, UV radiation or ozone [162-164].

An alternative strategy to regulate cell-surface interactions is achieved by self assembly methods based on physical association of surface-active molecules with surfaces. Although such physically associated molecules are not irreversibly bound to a surface, the resulting surface layers can be stable for the typical lifetime of an experiment or application. Self-assembled monolayers (SAMs) are used to create controlled interfaces with the high ligand density and efficient ligand presentation [165,166]. Structurally well-ordered SAMs of alkanethiolates are spontaneously formed once a gold-coated substrate is immersed into a solution of alkanethiols [166]. By introducing a variety of ligands with the defined densities and patterns onto an otherwise non-interacting substrate, Mrksich [166] demonstrated a good control of SAMs on interfacial molecular structures and the ligand-receptor interactions between material surfaces and cells. Another uses protein surface activity as a means of immobilizing artificial proteins with conjugated cell-interactive biomolecules (such as growth factors) or embedded cell recognition peptide motifs (such as the Arg-Gly-Asp (RGD) peptide) onto the substrate surfaces to control cell behavior via ligand-receptor

interactions [30]. These artificial proteins can be designed to ensure that their biologically active ligands are fully functional and do not interfere with their surface-active assembly domains, thus ensuring a well-defined bioactive surface [30]. The bioactive ligands can be chosen to act as adhesion peptides, antibiotics, inhibitors, cell-membrane receptor fragments, enzymes, plasminogen activators, and may be designed to mimic particular native biomolecules such as adhesive carbohydrates, glycosaminoglycans, and extracellular matrix (ECM) components. The adhesion peptide sequence Arg-Gly-Asp (RGD), a ubiquitous cell-binding domain originated from cell adhesion ECM proteins like fibronectin and vitronectin, is by far the most studied bioactive domain in cell-interactive surfaces. The RGD sequence is recognized by the integrin family of cell surface adhesion receptors, and forms the well studied ligand–receptor pair that stimulates the formation of focal adhesion complexes [75, 147, 167-169]. Early work demonstrating the efficacy of the RGD sequence for cell binding and focal adhesion formation used glass surfaces to immobilize the ligands [30]. Subsequently, RGD-based peptides have been covalently coupled to numerous natural and synthetic materials, including silk [93, 94], collagen [170-173], alginates [96], titanium implants [99], synthetic polymer hydrogels [100, 174-176], PDMS surfaces [91], and surface-active protein polymers [30, 177-178]. RGD peptide variants that have been studied include RGD[90,94-96], RGDS[30,90,94,96], RGDV[90], RGDT[90], GRGDS[94], GRGDY[95], GRGDVY[98], GRGESY[98], GRGDSP[96], GRGDNP[96].

This chapter reports on the studies of the surface activity and cell interactions of designed amphiphilic diblock proteins incorporating an integrin-binding ligand RGDS. Self-assembly of stable surface layers of these diblock proteins onto both smooth and porous

synthetic polymer materials, polystyrene (PS) and polyethylene terephthalate (PET), was first studied. Subsequently, cell adhesion and response to these coated surfaces was characterized using optical microscopy and cell proliferation assays. It was found that (i) surface adsorption of the proteins had minimal impact on the presentation of the bioactive domains in the soluble block, and (ii) the biofunctional interfaces were capable of inducing appropriate cellular responses in a variety of human cell types. In particular, we were able to mediate cell behavior such as attachment and spreading by controlling the ratio of bioactive protein (with RGDS) and bioneutral protein (without RGDS), thus providing a tunable cell adhesion system.

4.2 Materials and Methods

4.2.1 Materials and Reagents

Untreated, porous polyethylene terephthalate (PET) meshes were purchased from New Brunswick Scientific (Edison, NJ, USA). Untreated polystyrene petri dishes were purchased from Corning Inc. (NY, USA). Gold-coated SPR sensor chips were purchased from SensiQ Technologies Inc. (Oklahoma, OK, USA). C2C12 mouse myoblast cells were kindly provided by the lab of Prof. Andrew Pelling at the University of Ottawa, and Human Foreskin Fibroblasts (HFF) were purchased from ATCC (Manassas, VA, USA). DMEM medium, fetal bovine serum (FBS) and streptomycin/penicillin (P/S) were purchased from Sigma-Aldrich (Oakville, ON, Canada). The WST-1 Cell Proliferation Assay was purchased from Roche (Laval, QC, Canada). All reagents for fluorescent labeling of cells were

purchased from Life Technologies (Burlington, ON, Canada). All other chemicals were purchased either from Sigma-Aldrich or Fisher Scientific (Ottawa, ON, Canada).

4.2.2 Surface Plasmon Resonance (SPR)

To characterize the surface activity of the proteins, surface plasmon resonance (SPR) studies were carried out. Surface plasmons (SPs) are collective oscillations of the conduction electrons that exist at the interface between two materials with dielectric constants of opposite signs such as metal-dielectric interfaces [179]. The resonance condition is established by matching the frequency of photons which excite surface plasmons with the natural frequency of surface electrons. SPR occurs when polarized light interacts with a supported conducting metal layer, typically gold and silver in conditions of total internal reflection. At a particular angle of incidence (corresponding to total internal reflection), a resonance occurs in which the evanescent wave excites an intense wave of conducting electrons (the so-called plasmon excitation) at the free surface of the metal layer, resulting in a reduction in intensity of the reflected light due to the energy transferred to the plasma [141]. This surface plasmon excitation is sensitive to the presence of material at the free surface of the metal film, providing a means to detect subtle changes in adsorption to this surface. This sensitivity has been exploited for biosensing applications [179]. SPR-based biosensors monitor changes in the light reflected by the interface between metal film and the dielectric glass support to deduce the presence of analytes at the free surface of the film. In one typical mode of operation, one monitors an interaction between a ligand immobilized onto the sensor surface and a second soluble component (analyte) injected in am aqueous solution that flows across the sensor surface. When the analyte binds to the

ligand or dissociates from the ligand, the mass increases or decreases, and results in the change in the refractive index close to the surface. This change in refractive index is detected in real time and is expressed in arbitrary or resonance units (RUs). A Sensorgram is plotted by detecting the changes of resonance signal (RUs) as a function of time (s). It is also straightforward to study physical self-assembly of a material onto a sensor surface that has been pre-coated to have a non-specific affinity for the materials. This study uses the latter SPR modality by preparing sensor surfaces that have a hydrophobic polymer layer and monitoring the surface association of an amphiphilic protein domain to this surface.

In order to determine the adsorption of BSL-spacer and BSL-RGDS to the hydrophobic surface, we created sensor chips with such hydrophobic surfaces by spin coating polystyrene (PS) onto native gold sensor chips as described in the following. Gold (Au) sensor chips were spin-coated for 60 s at 2000 rpm with 0.1% (wt) polystyrene (M_w= 350,000, Density=1.04 g/cm^3) in toluene using a WS-400BZ-6NPP/LITE Spin Coater (Laurell Technologies co., North Wales, PA, USA), and subsequently mounted in a SensiQ SPR system (SensiQ Technologies Inc., Oklahoma, OK, USA). Stock 100 μM solutions of diblock proteins in 10 mM phosphate buffer, pH 7.5 were prepared for adsorption studies. Protein concentrations were verified by UV absorption at 280 nm using a NanoDrop 2000 spectrophotometer (Thermo Scientific, Wilmington, DE, USA) and molar extinction coefficients of proteins that were estimated from their primary sequences. For adsorption studies, 250 μl of samples were injected into the microfluidic loop of the SensiQ and passed across the chip flow cell at a speed of 5 μl/min. Subsequently, the chips were exposed to 5ul/min flows of 10 mM phosphate buffer at pH 7.5 for more than 1 hour to eliminate non-

specific binding signals from the protein-coated Au sensors. During loading and washing stages, the SPR reflectance signal was continuously collected to subsequent analysis of the surface associated protein on the PS-coated sensor chip.

4.2.3 Cell Culture

Human foreskin fibroblasts (HFFs) and C2C12 mouse myoblast cells were maintained in DMEM medium containing 300 mg/L L-glutamine, 10% fetal bovine serum (FBS), 100 U/ml penicillin, and 100 mg/ml streptomycin. All cells were cultured in a humidified incubator at 37 °C and 5% CO_2 and harvested with a solution of 0.05% trypsin EDTA when nearly confluent. For experiments, C2C12s and HFFs were cultured in serum-free medium with 100 U/ml penicillin and 100 mg/ml streptomycin added. The serum-free medium was used to minimize competitive adsorption effects occurring for serum proteins.

4.2.4 Assays for Cell Response

The responses of HFFs and C2C12s on protein-coated surfaces were examined for several combinations of adsorbed proteins. Cells were cultured on polystyrene plates coated with 25 μM of protein solution for the following compositions: 100% BSL-spacer, 97.5% BSL-spacer with 2.5% BSL-RGDS, 90% BSL-spacer with 10% BSL-RGDS, and 100% BSL-RGDS. Prior to coating, stock BSL-spacer and BSL-RGDS solutions were prepared at a concentration of 25 μM in 10mM phosphate buffer at pH 7.5, filtered through 0.22 μm syringe filters, and mixed at the ratios listed above. Triplicate wells were then coated by passive adsorption overnight at 4 °C and rinsed excessively with 10mM phosphate buffer at

pH 7.5 before use in order to remove unbound proteins. Subsequently, 200 μL of the cell suspension with a density of approximately 50,000 cells/ml in serum-free media was seeded into each well. After culturing for 24 h, phase contrast microscopy images were taken with an inverted microscope (Eclipse *Ti*, Nikon, Missisauga, Canada).

In order to quantitatively evaluate the responses of HFFs and C2C12s on the protein-coated surfaces, cells were also cultured in 24-well untreated polystyrene (PS) plates coated with BSL-spacer, BSL-RGDS, or combinations of them. As before, 25μM solutions with different ratios of BSL-spacer and BSL-RGDS in 10mM phosphate buffer (pH 7.5) were prepared, filtered through 0.22 μm filters, and coated in triplicate wells by passive adsorption overnight at 4°C and rinsed with PBS to remove unbound protein before testing. Relative metabolic activities of HFFs and C2C12s were then assessed using the WST-1 Cell Proliferation Assay, which directly measures the number of the metabolically active cells in the culture by the cleavage of tetrazolium salts to formazan. Since the formazan exhibits absorbance maxima at 440 nm, quantification of the formazan dye produced by metabolically active cells can be carried out using an ELSA reader (Scanning multi-well spectrophotometer) with the absorbance at 440 nm. 20 μL of WST-1 reagent was added into each well and incubated for 3 h. The absorbance at 440 nm was then monitored with a SpectraMax 190 microplate reader (Molecular Devices, Sunnyvale, CA, USA).

4.2.5 Fluorescence Microscopy

Fluorescent staining of cytoskeletal components (F-actin and vinculin) was performed on HFFs and C2C12s cultured on PS plates coated with protein solutions. As

before, triplicate sterile untreated PS plates were coated with filtered 25 μM protein solutions in 10mM phosphate buffer at pH 7.5 by passive adsorption overnight at 4 ˚C. After rinsing off unbound proteins, 1 ml cell suspensions (approximately 20,000 cells/well) were seeded onto the plates and cultured for a period of 12 h in serum-free medium. The cells were then warmed to 37 ˚C, rinsed with PBS, fixed with 3.5% paraformaldehyde (PFA) for 10 min, followed by permeabilization with warm Triton X-100 for 10 min and rinsing with PBS. For actin filament staining, samples were incubated with Alexa Fluor 488 phalloidin (Invitrogen) (diluted in 5% FBS in PBS) at room temperature for 20 min, and followed by wash buffer (5% FBS, 0.05% sodium azide in PBS) for 15 min. For focal adhesion staining, samples were incubated with monoclonal mouse anti-vinculin (diluted in 5% FBS in PBS) (Sigma-Aldrich, Oakville, ON, Canada) at room temperature for 15min, followed by incubation with Alexa Fluor 546 conjugated rabbit anti-mouse immunoglobulins (Invitrogen, Canada) diluted in 5% FBS in PBS for 15 min. After each treatment the cells were incubated for 15 min with wash buffer. Finally, nuclear staining was performed on ice by washing the sample with PBS, followed by incubation with DAPI (diluted in cold PBS) for 10 min. After rinsing with PBS, the plates were mounted onto microscope slides with DABCO Antifade (Sigma-Aldrich, Oakville, ON, Canada) and imaged with an A1R laser scanning confocal microscope (LSCM) using a 60X water immersion objective (Nikon, Mississauga, Canada).

Fluorescent staining of HFFs cultured in fibrous PET matrices was also carried out using 6 mm diameter FibraCel disks (New Brunswick Scientific, Edison, NJ, USA). The triplicate disks were placed in 24-well plate wells and coated with filtered solutions of either 25 μM BSL-spacer or BSL-RGDS in 10 mM phosphate buffer at pH 7.5 overnight at 4 ˚C.

The wells were then rinsed 3 times for 5 min each time with PBS to remove any unbound proteins. Subsequently, 50 µL of a concentrated cell suspension with approximately 20,000 cells in serum-free medium was seeded onto each disk and incubated at 37 ˚C for 2 h to allow for cell attachment. 1 ml of serum-free medium was then added to each well and the cells were incubated for an additional 24 h. After that, the disks were incubated with 2 µM solutions of calcein-AM in PBS for 45 min at 37 ˚C. Calcein-AM is a membrane-permeable dye for the determination of the cell viability. Upon being transported into live cells, the nonfluorescent acetoxymethyl (AM) ester group is cleaved by intracellular esterases and converted to a green-fluorescent calcein. Fluorescent microscopy images of live cells were then taken with an A1R laser scanning confocal microscope (Nikon, Canada) at 488 nm. 85 optical slices were obtained along the vertical z-axis (corresponding to a depth of 2.65 µm per slice) for both BSL-RGDS and BSL-spacer samples. Images were projected onto the x-y plane with ImageJ for the ease of presentation.

4.3 Results and Discussion

4.3.1 SPR Studies of Surface Adsorption of Diblock Proteins

Dilute solutions of BSL-spacer and BSL-RGDS proteins are able to passively adsorb onto hydrophobic materials (such as PS, treated glass, and PET) through self-assembly into a monolayer film. In order to characterize this self-assembly process, several experiments were carried out to study surface adsorption of the proteins. One such study used SPR-based biosensors, since they are able to detect surface affinity in real time by monitoring the

change of mass when proteins adsorb onto a treated sensor surface. In order to obtain hydrophobic surfaces, the Au sensor chip was spin-coated with 0.1% (w.t.) polystyrene in toluene at 2000 rpm for 1 min to create an ultrathin PS surface film. Figure 4-1 shows a representative example of the SPR signal of an Au sensor chip before and after coating with PS. The position of the minimum in the reflectance signal (the so-called "dip") shifted due to presence of the PS coating on the Au sensor chips. As we have elaborated, the angle of the incident light to sustain the surface plasmon excitation depends on the refractive index of a material, which in turn depends on the mass of the material at the free surface of the metal film. Accumulation of materials on the metal surface can be accurately determined by monitoring the change of the reflected light intensity or the shift in the SPR angle (the dip shift). The 7 pixel dip shift as shown in Figure 4-1 can be converted to 7000 RU (resonance unit) using the relationship of 1 pixel corresponding to 1000 RU. Since 1 RU is equal to 1 pg/mm^2 and the density of the polystyrene for coating is 1.04 g/cm^3, the thickness of the thin layer of the PS on the Au sensor chip was roughly 7 nm.

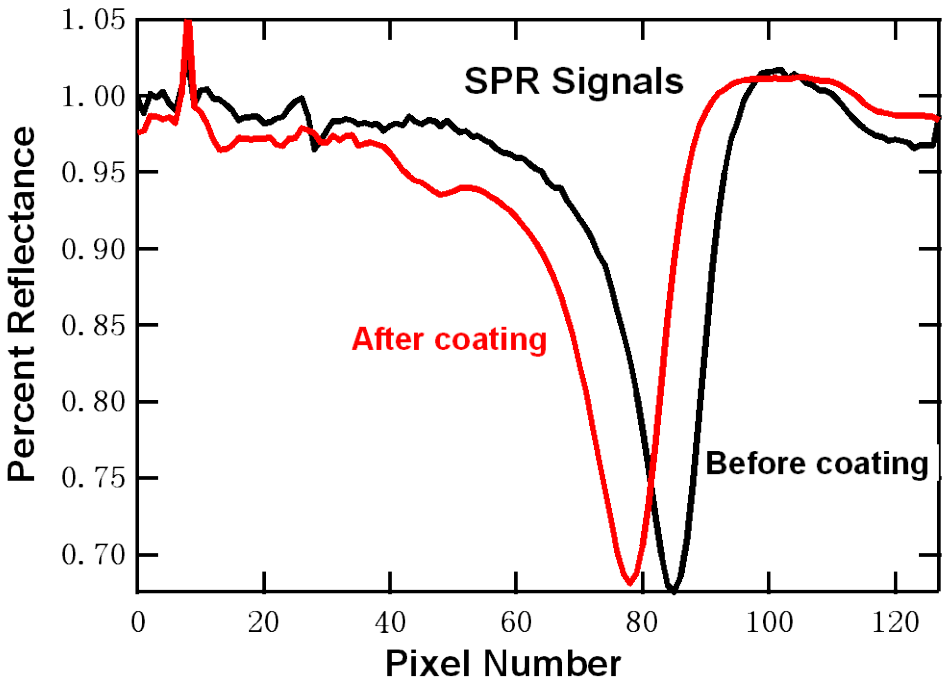

Figure 4-1 Dips in reflectivity from the SPR sensor chip before coating with PS (black dashed line) and after coating with PS (red solid line). The dip shift in this case 7 pixels.

Figure 4-2 shows the SPR signals in response units (RU) for adsorption and desorption of six diblock protein species. All six diblock proteins exhibited similar adsorption onto the PS-coated Au surfaces, with approximately 500 RU signals obtained in steady state conditions of flow of protein solution across the PS-coated Au sensor chips. The signals, a measure of the quantity of adsorbed protein, reach quickly reach a stable value even after being washed by buffer solution through the sensor channels for several hours (the initial rapid drop in signal at the start of the buffer wash period is presumably due to the loss of poorly associated proteins). The final steady-state adsorption signals were 550±50 RU for the BSL-spacer, 560±50 RU for the BSL-RGDS and 520±50 RU for the BSL-YIGSR. Since 1RU=0.1 ng/cm^2, this corresponds to surface protein densities of 55±5 ng/cm^2 for the BSL-spacer, 56±5 ng/cm^2 for the BSL-RGDS and 52±5 ng/cm^2 for the BSL-YIGSR. Similarly,

the final steady-state adsorption signals were 500±20 RU for the BSS-spacer, 490±50 RU for the BSS-RGDS and 480±80RU for the BSS-YIGSR, which correspond to the surface protein densities of 50±2 ng/cm^2 for the BSS-spacer, 49±5 ng/cm^2 for the BSL-RGDS and 48±8 ng/cm^2 for the BSS-YIGSR. Since the area of a single β-sheet domain is approximately 6.5 nm^2 [71] and the molecular weight of the β-sheet domain is 7204 Da, the maximum surface density (correponding to a perfectly packed monolayer) is approximately $1\text{cm}^2/6.5\text{nm}^2 \times (7204\text{g/mol}/6.02 \times 10^{23}\text{/mol}) = 184$ ng/cm^2. The surface protein densities inferred from the SPR data are much less than theoretical calculations, possibly due to several effects. First, since the BSL-spacer and BSL-RGDS adsorb from a flowing solution across the SPR biosensor, the adsorption process is limited by the diffusive flux of protein from the laminar low onto the surface. This is a relatively inefficient process compared with solution casting from a quiescent sample (indeed, another passive adsorption method briefly described below yielded substantially higher surface densities). Second, the soluble spacer domain acts as a steric barrier to adsorption of one protein in the immediate neighborhood of an already bound protein. This steric effect, although always a factor limiting the kinetics of adsorption of these proteins, is particularly limiting for adsorption of proteins in flows, as the spacer chains of the adsorbed proteins strongly perturb the flow profile of the solution of flowing proteins, leading to enhanced heterogeneity of adsorption. Nevertheless, the result of essentially irreversible adsorption of proteins at a relatively high surface coverage (approximately 30%) is quite good a flow-based, non-directed assembly process in a 1 h time window.

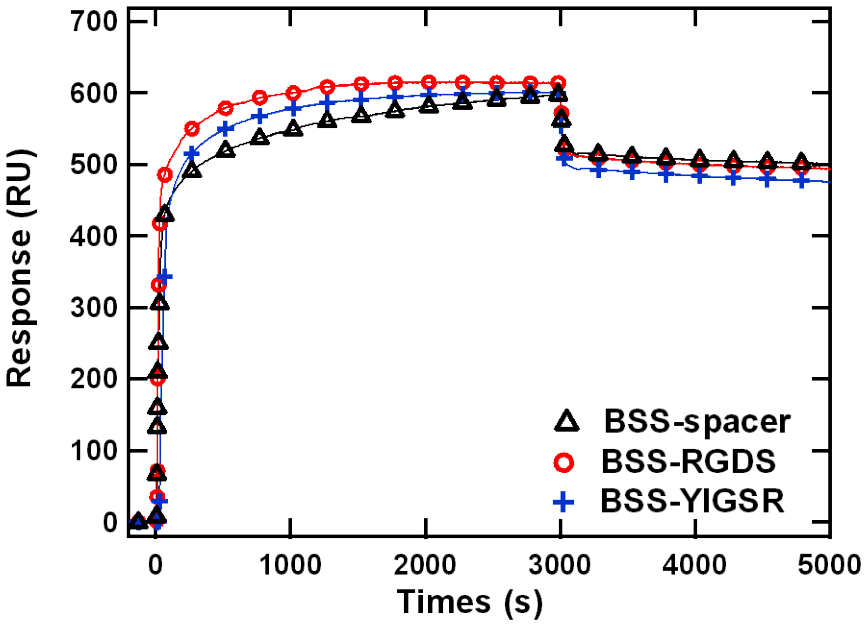

Figure 4-2a Sensorgrams of BSS proteins. The signals for proteins adsorbed onto PS coated Au sensor chips are roughly 500 RU after 50 min of flow with 250 ul of 100 μM solutions of BSS proteins in 10mM phosphate buffer at pH 7.5, and then washed with 10mM phosphate buffer at pH 7.5 for more than 1 hour.

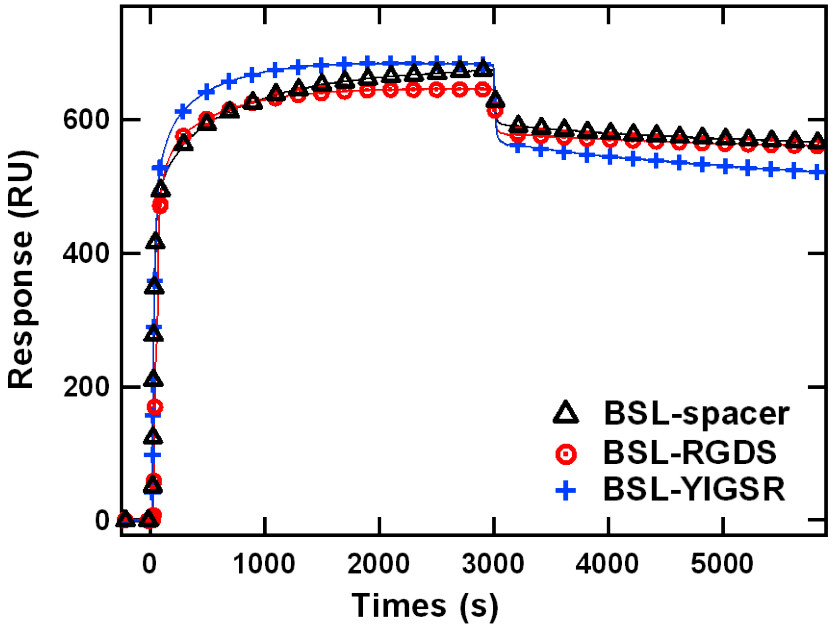

Figure 4-2b Sensorgrams of BSL proteins. The signals adsorbed onto PS coated Au sensor chips are roughly 570 RU after 50 min of flow with 250 ul of 100 μM solutions of BSL proteins in 10 mM phosphate buffer at pH 7.5, and then washed with 10 mM phosphate buffer at pH 7.5 for more than 1 hour.

Parallel studies of passive adsorption from a quiescent solution were shown to give higher final surface coverage (but without providing any kinetic data). These studies, performed by Dr. Scott Dick, utilized proteins labelled with ^{125}I via their tyrosine residues, allowing of radiographic detection of the surface coverage of proteins. The ^{125}I –labelling studies, described briefly below, show that passive adsorption yields a final monolayer coverage of approximately 140 ng/cm^2, and also that there were no appreciable competitive adsorption effects among the different diblock construct. Therefore, for subsequent cell studies, coated surfaces were always prepared by passive protein adsorption overnight to maximize adsorption.

Figure S-4-1 (*Supplementary materials*) shows the surface adsorption of the ^{125}I-labeled BSL-RGDS in both PBS buffers and IMDM media with FBS when they were passively adsorbed onto the PS surfaces for 50 days. IMDM media with FBS was used to assess the stability of the protein surface coating in physiological media with competitive adsorption effects of serum proteins. The BSL-RGDS in both solutions demonstrates similar surface adsorption curves. The surface density of the BSL-RGDS adsorbed onto PS surfaces decreased rapidly for the first 72 h (3 days) due to the fact that the protein molecules overlapping with others come off rapidly. The BSL-RGDS was supposed to form monolayer on the PS surfaces after 384 h (16 days) when its surface density became steady in both solutions. Therefore, the protein in PBS buffers created a monolayer on PS surfaces with adsorbed signals of 130-140 ng/cm^2, which was a little bit lower but still agreed well with the theoretical estimation. A similar result was exhibited by the protein in IMDM media with FBS. A signal of 120-130 ng/cm^2 was adsorbed onto the PS surface to create a monolayer.

Together, it shows that the monolayer formed with BSL proteins is sufficiently robust to support both serum-free and serum-containing cell cultures.

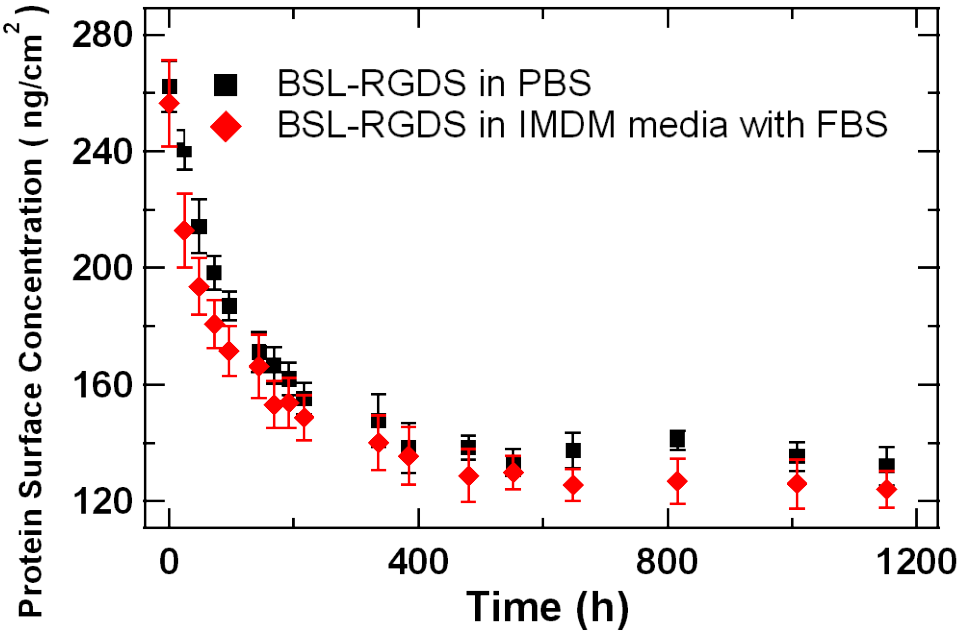

Figure S-4-1 Adsorption of BSL-RGDS onto PS surfaces.

In order to demonstrate the relative surface activities of BSL-spacer and BSL-RGDS, ^{125}I- labeled BSL-RGDS and non-labeled BSL-Spacer in 10 mM phosphate buffer, pH 7.5 were mixed together at different ratios and adsorbed onto PS substrates overnight. As shown in the Figure S-4-2 (*Supplementary materials*), the amount of ^{125}I-labeled BSL-RGDS adsorbed onto the substrate linearly increased with the fraction of BSL-RGDS in the mixed solutions with the correlation coefficient R^2=0.9976. This result demonstrated that the protein compositions coated onto PS surfaces were identical with the compositions of the bulk solution used for coatings, which implied that BSL-spacer and BSL-RGDS had similar surface activities, and the surface density of the ligand RGDS was tunable simply by adjusting the relative solution concentration of two proteins.

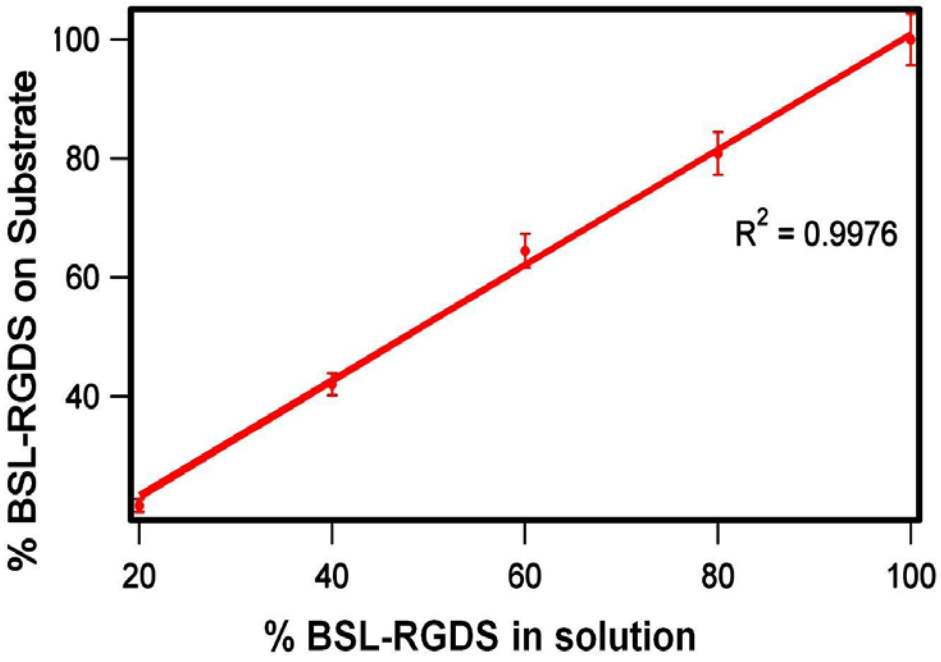

Figure S-4-2 Relationship of amount of adsorption of BSL-RGDS onto PS surfaces and amount of BSL-RGDS in the bulk solution.

4.3.2 Adhesion and Viability of Cells on Protein-Coated Surfaces

The interactions between material surfaces and cells play an important role in cellular behavior. The affinity and density of bioactive ligands embedded on the material surfaces to which cells are exposed is a key factor for such interactions, thereby influencing or determining cell adhesion, migration and proliferation [147,148]. A cell responds differently to various ratios of the density of the ligands, while different cell types respond differently to a single ligand at a fixed density. Therefore, there is the possibility to control cell behavior through controlling the density of the ligands, thereby regulating cell-surface interactions. The central purpose of this chapter is to demonstrate tunable cell adhesion based on

adjusting the density of the RGDS ligand by examining the response of different cell types on the surfaces coated with various ratios of BSL-spacer and BSL-RGDS.

We first studied the responses of two common types of adhesion-dependent cells, HFFs and C2C12s, on the surfaces coated with various ratios of BSL-spacer and BSL-RGDS proteins, in order to evaluate the effect of RGDS ligand density on cell adhesion and spreading. Untreated PS surfaces were prepared for these studies by coating with mixtures of BSL-spacer and BSL-RGDS at various ratios, and then incubating the coated surfaces with HFF and C2C12 cells in serum-free conditions for 24 h. Figure 4-3 shows representative images of cell adhesion and morphology on the surfaces coated with various ratios of BSL-RGDS. On the surfaces coated with only BSL-spacer, most HFFs and C2C12s remained rounded and unattached after 24 h of culture. Notably, HFFs started to attach and spread on the surfaces coated with as little as 2.5% of BSL-RGDS proteins, while C2C12s started to attach and spread on the surfaces coated with 10% of BSL-RGDS. Both cell types spread very well on the surfaces coated with pure BSL-RGDS solutions. The density of the RGDS ligands affects the attachment and morphology for both HFF and C2C12 cells. HFFs first stayed round and unattached without RGDS ligands on the surface, then they started to elongate and attach as the density of RGDS ligands on the surface increased, and finally cells became well-spread and highly polarized morphology. The C2C12s demonstrated the similar behavior as HFFs except that C2C12 cells spread on the substrates with less polarized morphology when the density of RGDS ligands increased. Based on these results, we can conclude that cell attachment and spreading generally increased with increasing amount of BSL-RGDS. Further evidence for the positive effects of BSL-RGDS protein

density on cell response was obtained from subsequent studies of the metabolic activity of HFFs and C2C12s on the surfaces coated with combinations of BSL-spacer and BSL-RGDS, and from immunohistochemistry studies of the focal adhesions and actin stress fibers that form in response to adhesion of cells to BSL-RGDS coated surfaces, as discussed below.

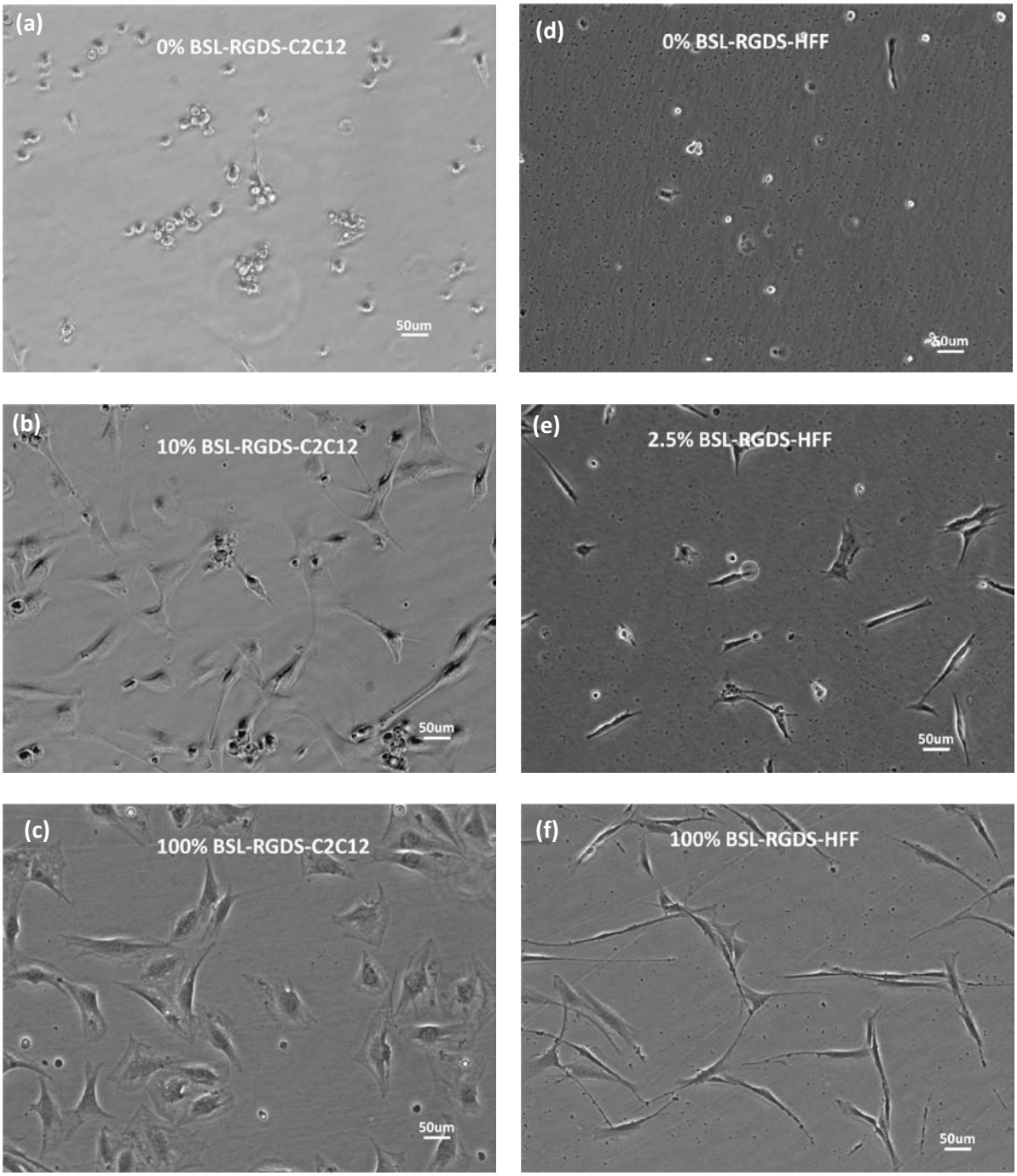

Figure 4-3 Phase contrast images of C2C12s (a-b) and HFFs (d-e) on protein coated polystyrene dishes after 24 h in culture. Substrates were coated with a mixture of BSL-spacer and BSL-RGDS with different ratios.

The metabolic activity of the HFFs and C2C12s on the protein coated PS substrates was investigated using the Roche WST-1 assay, which directly measures cellular metabolic activity through the bioreduction of tetrazolium salt to formazan. The formazan dye correlates to the number of viable cells and is measured using ELSA reader with absorbance at 440 nm. In these studies, metabolic activity was investigated as a function of RGDS ligand density through varying the ratio BSL-spacer and BSL-RGDS on the PS surface. These studies were also restricted to HFF and C2C12 cells that were actually attached to the substrate, as only attached and viable cells are of interest. Figure 4-4 shows relatively metabolic activity of HFFs and C2C12s, as indicated by absorbance at 440 nm, after culturing for 24 h as a function of amount of BSL-RGDS coated onto the surfaces. The metabolic activity of C2C12s and HFFs increased rapidly with the amount of BSL-RGDS on the surface, reaching 85% of maximal metabolic activity for surface coatings with approximately 10% RGDS ligand. The metabolic activity of both cells types reached an apparent maximum value at approximately 50% BSL-RGDS coverage, suggesting that the effect of the RGDS ligand on cell viability saturates at some value [180,181]. These results confirmed that the de novo protein BSL-RGDS is capable of improving the attachment and viability of cells, and that these effects are density dependent. However, it also appears that the adhesion and spreading of the cells is cell dependent at any given density of BSL-RGDS, and that in any case the metabolic activity eventually becomes insensitive to increasing density of the RGDS ligand.

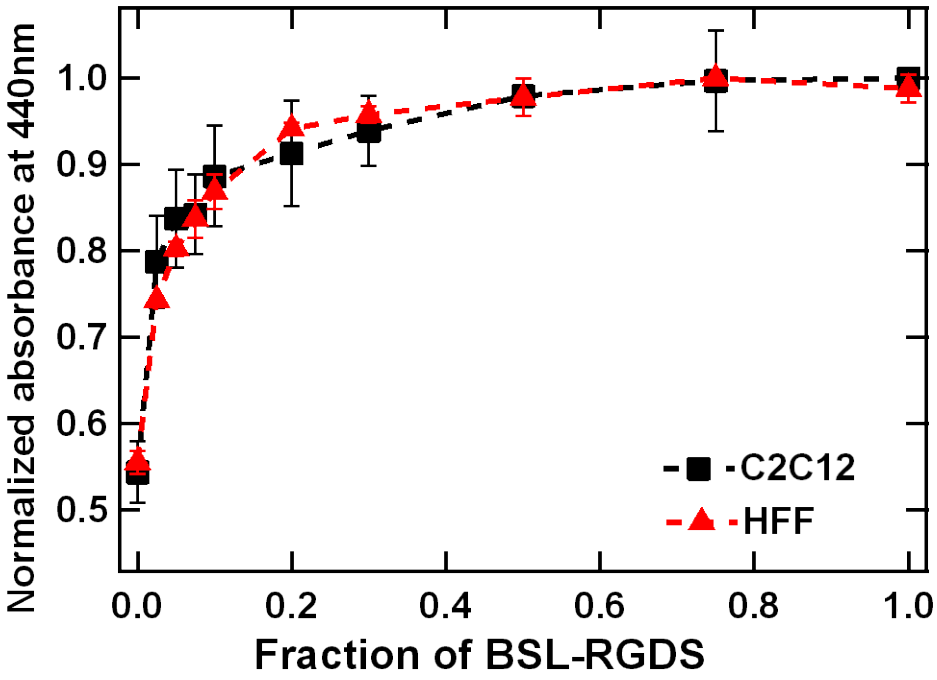

Figure 4-4 Normalized absorbance at 440 nm of formazan produced by HFFs and C2C12s incubated for 3 h in the presence of the WST-1 reagent on substrates with varying composition of BSL- spacer and BSL-RGDS proteins.

4.3.3 Fluorescence Microscopy Studies of Cells on Surface Coatings

Cells adhere to and interact with their extracellular environment through dynamic protein assemblies, called focal adhesions, as sketched in Figure 4-5. Focal adhesions are generated in response to the binding of ligands such as the RGDS peptide to the extracellular domains of integrins, and the subsequent intracellular signalling cascade initiated by these binding events. Integrins thus serve both to anchor cells and to provide dynamic links between the extracellular and intracellular environments through bi-directional signal transduction and organization of intracellular cytoskeletal and signalling elements. In

particular, integrin signalling is linked with the recruitment of proteins forming the focal adhesion complex and with cytoskeleton assembly of actin filaments. In turn, these actin filaments reorganize into larger stress fibers, which lead to further integrin clustering and enhanced binding to the extracellular environment. Well-developed aggregates formed by ECM proteins, integrins, and cytoskeletal proteins on each side of the membrane can be detected by immunofluorescence microscopy [168].

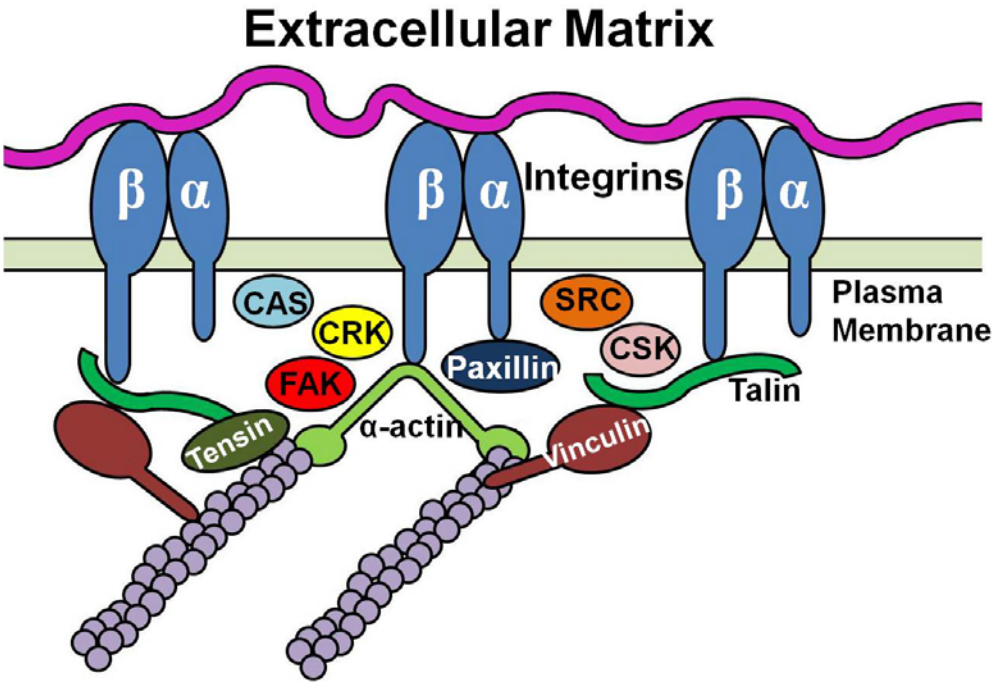

Figure 4-5 Sketch of integrins linking the ECM with cytoskeletal filaments through the focal adhesion complex.

To evaluate the ability of surfaces coated with BSL-RGDS protein layers to induce focal adhesion formation and enhance cytoskeletal reorganization, immunohistochemistry studies of HFFs and C2C12s cultured on smooth protein coated surfaces were conducted. HFFs and C2C12s were cultured on untreated PS dishes coated with BSL-spacer or BSL-

RGDS protein by exposure to 25 μM solutions for 12 h under serum-free conditions. The adherent cells were subsequently fixed and fluorescently stained for F-actin and vinculin (a prominent member of the focal adhesion complex; see Figure 4-5) as previous described. Figure 4-6 shows fluorescence microscopy images of fixed and stained cells on the surfaces coated with either BSL-spacer or BSL-RGDS proteins. Well-developed actin filaments terminating at focal adhesions were formed in the strongly adherent and polarized adherent cells on the BSL-RGDS coated PS surfaces for both C2C12s (Figure 4-6b) and HFFs (Figure 4-6d-e). In contrast, poorly attached C2C12s (Figure 4-6a) and HFFs (Figure 4-6c) were observed on BSL-spacer coated PS surfaces, neither of which exhibited well-developed F-actin or focal adhesions. By analyzing with ImageJ software package, the average area of HFF cells on the surface coated with BSL-spacer is 150±30 μm^2, the average length is 18±3 μm and average breadth is 9±2 μm. The average area of HFF cells on the surface coated with BSL-RGDS is 4600±600 μm^2, the average length is 170±40 μm and average breadth is 40±10 μm. The HFF cells increase by roughly 30 times in size on the surface coated with BSL-RGDS compared with that on the surface coated with BSL-spacer. The number of focal adhesions formed on the BSL-RGDS coated surfaces was 45±4 and the average area of focal adhesions was (3±4) μm^2. These results demonstrated that surfaces coated with BSL-RGDS were effective in inducing strong cell adhesion via integrin-RGDS peptide binding and subsequent focal adhesion formation and cytoskeletal organization for both HFFs and C2C12s cell types. Moreover, together with the previous phase microscopy results, this study suggests that cell response, including cell adhesion, spreading, and internal cytoskeletal re-organization, can be regulated by adjusting the ratio of BSL-RGDS and BSL-spacer proteins used for surface coatings.

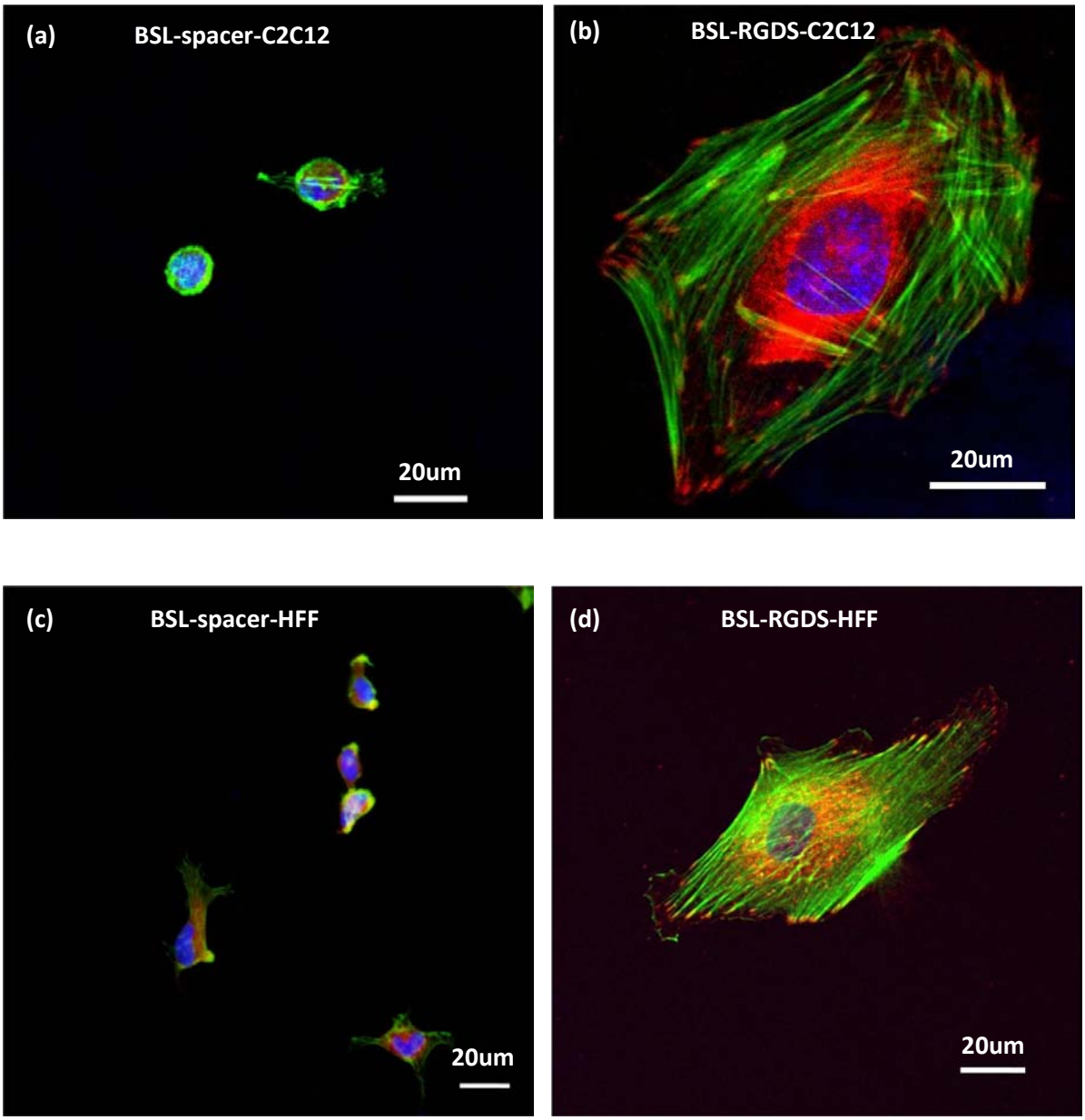

Figure 4-6 Representative fluorescence microscopy images of HFFs and C2C12s cultured on untreated PS dishes coated with BSL-spacer or BSL-RGDS for 12h in serum-free conditions. Actin is indicated in green, vinculin is indicated in red, and the cell nucleus is indicated in blue: (a) C2C12s cultured on a BSL-spacer coated PS surface; (b) C2C12s cultured on a BSL-RGDS coated PS surface; (c) HFFs cultured on a BSL-spacer coated PS surface; (d-e) HFFs cultured on a BSL-RGDS coated PS surface.

4.3.4 Fluorescence Microscopy Studies of Cells on Porous Substrates

Porous 3-D scaffolds can also be functionalized with bioactive ligands by the passive adsorption of dilute protein solutions, as with the case of smooth 2-D substrates presented above. This possibility was investigated using 3-D scaffold of non-woven PET mesh coated with bioactive (BSL-RGDS) and bioneutral (BSL-spacer) proteins to generate protein-functionalized porous 3-D matrices. PET has similar physical properties and equilibrium contact angle with PS substrates. The response of HFFs on PET meshes coated with either BSL-spacer or BSL-RGDS were evaluated by staining the cells with the live stain calcein-AM after culturing in serum-free conditions for 24 h. Figure 4-7 and Figure 4-8 demonstrate the 2-D projections of a series of confocal microscopy images taken at various depths of the meshes. The total depth of image was 222.6 μm (85 optical slices with a depth of 2.65 μm per slice) in z-axis for both the BSL-spacer and BSL-RGDS coated meshes. For the case of the BSL-spacer-coated PET mesh (Figure 4-7), the HFFs remained mostly rounded and poorly attached. The 2-D projections for top third slices (with a depth range of 0-90.1 μm), middle third slices (with a depth range of 92.75-129.85 μm) and bottom third slices (with a depth range of 132.5-222.6 μm) show the distribution of cells at various depth ranges. Most cells were found in the depth range of 0-90.1 μm, implying that the cells did not migrate into the mesh. However, in the case of the BSL-RGDS-coated PET mesh (Figure 4-8), HFFs adhered well to the treated PET surfaces, migrated into the mesh, and polarized along the PET fibers in the mesh. The 2-D projections for top slices (with a depth range of 0-90.1 μm), middle slices (with a depth range of 92.75-129.85 μm) and bottom slices (with a depth range

of 132.5-222.6 μm) show that the cells distributed well in all depth ranges. It is clear that the HFFs exhibited similar behavior on the protein coated porous 3-D scaffolds as they did on the more idealized 2-D coatings. This suggests that the surface-active diblock protein system studied in this thesis may be a simple and robust way to functionalize many traditional synthetic polymer scaffold materials (such as PLGA) used in cell and tissue engineering applications by passive adsorption from a solution of bioactive protein species.

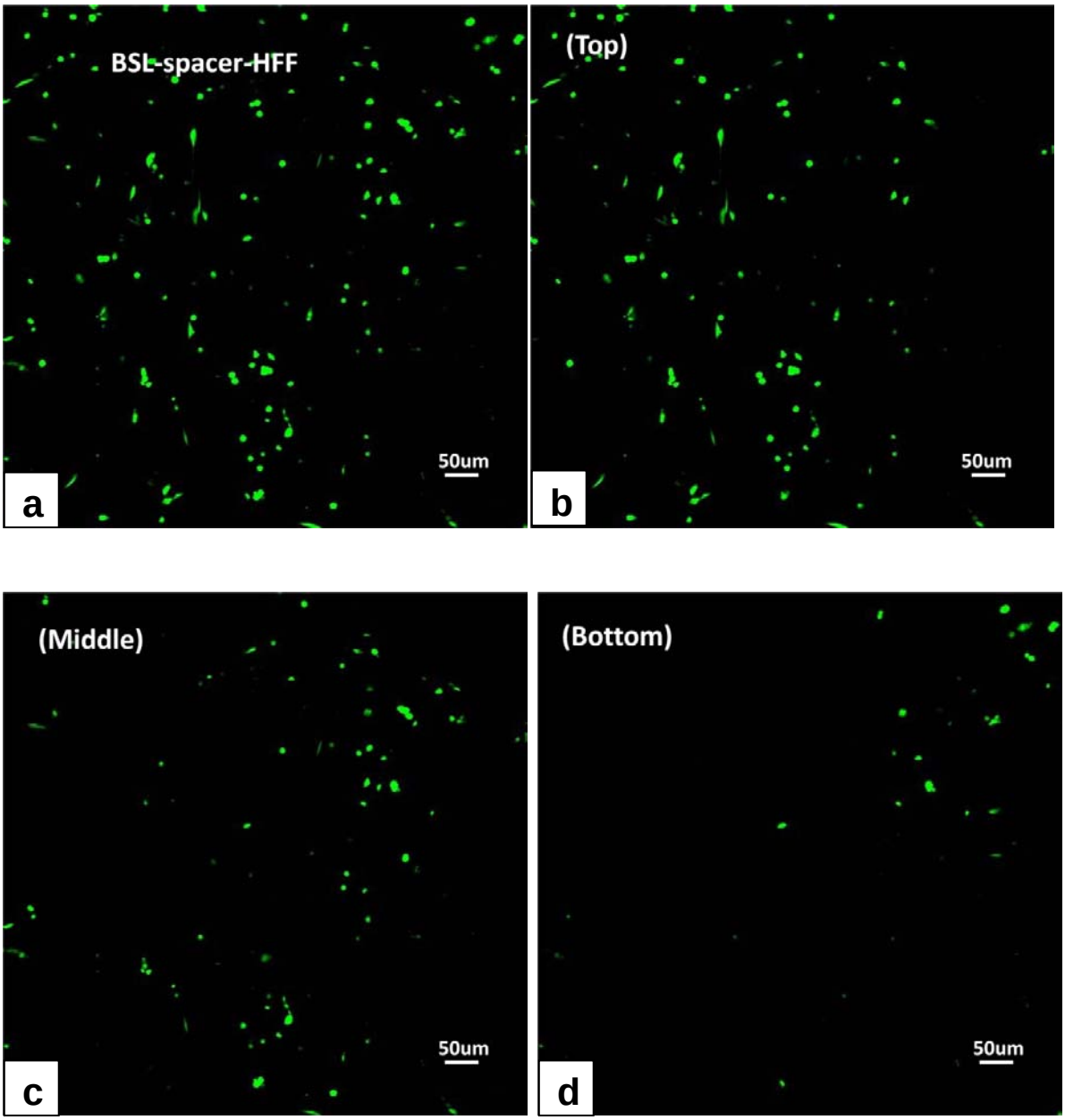

Figure 4-7 2-D projections of confocal microscopy images of HFFs cultured on BSL-spacer-coated PET mesh in serum-free conditions for 24 h. The HFFs were stained with Calcein-AM which is shown in green. (a) 2-D projections of all confocal microscopy images; (b-d) 2-D projections of confocal microscopy images for top, middle and bottom, respectively.

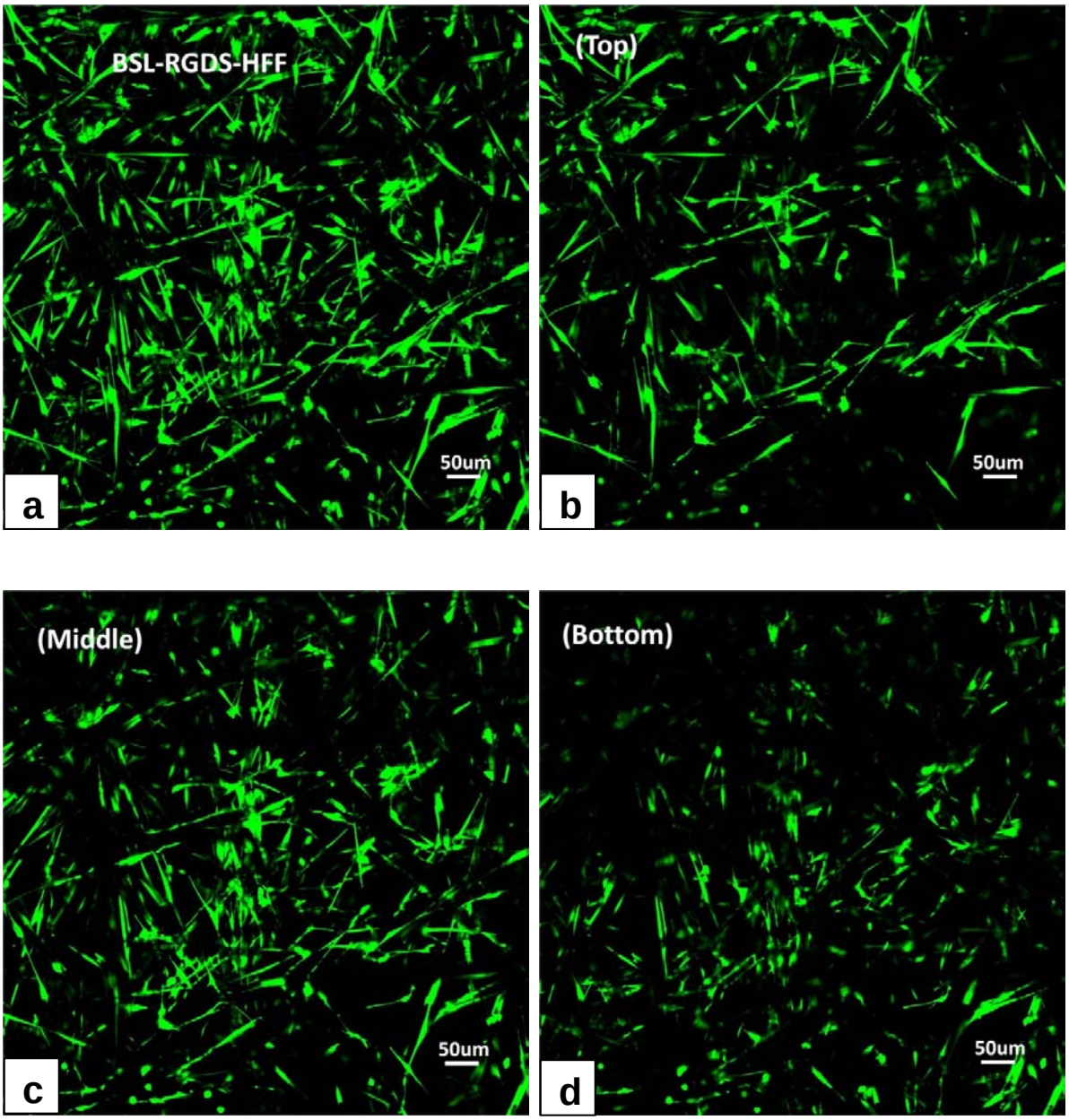

Figure 4-8 2-D projections of confocal microscopy images of HFFs cultured on BSL-RGDS-coated PET mesh in serum-free conditions for 24 h. The HFFs were stained with Calcein-AM which is shown in green. (a) 2-D projections of all confocal microscopy images; (b-d) 2-D projections of confocal microscopy images for top, middle and bottom, respectively.

4.4 Conclusions

In this chapter, a simple method for surface biofunctionalization through passive adsorption of BSL proteins was developed and characterized. By studying the adsorption of proteins to hydrophobic substrates using the SPR and ^{125}I radio labelling methods, it was shown that surface activities of BSL-spacer and BSL-RGDS proteins are similar and very robust, suggesting that the spacer and the bioactive domains do not interfere with surface adsorption domain of the proteins. Two adhesion-dependent cell lines, HFFs and C2C12s, were used to characterize the cell response to coatings of these two protein variants. The bioneutral BSL-spacer protein was shown to inhibit adsorption, spreading, and cytoskeletal remodeling of these cell types. On the other hand, the putative bioactive BSL-RGDS proteins exhibited the expected strong adsorption, spreading, and polarization of cells on coated surfaces. Furthermore, focal adhesions and F-actin stress fibers were observed for cells on the BSL-RGDS coated surfaces. These cell adhesion studies also implicitly demonstrated that surface adsorption domain did not interfere with the cell binding function of the terminal RGDS sequence. Thus, the data support the hypothesis that diblock proteins with independent assembly and biofunctional domains can de realized in practice. Moreover, since the BSL-spacer itself was shown to inhibit cell adhesion, it was shown by microscopy and cell proliferation assays that the cell response to surface coatings formed by passive adsorption of the diblock proteins could be titrated and controlled by tuning the ratio of bioneutral BSL-spacer and bioactive BSL-RGDS proteins in solution, providing a facile means of tailoring bioactivity of a surface. While this study focused on a single bioactive domain, the ubiquitous RGDS integrin-binding ligand, we believe that the method should be

applicable to diblock protein variants with other bioactive ECM peptide sequences. Expansion of the variants to include a broad range of terminal functional domains will be the next step in the development of a combinatorial biomaterials platform that will allow for custom combinations of bioactive ligands and other functional domains for particular cell types and applications. The next two chapters will explore the extension of this amphiphilic diblock motif to proteins with terminal functional domains that act to nucleate the growth of nanoparticles of inorganic materials.

Chapter 5

Surface-Active Proteins with Hydroxyapatite-Binding Domains

5.1 Introduction

Biomineralization is a highly regulated process in vivo by which living organisms produce inorganic minerals that are organized hierarchically across a range of dimensional scales [182,183]. Over 60 different kinds of minerals, including hydroxyapatite, carbonates, silicates, phosphates, metals and metal oxides, have been identified in organisms [182,183]. Biomimetic materials with properties similar to teeth [184-186], bones and cartilage [187-189] have been widely developed and studied in order to satisfy the high demand for bone and dentin–like biological hard tissues in regenerative medicine.

Mineralized tissues are hierarchically organized biocomposites of a structured organic matrix impregnated mainly with hydroxyapatite ($Ca_{10}(PO_4)_6(OH)_2$; HA) crystals [53]. A variety of extracellular matrix proteins have been proposed to play crucial roles in the biomineralization of HA in bone and dentin [53,190-191] by acting as nucleators or inhibitors, growth modifiers, or by recognizing molecules and self-assembling as scaffolds for mineral deposition [53, 192-194]. Although the detailed apatite crystallization process is not well characterized, and the detailed molecular recognition mechanisms between proteins

and mineral remain to be understood, it is postulated that interactions between mineral nuclei and soluble or immobilized matrix proteins kinetically control the biomineralization process [195].

Protein sequences related to biomineralization have been identified using several methods. He *et al.* [53] have shown that the mixture of the two peptide motifs [motif-A (ESQES) and motif-B (QESQSEQDS)] which are found in dentin matrix protein1 (DMP1) enhanced in vitro HA formation when immobilized onto a glass plate. Along with DMP1's motifs, Tsuji *et al.* [196] synthesized motifs using an artificial protein programmed library prepared from these two DMP1 motifs and selected motifs which accelerate HA formation without immobilization. Gungormus *et al.* [54] combinatorially selected two disulfide bond constrained peptides with higher and much lower binding affinity to hydroxyapatite from phage display. Both peptides, the strong binder (CMLPHHGAC) and the weak binder HABP2 (CNPGFAQAC), affected calcium phosphate formation. However, HABP1 accelerated and regulated the formation of crystalline calcium phosphate with much larger plate-shaped nanoparticles than did HABP2, and also increased the rate of transformation of the amorphous phase to the crystalline phase. Roy *et al.* [32] have screened and isolated other HA-binding peptides, such as peptide HA 6-1 (SVSVGMKPSPRP), and tested their selectivity for amorphous calcium phosphate and hydroxyapatite. The peptide HA 6-1 sequence (SVSVGMKPSPRP) exhibited higher binding affinity for hydroxyapatite and human tooth surface, which is rich in hydroxyapatite minerals, than for calcium carbonate and amorphous calcium phosphate [32].

A variety of bone mineral-binding proteins have been studied in detail for bone-specific applications, and fusions with other functional proteins have been created. Kaplan et al. [197,198] reported that a new functionalized spider silk-bone sialoprotein fusion protein was able to provide good support for cell viability and induce the deposition of calcium phosphate during osteoblast in vitro culture. A native FGF2 fused with a bone mineral-binding domain of osteocalcin exhibited a strong HA-binding affinity and significantly increased mitogenic activity and cellular differentiation of osteoblastic cells [199]. Kang et al. [200] showed that a new extracellular matrix protein with a cell adhesive RGD sequence and a bone mineral-binding domain of osteocalcin bound to HA and stimulated differentiation of MC3T3-E1 cells. Fusions of HA-binding peptides with surface-active proteins, however, have received less attention. In this study, we synthesized BSL-spacer protein variants with motif-A (ESQES) or motif-B (QESQSEQDS) at the terminus of the spacer domain (these variants are named BSL-5mer and BSL-9mer, respectively). At the same time, another HA-binding peptide, HABP1 (MLPHHGA), as was also fused to the terminus of BSL-spacer (this variant is named BSL-7mer). With these variants, we studied HA-binding affinity and the regulation of HA formation, as a first step toward development of protein surface coatings for bone tissue engineering scaffolding materials.

5.2 Materials and Methods

5.2.1 Materials and Reagents

The putative HA-binding variants were designed and synthesized as described earlier in Chapter 2. HA nanoparticles and mounting media were purchased from Sigma-Aldrich

(Oakville, ON, Canada). EZ-Link® Sulfo-NHS-LC-Biotin (Thermo Scientific) was purchased from Thermo Scientific (Wilmington, DE, USA). Alexa Fluor 488 streptavidin was obtained from Life Technologies (Burlington, ON, Canada). Primers were ordered from Integrated DNA Technologies (Toronto, ON, Canada). All other chemicals were purchased either from Sigma-Aldrich (Oakville, ON, Canada) or Fisher Scientific (Ottawa, ON, Canada).

5.2.2 *In Vitro* Binding of Peptides to HA

The cleaning procedure for preparing the HA nanoparticles before binding experiments was essential. A suspension of 15 mg of HA nanoparticles (mean size<200 nm) was prepared in a mixture of 100 µL of dH_2O and 900 µL of 1:1 methanol/acetone, and then sonicated for 20 min. The mixture was centrifuged and the supernatant was taken out. After that, the HA nanoparticles were resuspended in 1 ml of isopropanol, vortexed and sonicated for 20min. The HA nanoparticles were subsequently washed with dH_2O. The alcohol and acetone washes were used to remove any organic contaminants, and sonication was employed to improve the cleaning by physically removing the contaminants and dispersing the nanoparticles into the solution. Washing in dH_2O was used to remove any organic solvents remaining. The same cleaning procedure was performed in all experiments using HA particles.

Stock solutions of proteins (BSA, lysozyme, BSL-spacer and BSL-7mer) were prepared by mixing 250 µM of a given protein in a 10 mM phosphate buffer at pH 7.5. Solutions for binding experiments were prepared by combining 500 uL of each protein

solution with 15 mg of washed HA in a 2 ml eppendorf tube and agitating using a vortex mixer for 1 min. Three samples for each protein were prepared and placed in an orbital shaker running continuously at approximately 100 rpm. The concentration of the free, soluble protein in each sample was determined at 0, 0.5, 1, 2, 4, 8 and 24 h after mixing as follows. At the prescribed time points, three tubes of each sample were removed from the shaker and centrifuged at 5000 rpm for 5 min, creating a pellet of HA-nanoparticles (potentially with bound protein) and a supernatant solution of soluble protein. The concentrations of protein in the supernatant solutions were measured by observing UV absorbance at 280 nm with a NanoDrop 2000 UV-Vis Spectrophotometer (Thermo Scientific, Wilmington, DE, USA). The fraction of bound protein at a given time point was then inferred by subtracting the amount of soluble protein in the supernatant from the original amount in the prepared mixtures.

5.2.3 Sample Preparation for Electron Microscopy

For TEM studies of the nucleation and growth of HA on the proteins in solution, samples of 5 μM BSL-7mer and BSL-spacer were prepared in aqueous HA-reaction solution (1.2 mM $CaCl_2$ and 0.72 mM KH_2PO_4 at pH 7.5). The samples were then transfered to 1 K MWCO Spectra/Pro dialysis tubing (Fisher Scientific, Ottawa, Canada) and dialyzed against the same buffer while gently stirring on a plate stirrer for 5 days. Carbon coated TEM grids were then dipped into the solutions for 1 min, followed by wicking away the extra liquid on the TEM grids using a Filter paper (Qulitative circles 42.5 mm, Whatman™). The dried grids were stored in a desiccated container for subsequent TEM analysis.

SEM studies were also carried out to examine the HA nanoparticle binding affinity of BSL-7mer that has been previously immobilized onto a surface. For these studies, previously washed HA nanoparticles were re-suspended in dH_2O and filtered through a 0.2 μm Sterile Syringe Filter (Corning, NY, USA). Filtering of the cleaned HA nanoparticle solutions through 0.2 μm filter was used to remove all aggregates larger than 200 nm. Samples of 25 μM of BSL-7mer and BSL-spacer in 10 mM phosphate buffer at pH 7.5 were loaded onto polystyrene (PS) surfaces and passively absorbed overnight. Subsequently, the surfaces were rinsed three times with dH_2O for 5 min, to remove any poorly bound proteins. The PS surfaces were then put into contact with the HA solutions and incubated for 24 h placed in an orbital shaker run continuously at approximately 100 rpm. The resulting coated PS surfaces were dried in vacuum and stored in a desiccated container for subsequent SEM analysis.

The experiments were performed using JSM-7500F Scanning Electron Microscope (fitted with Energy dispersive X-ray spectroscopy (EDS)) (JEOL, Japan). SEM images were acquired using the "SEM" mode by setting the acceleration voltage at 5 kV and the emission current at 20 μA. TEM images were acquired using the "SEM" mode by setting the acceleration voltage at either 15 kV or 20 kV and the emission current at 20 μA. Focus, stigmatism adjustment, and bright and contrast are optimized before imaging. EDS was employed on the same samples prepared for TEM to obtain the information on the mineral elements [201]. EDS conditions were set as the acceleration voltage at 20 kV, emission current at 20 μA and magnification at X7500.

5.2.4 Preparation of Fluorescently-Labeled Diblock Proteins

To facilitate the study of HA-binding affinity, BSL-7mer and BSL-spacer (control) were biotinylated for subsequent binding by Alexa Fluor 488 streptavidin. Solutions of 1 ml of 2 mg/ml BSL-7mer and 1 ml of 2 mg/ml BSL-spacer were biotinylated with a 20-fold molar excess of EZ-Link® Sulfo-NHS-LC-Biotin (Thermo Scientific). The EZ-Link® Sulfo-NHS-LC-Biotin was first equilibrated to room temperature before use. Subsequently, a 10 mM solution of the biotin reagent was prepared and immediately added into the BSL-spacer and BSL-7mer solutions, respectively. The reaction solutions were then incubated on ice for 2 h. After that, the proteins were dialyzed against TBS buffer (50 mM Tris-HCl, pH 7.5, 150 mM NaCl) using 1 K MWCO Spectra/Pro dialysis tubing (Fisher Scientific, Canada) to remove the excess non-reacted and hydrolyzed biotin reagent from the protein solutions.

The proposed process by which biotinylated proteins bind to HA nanoparticles and are subsequently bound to fluorescently-labeled streptavidin is presented in Figure 5-1. The experimental steps performed for this process are as follows. First, approximately 5mg of HA nanoparticles are exposed to 5 mg/ml solutions of BSA in 0.1 M $NaHCO_3$ with 0.02% (w.t.) sodium azide at 4 °C for 1 h, followed by six wash cycles with TBS buffer to remove soluble BSA. The purpose of this BSA coating step is to minimize the effects of non-specific binding with HA nanoparticles. Next, 50 μM of N-terminal biotinylated BSL protein solution (either BSL-7mer or BSL-spacer as a control) in TBS buffer was added to the BSA-blocked HA solutions and incubated for 24 h at 23°C with shaking at approximately 100 rpm on an orbital shaker to allow BSL-7mer to displace bound BSA and bind to HA nanoparticles. After that, the soluble protein components in solution were removed from the

mineral samples by vacuum aspiration, followed by six wash cycles with TBS buffer. Fluorescence labeling of bound BSL proteins was carried out by adding 1 µg/ml of Alexa Fluor 488 streptavidin in labeling buffer (0.1 M $NaHCO_3$, 5mg/ml BSA, and 0.02% (w.t.) sodium azide) to the samples and incubating the mixtures at 23 °C with shaking at approximately 100 rpm on an orbital shaker for 30 min. Once again, soluble proteins in solution were subsequently removed after incubation by vacuum aspiration, followed by ten wash cycles with TBS buffer to eliminate the influence of non-binding BSL protein and streptavidin. Finally, the samples were mounted onto the microscope slides with 20 µL of mounting media and sealed for subsequent fluorescence microscopy studies. All samples were then visualized using an A1R laser scanning confocal microscope (Nikon, Missisauga, Canada).

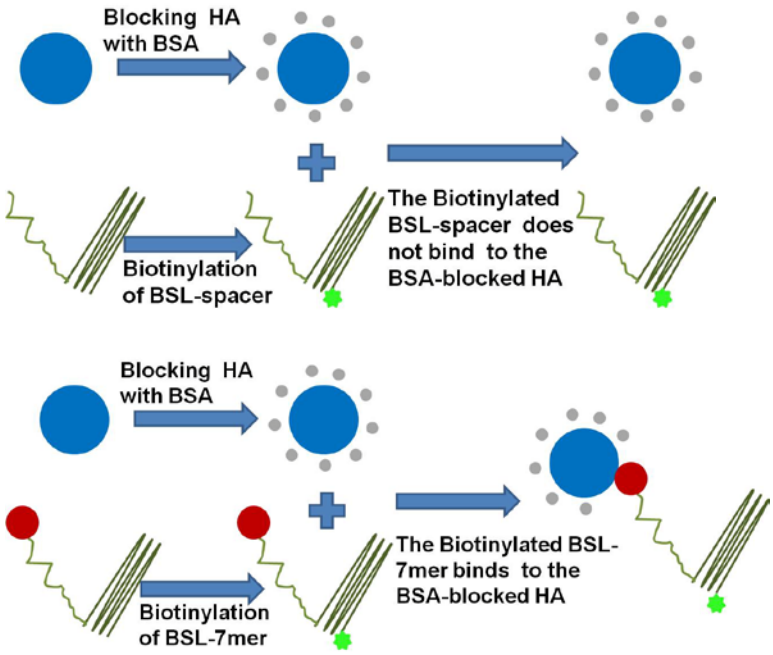

Figure 5-1 Hypothetical process of adsorption of biotinylated diblock proteins to HA nanoparticles, followed by binding of fluorescently-labeled streptavidin to the surface-associated biotinylated BSL proteins.

Another experiment was performed (as described below) to test if BSL-7mer proteins still retained an amphiphilic β-sheet domain capable of assembling at hydrophobic surfaces after binding of the functional 7mer terminal sequence with HA nanoparticles. The BSL-spacer and BSL-7mer proteins tend to aggregate each other with amphiphilic β-sheet blocks when they are mixed together. Therefore, the mixture of the biotinylated BSL-spacer and the BSL-7mer would be observed by confocal microscopy after staining with fluorescently-labeled streptavidin if the BSL-7mer protein retains β-sheet structure after binding with HA nanoparticles. The proposed process is presented in Figure 5-2. As before, approximately 5 mg of HA nanoparticles was coated by exposure to 5 mg/ml solutions of BSA in 0.1 M $NaHCO_3$ with 0.02% (w.t.) sodium azide at 4 °C for 1 h, followed by six wash cycles with TBS buffer to remove soluble BSA. Next, 50 μM of non-biotinylated BSL-7mer peptide solution in TBS buffer was incubated with the BSA-blocked HA nanoparticles for 24 h at 23 °C while shaking at approximately 100 rpm on an orbital shaker to achieve maximum binding capacity. The peptide solution was then removed from HA mineral sample by vacuum aspiration, followed by six wash cycles of the remaining HA mineral sample with TBS buffer. Next, 50 μM of biotinylated BSL-spacer in TBS buffer was added to the HA mineral sample and incubated with the sample for 24 h at 23 °C while shaking at approximately 100 rpm on an orbital shaker. The BSL-spacer solution was then removed by vacuum aspiration from the HA sample, followed by six wash cycles of the remaining HA mineral sample with TBS buffer. Subsequently, 1 μg/ml of Alexa Fluor 488 conjugated streptavidin in labeling buffer (0.1 M $NaHCO_3$, 5 mg/ml BSA, and 0.02% (w.t.) sodium azide) was added to the HA sample and incubated at 23°C while shaking at approximately 100 rpm on an orbital shaker for 30 min. Next, the solution containing streptavidin was

removed by vacuum aspiration and the remaining HA sample was washed 10 times with TBS buffer. The HA samples were then placed onto microscope slides with 20 μL of mounting media and sealed. All samples were visualized using an A1R laser scanning confocal microscope (Nikon, Canada).

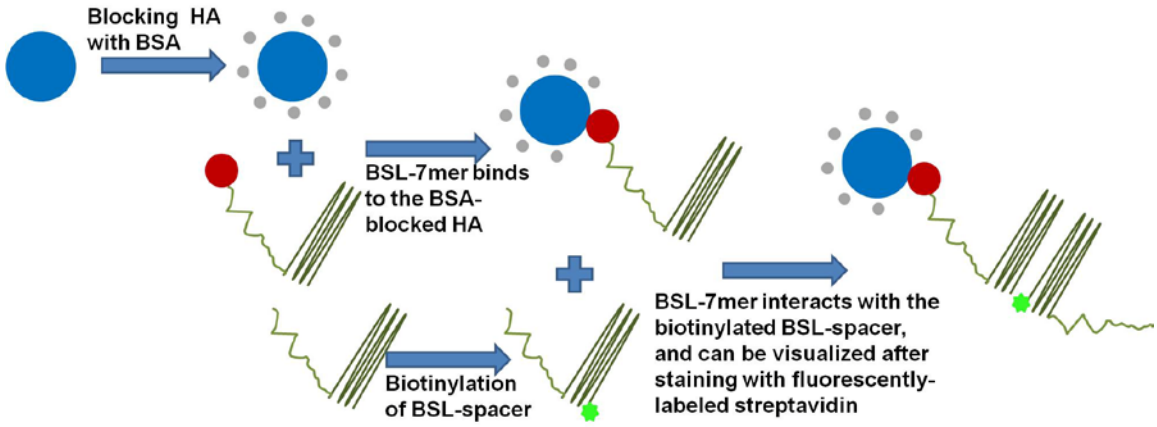

Figure 5-2 Hypothetical process to demonstrate the functionality of the β-sheet domain in the BSL-7mer after binding with HA nanoparticles.

5.3 Results and Discussion

5.3.1 Synthesis and Purification of HA-Binding Diblock Proteins

Several BSL diblock proteins variants with terminal HA-binding motifs were designed and synthesized for these studies. These include the BSL-7mer diblock protein that incorporates the HABP1 sequence (MLPHHGA)[54], the BSL-5mer diblock protein that incorporates the motif-A sequence (ESQES)[53], and the BSL-9mer diblock protein that incorporates the motif-B (QESQSEQDS)[53]. One important design criterion for these

proteins is the independence of the β-sheet and the HA-binding domains, as a functional amphiphilic β-sheet domain is crucial for preserving the ability of these proteins to self-assemble on hydrophobic surfaces. All three of these HA-binding BSL variants were successfully produced recombinantly in *E. coli* with high yields. The vectors PET-21d+ containing 5mer (ESQES), 7mer (MLPHHGA) and 9mer (QESQSEQDS) genes were constructed with the fragment-vector enzymatic ligation technique, as described previously. Primers encoding these HA-binding peptides are provided in Table 2-3 of Chapter 2.

BSL-5mer, BSL-7mer and BSL-9mer were expressed and purified using the methods described in Chapter 2. In particular, proteins recovered from inclusion bodies were purified using gel filtration with an FPLC to obtain high-level purity. A representative FPLC gel filtration purification trace is shown in Figure 5-3a. The fractions A3-A12 and B12 collected from gel filtration were visualized with an SDS-PAGE gel (Figure 5-3b). The proteins initially loaded onto the FPLC contained a significant quantity of impurities and fragments of various molecular weights, as shown in fractions A3-A6. The desired pure proteins were collected after fraction A8, since the eluted fractions after fraction A8 primarily contained single bands near 8 kDa as demonstrated by SDS-PAGE analysis. Figure 5-4 provides a summary of SDS-PAGE results for the three types of HA-binding diblock proteins at different stages of expression and purification. This figure shows that good expression and high level of purity (greater than 95%) using the FPLC gel filtration method were obtained for all these three HA-binding diblock proteins.

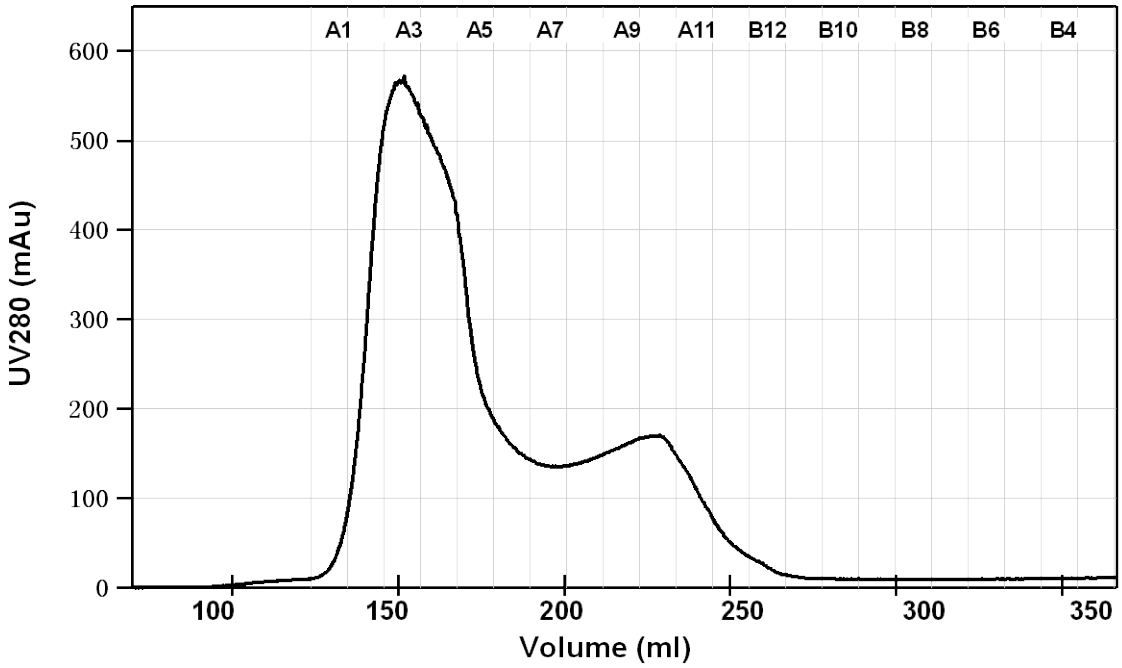

Figure 5-3a A representative purification trace of BSL-7mer using Gel-filtration with FPLC. The fractions A3- A12, B12 were visualized with SDS-PAGE.

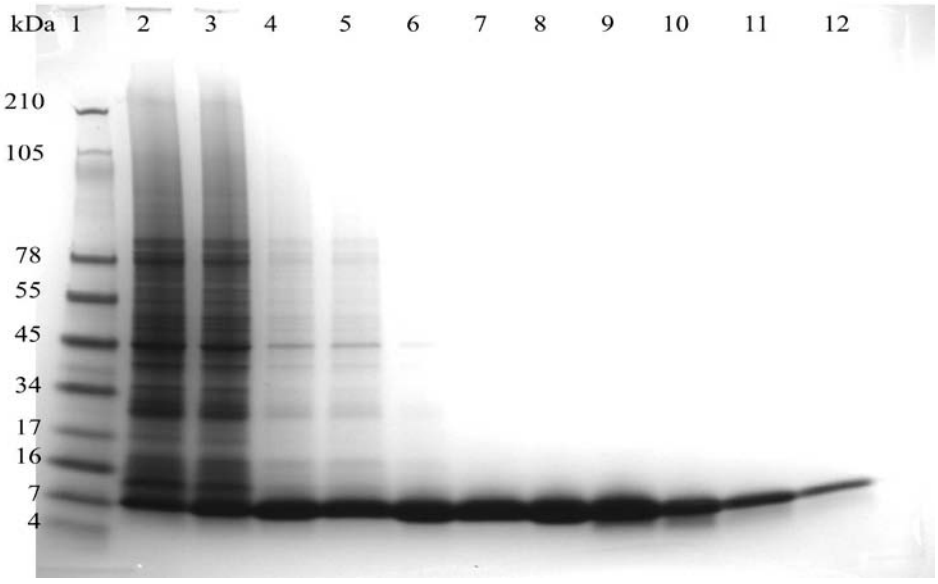

Figure 5-3b A representative coomassie stained SDS-PAGE gel (Tricine) to show the purification of BSL-7mer with FPLC gel-filtration. Lane1: SeeBlue Plus 2 standard. Lane2-12: fractions of A3-A12, B12 from FPLC gel filtration purification of BSL-7mer.

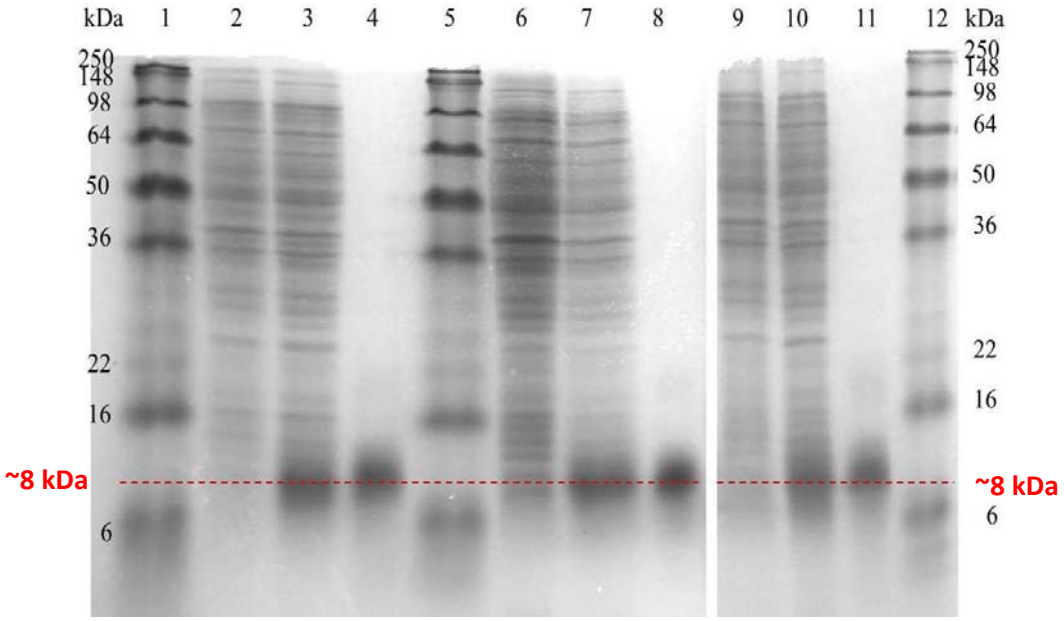

Figure 5-4 A coomassie stained SDS-PAGE gel to show the expression and purification of BSL-5mer, BSL-7mer, and BSL-9mer. The lanes contain the following: Lanes 1, 5 and 12: SeeBlue Plus 2 standard. Lane 2: BSL-5mer pre-induction. Lane 3: BSL-5mer 4h post-induction. Lane 4: purified BSL-5mer. Lane 6: BSL-9mer pre-induction. Lane 7: BSL-9mer 4 h post-induction. Lane 8: purified BSL-9mer. Lane 9: BSL-7mer pre-induction. Lane 10: BSL-7mer 4 h post-induction. Lane 11: purified BSL-7mer.

The molar masses of the purified BSL-5mer, BSL-7mer and BSL-9mer proteins were verified using Matrix-assisted laser desorption mass spectrometry (MALDI); results along with protein sequences are shown in Figure 5-5. The molecular weight determined by MALDI for BSL-5mer was 9385 Da, which is within 0.2% of its expected theoretical value of 9400 Da. Likewise, BSL-7mer demonstrates a single, sharp peak at 9590 Da, with a deviation of 0.2% from the theoretical value at 9560 Da. Finally, for BSL-9mer the measured MALDI value was deviation was 9843 Da, a value within 0.2% of its expected molecular weight of 9860 Da.

It is promising to use the surface-active proteins with HA-binding domains to control the mineralization of the calcium phosphate on the scaffold surfaces for bone and tooth implant substitutes. Three proteins allow us to carry out mineralization experiments in three ways by using only the BSL-7mer, the BSL-5mer and 9mer (QESQSEQDS), and the BSL-9mer and 5mer (ESQES). The BSL-7mer, the one that I focus on in the following studies, can induce mineralization by itself. The other two combinations (the BSL-5mer and 9mer, the BSL-9mer and 5mer) have the potential to act as triggers for calcium phosphate mineralization since the minerals cannot form on the surface coated with the BSL-5mer (or BSL-9mer) unless the 9mer (or the 5mer) is added.

BSL- 5mer:

M D Y E I K F H G D G D N F D L N L D D S G G D L Q L Q I R G P G G R V Q V H I H S S S G K V D F H V N N D G G D V E V K M H P W *G S T S G S G K P G S G E G S T K G T* **E S Q E S**

Length=89aa, MW=9385Da, PI=4.77

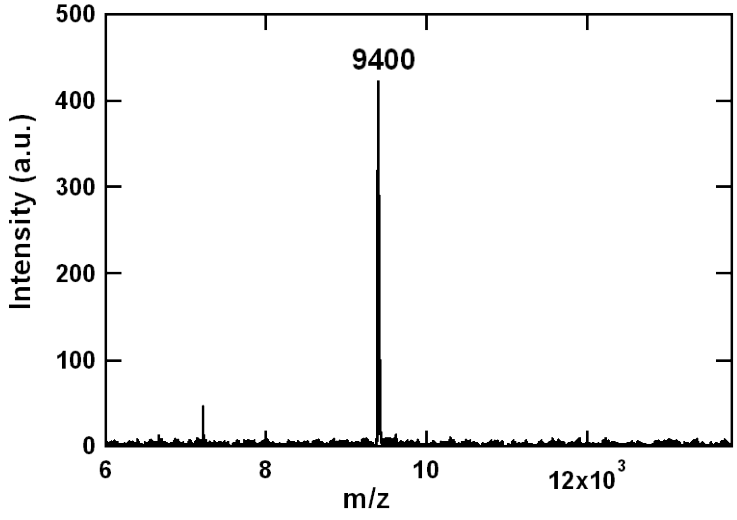

Figure 5-5a Sequence and MALDI spectrograph of BSL-5mer with a significant peak at 9400.

BSL- 7mer:

M D Y E I K F H G D G D N F D L N L D D S G G D L Q L Q I R G P G G R V Q V H I H S S S G K V D F H V N N D G G D V E V K M H P W *G S T S G S G K P G S G E G S T K G T* **M L P H H G A**

Length=91aa, MW=9568Da, PI=5.46

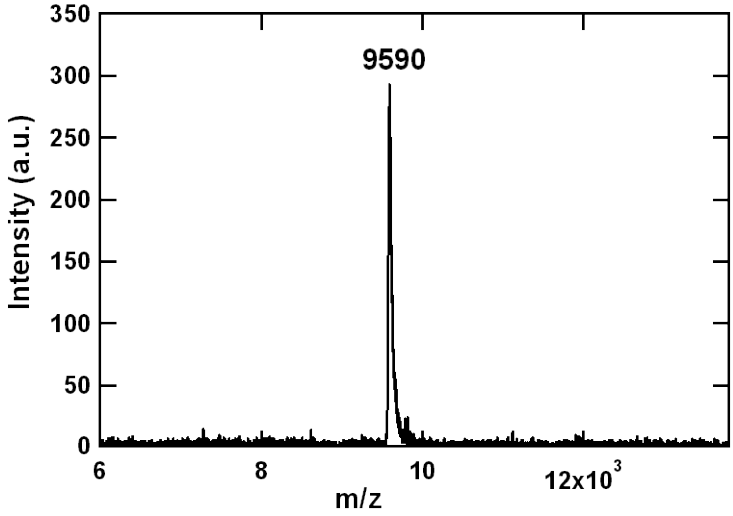

Figure 5-5b Sequence and MALDI spectrograph of BSL-7mer with a significant peak at 9590.

BSL- 9mer:

M D Y E I K F H G D G D N F D L N L D D S G G D L Q L Q I R G P G G R V Q V H I H S S S G K V D F H V N N D G G D V E V K M H P W *G S T S G S G K P G S G E G S T K G T* **Q E S Q S E Q D S**

Length=93aa, MW=9843Da, PI=4.65

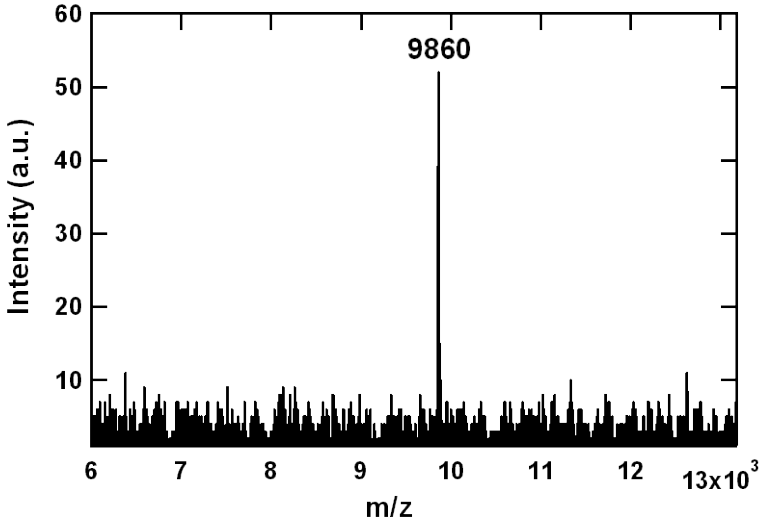

Figure 5-5c Sequence and MALDI spectrograph of BSL-9mer with a significant peak at 9860.

5. 3.2 Binding Affinity of BSL-7mer for HA

Solutions of BSA, lysozyme, BSL-7mer and BLS-spacer were incubated with HA nanoparticles for 24 h to determine the affinity of these proteins for HA. A semi-log plot of the percentage of peptides bound to HA versus time is shown in Figure 5-6. BSL-7mer proteins demonstrated immediate and significant binding affinity for HA with over 20% of initial peptides bound after the first 30 minutes, followed by a second fast binding regime from 2 to 8 h and a third regime characterized by a slow increase in bound protein (Figure 5-6, 5-7). All other peptides exhibited relatively low binding affinity for HA nanoparticles. BSA and lysozyme exhibited similar binding curves characterized by a gradual increase in binding during first 4 h before saturating at plateau value of about 9% of protein bound to HA. This behavior is indicative of weak, non-specific binding of protein to the mineral surface. Binding kinetics for BSL-spacer are somewhat more complex, characterized by a lag time with a slow binding rate, followed by a dramatic increase in binding from 2 to 4 h to a plateau value of bound protein. Such an abrupt increase of BSL-spacer binding suggests a second mechanism in addition to non-specific binding. One possibility is that the rapid period of binding is initiated by Ca^{2+} interaction sites (present in Asp or Glu residues) in the β-sheet domain, which are known to be abundant in mineralized tissues and to initiate HA growth [202,203]. The binding rate of the BSL-7mer proteins also suddenly increased during this period, consistent with the potential role of Ca^{2+} interaction sites in the β-sheet domain (as both proteins have identical β-sheet domains). BSL-spacer then reached binding plateau of about 25% of bound protein after 4 h of incubation, indicating that the binding sites in the β-sheet structure were saturated with HA.

The BSL-7mer showed significantly higher binding affinity for HA nanoparticles compared with all other peptides studied. After a rapid increase in binding during the first 30 min, the binding of the BSL-7mer to HA steadily increased during the 24 h of incubation to about 60% binding, with no sign of saturation. Given sufficient incubation time, these results suggest that BSL-7mer proteins would displace all weakly bound proteins and fully saturate the surfaces of the HA nanoparticles. After a transient period of weak non-specific binding, two modes of binding of BSL-7mer to HA nanoparticles are suggested by the results: (1) specific binding by the MLPHHGA HA binding sequence and (2) binding due to Ca^{2+} interaction sites in β-sheet structure (as was also seen for the BSL-spacer proteins). Since the β-sheet domains of BSL-7mer and BSL-spacer are identical, we can estimate contribution due to the β-sheet Ca^{2+} interaction sites (and any residual non-specific binding) to be at most 23% of binding events. Thus, the contribution due to the specific MLPHHGA binding sequence should account for at least 37% of the binding contribution. The fact that the bound BSL-7mer increases steadily from about 23% at 4 hours to about 60% at 24 hours suggests that the binding that occurs after 4 hours in solution is exclusively associated with specific binding events (and perhaps also conversion between non-specific or β-sheet binding and specific MLPHHGA binding with the passage of time). In any event, it can be concluded that main contributor to the significant differences in binding affinity between the BSL-7mer and the other proteins studied was the HA binding domain, MLPHHGA.

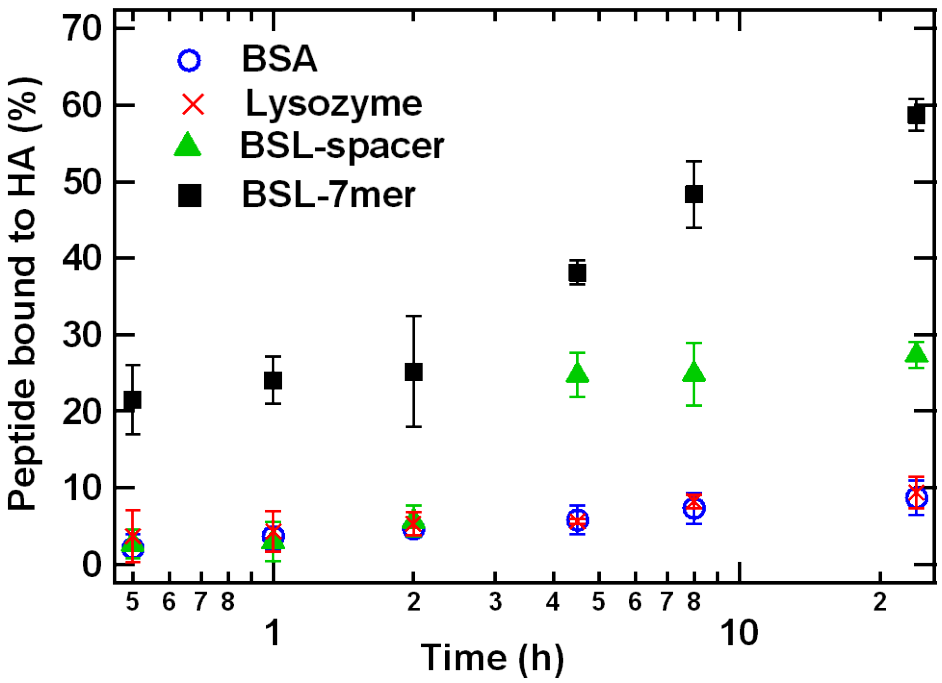

Figure 5-6 Semi-log of the percentage of peptides bound to HA nanoparticles versus time for the BSL-7mer and controls.

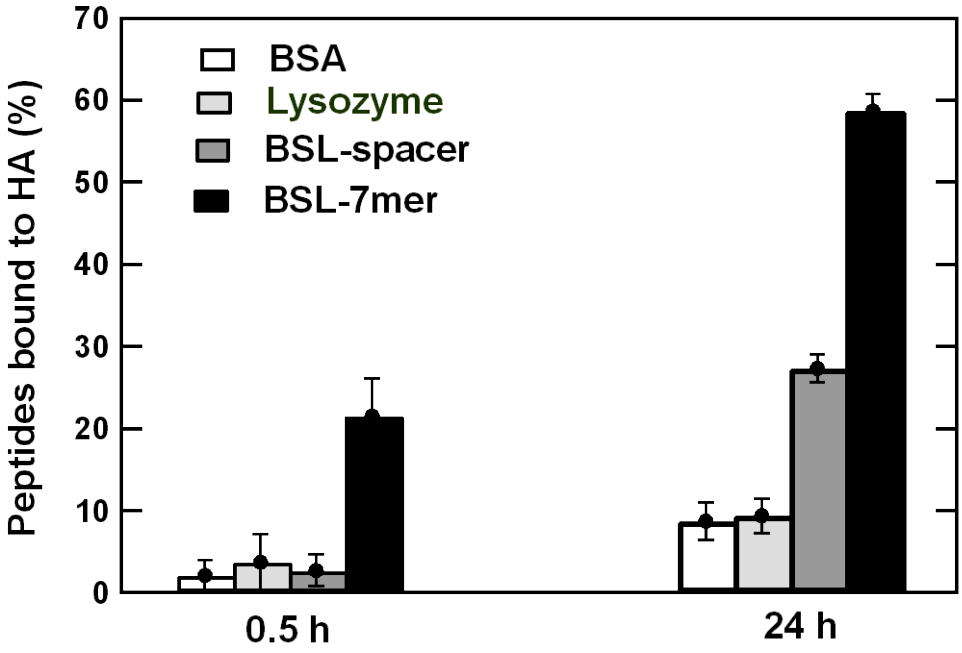

Figure 5- 7 The percentage of peptides bound to HA nanoparticles at 30 min and 24 h.

5.3.3 Electron Microscopy Studies of Calcium Phosphate Formation

Biomineralization experiments were carried out using 5 μM BSL-7mer and BSL-spacer solutions in 1.2 mM $CaCl_2$ and 0.72 mM KH_2PO_4 at pH 7.5. The reaction solutions were continuously stirred to facilitate proteins interactions with the mineralization solution. After 5 days, the reaction solution containing BSL-7mer contained appreciable precipitated material, while the solution containing BSL-spacer only showed a low level of precipitation. The precipitates from the reaction solutions were analyzed with TEM (JSM-7500F, JEOL, Japan). TEM observations revealed that only very tiny precipitates were present in the reaction solution with BSL-spacer (Figure 5-8a). Compared with the BSL-spacer solution (the control reference), the reaction in the presence of the BSL-7mer had a significant amount of larger precipitates, as shown in Figure 5-8b-d. At low magnification, we observed larger precipitates aggregating each other and forming structures. The shapes of the crystals were identified as the magnification increased, as shown in Figure 5-8c-d. The crystals formed in the presence of the BSL-7mer were large plate-like crystals growing to several hundred nanometers in width and length.

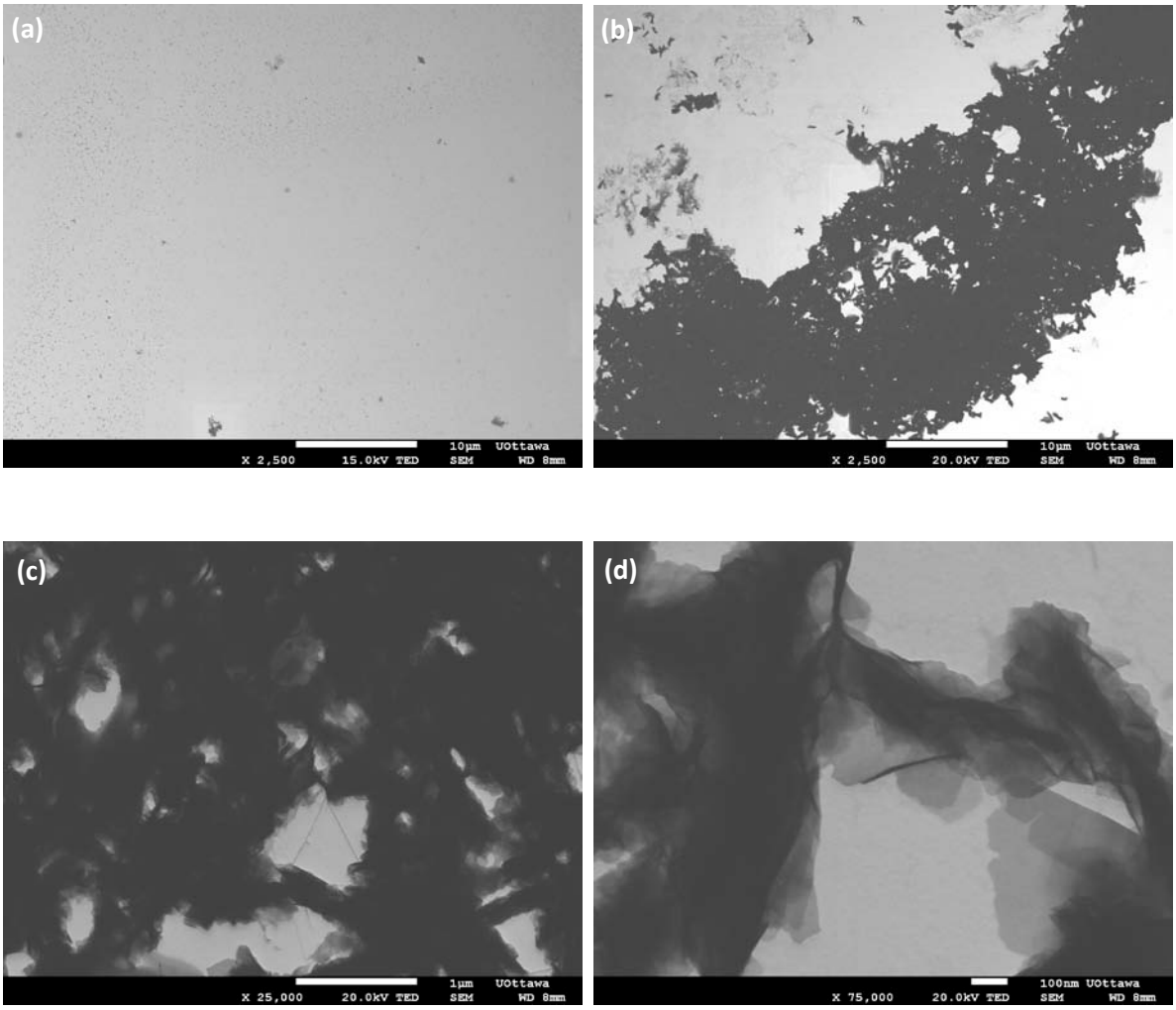

Figure 5-8 TEM images for mineralization formmation in the presence of BSL-7mer and BSL-spacer proteins. (a) Control sample with 5µM solution of BSL-spacer in 1.2 mM $CaCl_2$ and 0.72 mM KH_2PO_4 at pH 7.5 after 5days of reaction; (b-d) 5 µM solution of BSL-7mer in 1.2 mM $CaCl_2$ and 0.72 mM KH_2PO_4 at pH7.5 after 5 days of reaction.

The precipitates formed from the reaction of Ca^{2+} and PO_4^{3-} are likely to be either crystalline octacalcium phosphate (OCP; $Ca_8(HPO_4)_2(PO_4)_4 \cdot 5H_2O$) or hydroxyapatite (HA; $Ca_{10}(PO_4)_6(OH)_2$) depending on the pH of the solutions and the reaction conditions[196, 204-206]. EDS was used to identify the ratio of Ca and P in the precipitate crystals. EDS measurements of these precipitates showed that the ratio of Ca to P is Ca/P=1.3±0.1 (N=3), which matches the ratio expected for OCP (Ca/P=1.33). Based on the results above, we inferred that the precipitates for these reaction conditions were OCP not HA (which has a ratio Ca/P=1.67). The OCP has been regarded as a precursor of HA crystals in bone and tooth mineralization [207]. It contains a layer structure of alternating water molecule layers and apatite layers [208]. The transformation of OCP to HA by hydrolysis reaction occurs both in vivo and in vitro [209-211]. The conversion of OCP-HA in vivo is accompanied by a series of physicochemical changes, thereby affecting the tissue reaction around the location where osteoblastic cells are seeded and stimulating osteoblastic cell differentiation. The recent studies in biomaterials and tissue engineering have demonstrated that the OCP has the potential to be used as a synthetic bone substitute material and a scaffold material for exogenous osteoblastic cells due to its high osteoconductivity and biodegradability.

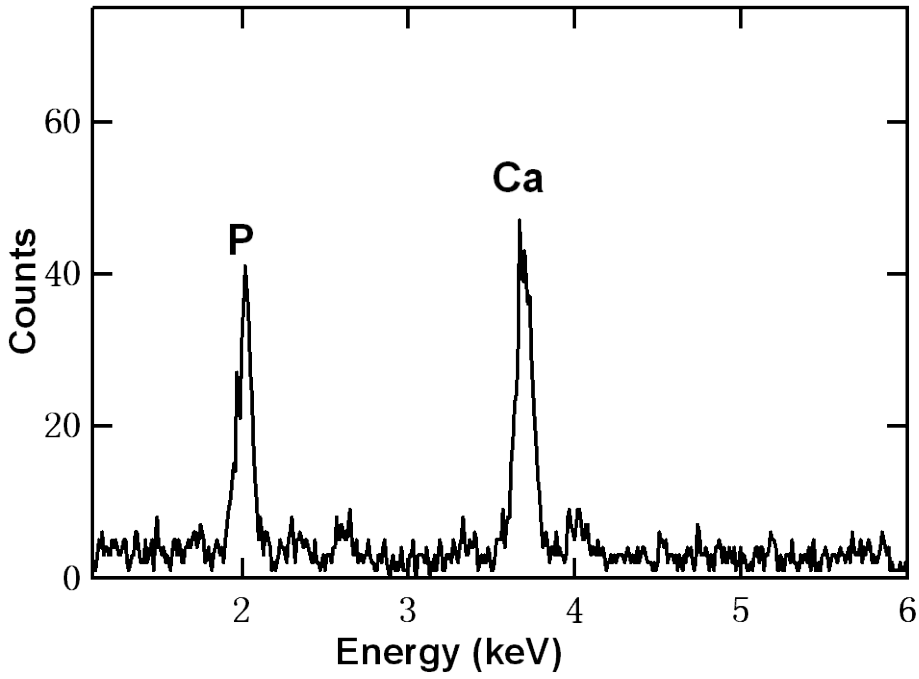

Figure 5-9 A representative EDS result for precipitates from BSL-7mer in a reaction solution of 1.2 mM $CaCl_2$ and 0.72 mM KH_2PO_4 at pH 7.5 after 5days. The atomic percentages of Ca and P are 56% and 44%, respectively, giving a ratio of Ca/P=1.3.

Since the reactions above were carried out in bulk solutions, we cannot definitely confirm that BSL-7mer protein is still able to bind to HA or OCP crystals after it is immobilized onto surfaces by passive adsorption. To study this possibility, we next performed the following binding experiment. First, PS surfaces were coated overnight at 4°C with a 25 µM solution of BSL-spacer or BSL-7mer in 10 mM phosphate buffer at pH 7.5. The PS surfaces were rinsed 3 times with dH_2O to remove unbound proteins. Subsequently, solutions of pre-washed HA nanoparticles were put in contact with the protein-coated PS surfaces overnight under gently shaking. Figure 5-10a shows SEM images of the control study using the BSL-spacer protein. It is evident that there are very few bound HA particles for the control. Figure 5-10b-c shows SEM images of bound HA on the

surfaces coated with BSL-7mer. The SEM images clearly demonstrate bound HA nanoparticles distributed fairly evenly on the surface. Since we previously demonstrated that diblock proteins form monolayers on surfaces by self-assembly under the low concentration, uniform distribution of HA nanoparticles on the surface coated with BSL-7mer is likely to be due to the distribution of the HA-binding domain (7mer) on the surface. Because the density of the ligands can be controlled by the composition of the protein solutions (BSL-7mer+BSL-spacer), it is possible to control the distribution of the HA on the scaffold surfaces and regulate the hard tissue regeneration. A high magnification image of bound HA (Figure 5-10c) indicated the presence of clusters of bound HA particles. The aggregation may be due to the interaction of functional domains with HA particles and the preparation for SEM samples. This experiment, although very basic, did prove that BSL-7mer was able to bind to HA particles after immobilization onto the PS surface.

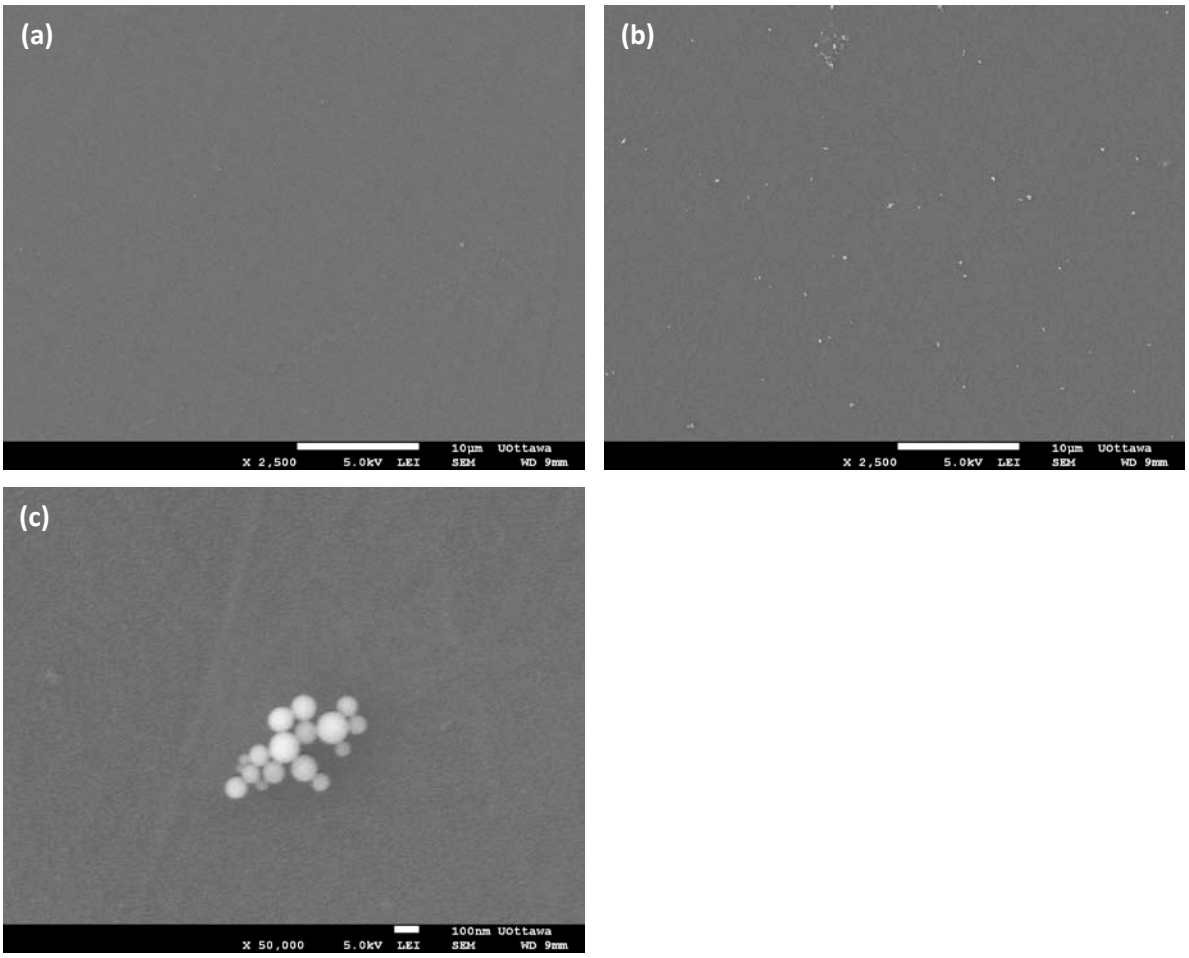

Figure 5-10 SEM images for binding of HA nanoparticles to BSL-spcaer and BSL-7mer coated surfaces. (a). Control sample with HA on a PS dish coated with a 25 µM solution of BSL-spacer in 10 mM phosphate buffer at pH 7.5; (b-c). HA on PS dish coated with a 25µM solution of BSL-7mer in 10 mM phosphate buffer at pH 7.5.

5.3.4 Studies on Binding of BSL-7mer to HA using Fluorescence

The use of fluorescent labeling provided the means to characterize the binding affinity of BSL-7mer to HA nanoparticles, and also to indirectly demonstrate that BSL-7mer retained its surface-active β-sheet structure after binding to HA particles. Biotinylation of

BSL-spacer and BSL-7mer was carried out first. We chose one of the most popular types of biotinylation reagent, (EZ-Link® Sulfo-NHS-LC-Biotin (Thermo Scientific) which reacts efficiently with primary amino groups (-NH_2) to form stable amide bonds) to label BSL-spacer and BSL-7mer proteins. NHS-activated biotins target the side chain of lysine (K) residues and the N-terminus of each polypeptide in BSL-spacer and BSL-7mer, allowing for the biotinylation of the proteins. The efficacy of biotin-labeling depends on the distribution of amino groups in the BSL-spacer and BSL-7mer proteins, their concentration, and the amount of biotin reagent used. Experiments performed in this chapter used a 20-fold molar excess of biotin reagent to label 1 ml of 2 mg/ml proteins, which yielded 4-6 biotin groups per antibody molecule according to the protocol (Thermo Scientific Inc., Mississauga, Canada).

Biotinylated BSL-spacer and BSL-7mer were incubated with BSA-blocked HA nanoparticles. After incubating for 24 h, samples were thoroughly washed and incubated with Alexa Fluor 488 streptavidin for 30 min to fluorescently tag the biotinylated proteins attached to HA. A washing step after staining aimed to eliminate soluble and non-specifically bound streptavidin. Fluorescence confocal microscopy was then used to visualize the location of the bound peptides. Figure 5-11a shows relatively little binding of BSL-spacer peptide (the control) to HA after incubating for 24 h. Figure 5-11b, however, indicates significant binding of BSL-7mer to HA after incubating for 24h. These fluorescence microscopy studies verify that BSL-7mer has a dramatically enhanced binding affinity to HA nanoparticles compared with the BSL-spacer control.

We also studied whether BSL-7mer was still able to self-assemble on the hydrophobic surfaces after binding to HA nanoparticles. To do so, non-biotinylated BSL-7mer was first to reacted with HA nanoparticles for 24 h. Subsequently, biotinylated BSL-spacer was added to this solution containing non-biotinylated BSL-7mer associated with HA nanoparticles, and allowed to incubate for another 24 h. If the amphiphilic β-sheet structures of the BSL-7mers bound to HA are not compromised, the β-sheet structures of the soluble biotinylated BSL-spacer and the bound BSL-7mer should dimerize (to protect the hydrophobic surface of the β-sheet structures from the aqueous solution). The existence of such interactions may be visualized after the proteins were stained with Alexa Fluor 488 and the samples were to remove soluble and non-specifically bound proteins and free unassociated chromophores. Figure 5-12 shows the fluorescence microscopy images of mixtures of proteins and HA particles. Since only BSL-spacer was biotinylated, and it has already been shown that BSL-spacer does not bind as strongly to HA nanoparticles as the BSL-7mer proteins, the only explanation for the fluorescent signal associated with HA nanoparticles in the images is that conjugation of the non-biotinylated, HA-bound BSL-7mer with soluble, Alexa Fluor 488 labeled, biotinylated BSL-spacer has occurred due to intermolecular association of the amphiphilic β-sheet domains of the two types of BSL proteins. Therefore, we may infer that BSL-7mer still possessed surface-active β-sheet structure after binding to HA particles.

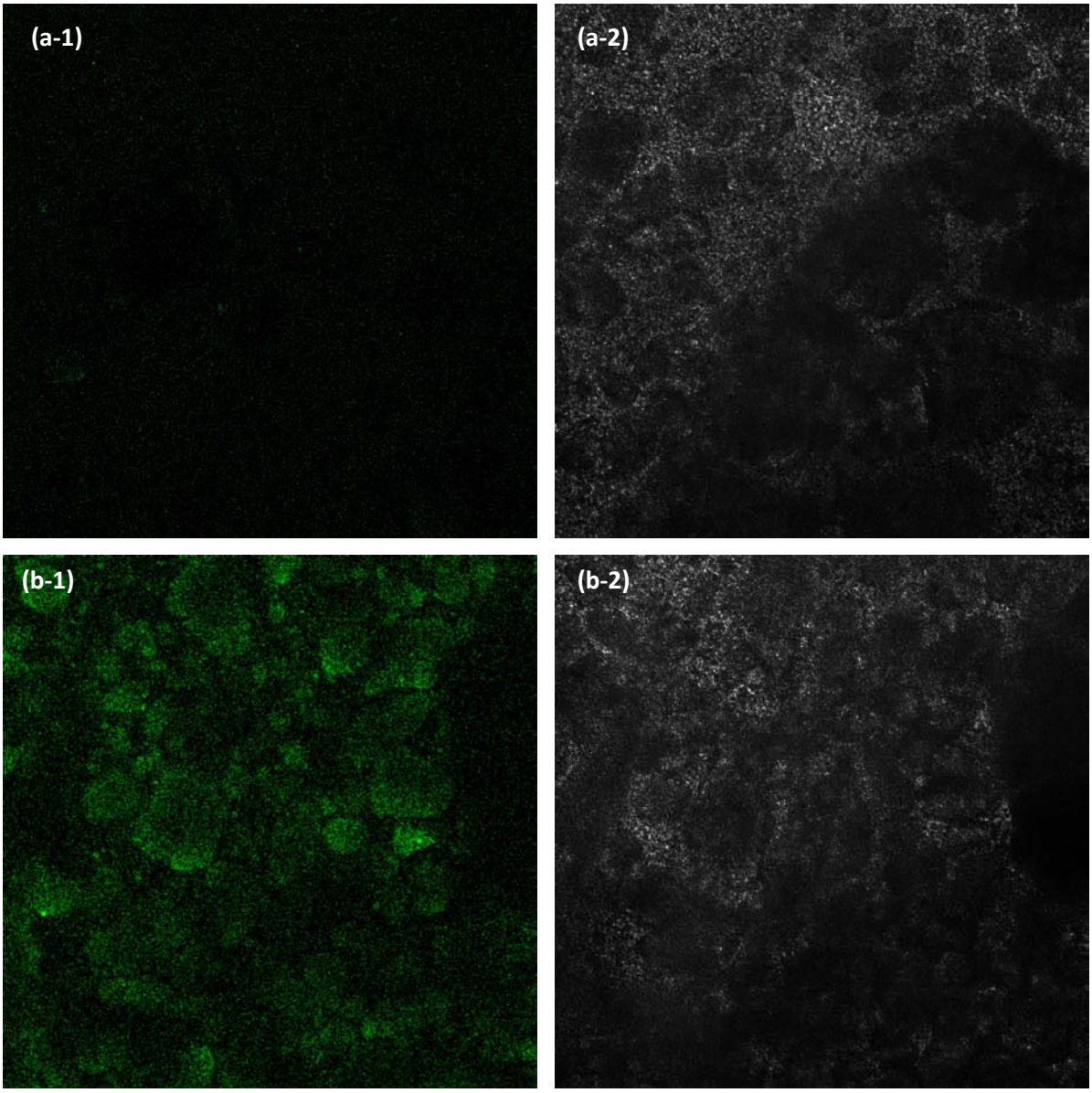

Figure 5-11 Binding ability test with biotinylated BSL-proteins. (a) Images of HA particles after incubating with BSL-spacer. (a-1) The Fluor 488 image of HA particles after incubating with BSL-spacer; (a-2) The phase contrast image of HA particles after incubating with BSL-spacer. (b) Images of HA particles after incubating with BSL-RGDS. (b-1) The Fluor 488 image of HA particles after incubating with BSL-7mer; (b-2) The phase contrast image of HA particles after incubating with BSL-7mer.

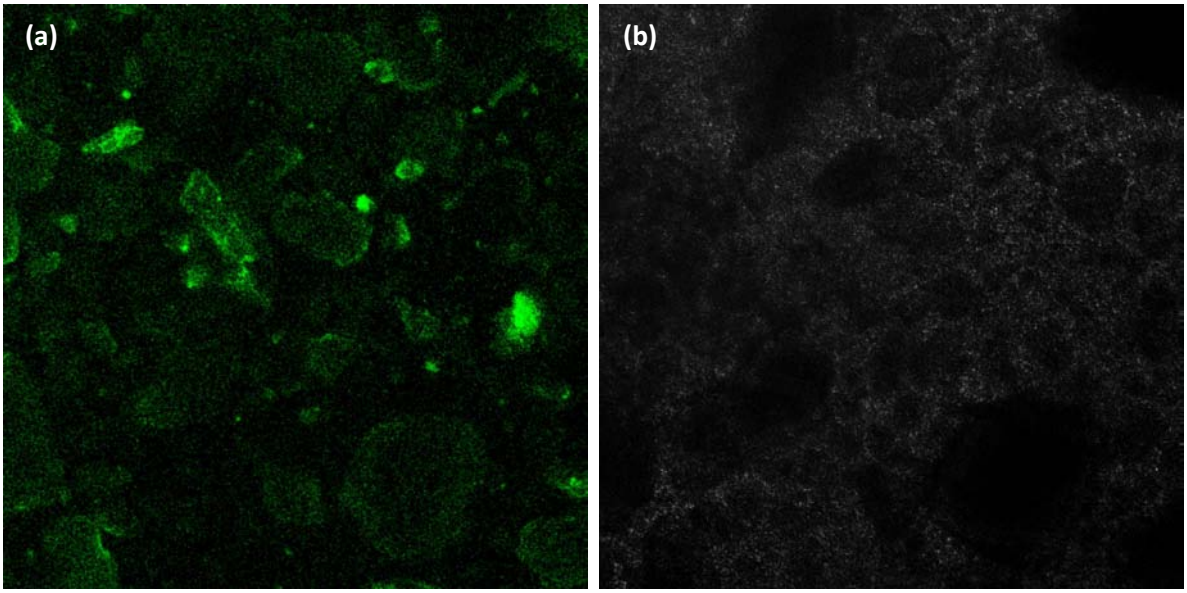

Figure 5-12 Surface activity test for BSL-7mer with pre-bound HA nanoparticles. (a). The Fluor 488 image of HA particles after incubating with BSL-7mer followed by biotinylated BSL-spacer; (b).The phase contrast of HA particles after incubating with BSL-7mer followed by biotinylated BSL-spacer.

5.4 Conclusions

A HA-binding peptide sequence (MLPHHGA) attached to the terminus of the BSL protein exhibited high-specific binding to crystalline hydroxyapatite and was able to direct the mineralization process of calcium and phosphate to produce OCP, a precursor of the HA in bone and tooth growth (or HA, depending on solution conditions [196, 212]. Moreover, fluorescence labeling studies showed that the surface-active amphiphilic β-sheet domain and the biomineralzation domain in these proteins were able to act independently. Together, these results suggest that the hybrid peptide BSL-7mer may be suitable as a biomineralization substrate. BSL-7mer, on one hand, has ability to form well-defined two-dimensional surface layers (or even three dimensional fibrils [69]), which makes this hybrid

peptide an attractive candidate for biofunctionalization of scaffolding materials for bone tissue engineering. On the other hand, BSL-7mer has capacity to localize in bone tissue and direct the formation of calcium phosphate deposits. Combined with other genetically selected or designed HA-binding peptides, calcium phosphate biomineralization could be controlled and regulated using this designer protein platform. The findings of this work are promising initial steps toward the development of systems for fundamental studies of biomineralization and for practical applications in restoration and regeneration of the hard tissues such as bone, cartilage, and teeth [213]. In the future research, we will focus on investigating the effect of the minerals produced by the BSL-7mer on the activity of osteoblasts and formation of skeletal tissues. We will explore the utility of BSL-5mer and BSL-9mer as triggers of calcium phosphate mineralization on scaffold surfaces as well.

Chapter 6

Surface-Active Proteins with Silver-Binding Domains

6.1 Introduction

Metal nanoparticles have received considerable attention in recent years due to their unique properties and their enormous potential for applications in areas such as catalysis [214], biological labeling [215], (bio) chemical sensing and imaging [215,216], electronics [217], photonics[218], and drug delivery[219]. Silver nanoparticles (AgNPs) in particular have become one of the most widely studied metal nanoparticle types due to their distinctive properties, including broad-acting biocidal activity [220,221], electrical conductivity and chemical stability [217] and optical polarizability [218]. Indeed, AgNPs are routinely used to inhibit bacterial colonization and biofilm formation in many consumer materials. It is also impressive that AgNPs can be used to protect cells against HIV-1 infection and promote wound healing [220].

Physical and chemical methods to synthesize silver nanoparticles are well-established. These include the use of electromagnetic radiation [222, 223], gas condensation [224], thermal decomposition in organic solvents [225], chemical reduction with reducing agents like dimethylformamide (DMF) or with stabilizing and protective agents [221, 226]. In

recent years, efforts have focused on more environmentally friendly nanoparticle synthesis processes, including bio-inspired approaches. In particular, using biological organisms to produce inorganic nanoparticles, either intracellularly or extracellularly [227-229], has been increasingly utilized. A number of inorganic nanomaterials have been synthesized using a number of different microorganisms including bacteria [230], yeast [231], fungi [229,232] and algae [233]. The bacterium Pseudomonas stutzeri AG259, originally isolated from the soil of a silver mine[234], was found to reduce silver ions in aqueous solutions of $AgNO_3$ and to agglomerate them within the periplasmic space of the bacteria into silver nanoparticles of well-defined size and distinct morphology [230]. Bacillus licheniformis, on the other hand, was found to produce silver nanoparticles extracellularly by enzymatic reduction of nitrate reductases [228]. The fungus Verticillium was shown to intracellularly reduce silver ions and form silver nanoparticles probably due to the metal ion reduction of enzymes in the cell wall membrane [229]. Various fungi such as Penicillium fellutanum[232], Phoma sp. 3.2883[235], Aspergillus fumigates[236], Fusarium oxysporum[237] have also been reported for producing stable silver nanoparticles when silver nitrate was introduced to the aqueous medium. Some plant-derived systems, such as Azadirachta indica (Neem) leaves and the citrus limon aqueous extract, have also been used for the synthesis of silver nanoparticles [238,239].

Based on the hypothesis that the organic matrices implicated in biosynthesis of silver particles contain silver-binding peptides that act as nucleation sites, Stone *et al.* [33] identified silver-binding peptides using a phage-displayed peptide library, thereby bridging the divide between biological and biomimetic synthesis of silver nanoparticles. In this study,

the 12-mer peptides AG3 (AYSSGAPPMPPF) and AG4 (NPSSLFRYLPSD) were determined to be the predominant silver binding peptides due to their significantly high binding affinity for silver ions and capability to form silver nanoparticles.

As part of this thesis research, we utilized these established silver-binding peptides to create proteins capable of forming stable coatings on surfaces and subsequently nucleating the growth of AgNPs. The focus of these studies was a chimera (named BSL-Ag4) consisting of the AG4 silver-binding domain (NPSSLFRYLPSD) appended to the end terminus of the BSL-spacer protein. Detailed studies using UV-Vis, SEM, TEM and EDS demonstrated that the recombinant protein was able to accumulate and reduce the silver ions to synthesize silver nanoparticles on surfaces functionalized by self-assembly of BSL-Ag4. The ability to control surface composition and density of these coatings (e.g. though the use of mixtures of BSL-Ag4 and other BSL variants) provides the possibility to tailor the formation and distribution of silver nanoparticles on surfaces. This investigation was motivated in part by potential applications for anti-microbial biomaterial surfaces.

6.2 Materials and Methods

6.2.1 Materials and Reagents

The putative AgNP-binding protein was designed and synthesized as described earlier in Chapter 2. $AgNO_3$ was purchased from Sigma-Aldrich. All other chemicals were purchased either from Sigma-Aldrich (Oakville, ON, Canada) or Fisher Scientific (Ottawa, ON, Canada).

6.2.2 Synthesis of AgNPs on BSL-Ag4 Templates

AgNPs were produced in aqueous solution by reduction of silver nitrate in the presence of the BSL-Ag4 protein. To do so, 600 μl freshly prepared BSL-Ag4 (100 μM) (or BSL-spacer as a control) were mixed at room temperature with 50 μl of a 20 mM aqueous solution of silver nitrate at pH 7.5 and stirred for 10 min. The samples were then placed in a dark environment for 48 h at room temperature to allow the AgNP formation to occur. The AgNP content of the resulting solutions was then initially characterized using a Cary100 UV-vis spectrophotometer (Varian Medical Systems, Inc., Palo Alto, USA) to monitor the size-dependent surface plasmon resonance absorption peak around 400-440 nm [240].

6.2.3 Electron Microscopy Studies of BSL-Ag4 induced AgNPs

Transmission electron microscopy was performed to examine the silver-binding affinity of BSL-Ag4 after it was immobilized onto the surface by self-assembly of its amphiphilic β-sheet domains. To do so, 25 μM of BSL-Ag4 (or BSL-spacer as a control) were coated by passive adsorption onto Au grids for 24 h. Grids were then rinsed three times with dH_2O to remove excess unbound protein. Subsequently, 2 mM silver nitrate solution was added to cover the surface of protein-coated Au grids and kept in a dark environment for 24 h at room temperature. The grids were then rinsed gently with dH_2O and dried before TEM characterization. Similar samples were also prepared with BSL-Ag4 peptide-coated PS surfaces (instead of Au grids) and incubated in aqueous silver nitrate solutions for 48 h for subsequent imaging with SEM and quantitative composition analysis with EDS, as described previously.

6.3 Results and Discussion

6.3.1 Synthesis, Expression and Purification of the BSL-Ag4 Protein

The Ag4 silver-binding domain (NPSSLFRYLPSD) was appended to the end of the BSL-spacer gene to create a BSL protein variant with acquired antimicrobial activity from the formation of silver nanoparticles at the terminus. This protein would produce surface-tethered silver nanoparticles in situ by reducing and binding silver to the termini of proteins previously adsorbed onto surfaces via their amphiphilic β-sheet domains. Such a protein could be used as a component of novel biomedical scaffold materials. To achieve the goal, the vector PET-21d+ containing BSL-Ag4 gene was constructed using the fragment-vector enzymatic ligation technique, identified with colonies PCR, and then verified by DNA Sequencing in the OHRI Stemcore laboratories DNA sequencing Facility, as previously described.

BSL-Ag4 protein was expressed and purified using the methods described in Chapter 2. Inclusion body purification was first performed, followed by gel filtration purification using Fast protein liquid chromatography (FPLC) with Sephadex^{TM} G-50 Fine media. A representative FPLC gel filtration purification trace is shown in Figure 6-1a. The gel filtration method separates protein according to size, with the largest molecules eluting first (the A1 fraction in this case). The fractions A1-A10, B8-B5 collected from FPLC were visualized with SDS-PAGE (Figure 6-1b). The eluted fractions from A7 to B5 primarily

were found form the SDS-PAGE results to contain single bands near 8 kDa. Hence, these protein fractions were collected and then lyophilized. Figure 6-2 provides a summary of SDS-PAGE results for protein BSL-Ag4 at different stages of expression and purification. This figure shows that good expression (as indicated by the difference between pre-induction and post-induction bands) and high level of purity (greater than 90%) using the FPLC gel filtration method was obtained for BSL-Ag4.

The molar mass of protein BSL-Ag4 was verified using Matrix-assisted laser desorption mass spectrometry (MALDI). The MALDI results for BSL-Ag4 shown in Figure 6-3 indicate a dominant peak at approximately10213 Da, with a deviation of 0.1% from the theoretical value of 10202 Da.

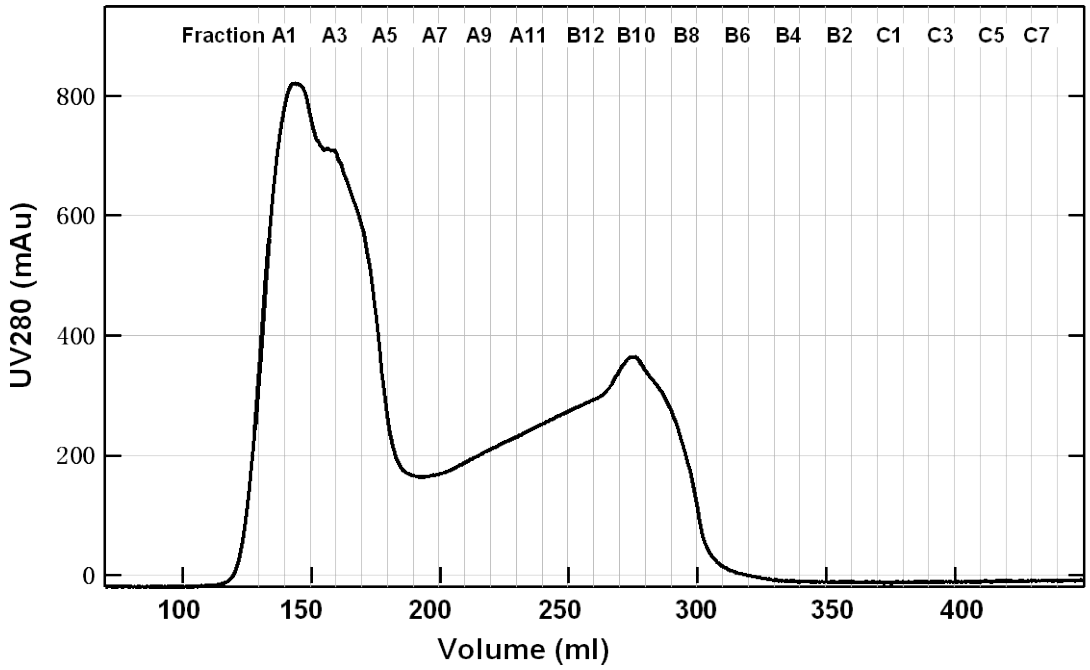

Figure 6-1a A representative purification trace of BSL-Ag4 using Gel-filtration with FPLC. The fractions A1-A10, B8-B5 were visualized with SDS-PAGE.

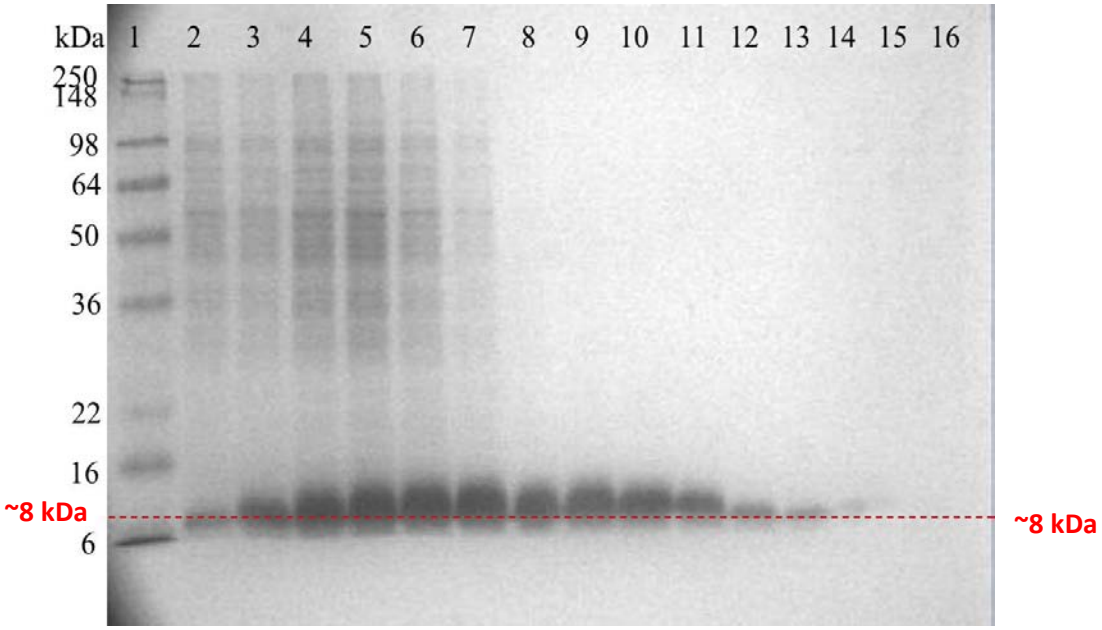

Figure 6-1b A representative coomassie stained SDS-PAGE gel to show the purification of BSL-Ag4 with Gel-filtration. Lane1: SeeBlue Plus 2 standard. Lane2-15: fractions A1-A10, B8-B5 from FPLC gel filtration purification of BSL-Ag4.

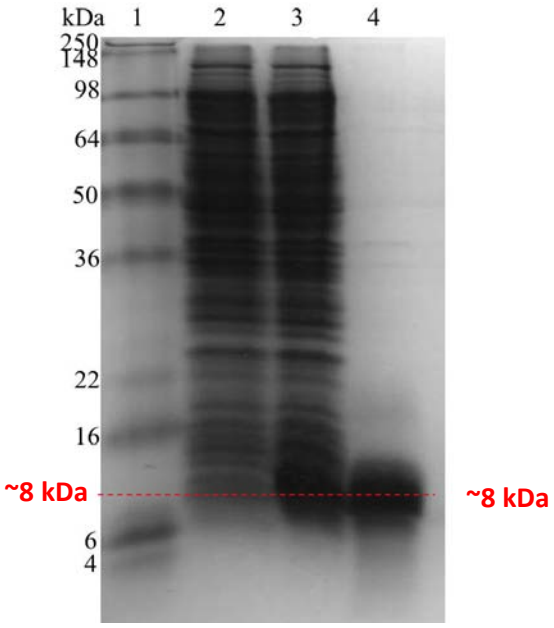

Figure 6-2 A coomassie stained SDS-PAGE gel to show the expression and purification of BSL-Ag4. The lanes contain the following: Lane1: SeeBlue Plus 2 standard. Lane2: BSL-Ag4 pre-induction. Lane 3: BSL-Ag4 4h post-induction. Lane 4: purified BSL-Ag4.

BSL- Ag4:

M D Y E I K F H G D G D N F D L N L D D S G G D L Q L Q I R G P G G R V Q V H I H S S S G K V D F H V N N D G G D V E V K M H P W *G S T S G S G K P G S G E G S T K G* *T* **N P S S L F R Y L P S D**

Length=96aa MW=10203Da PI=5.07

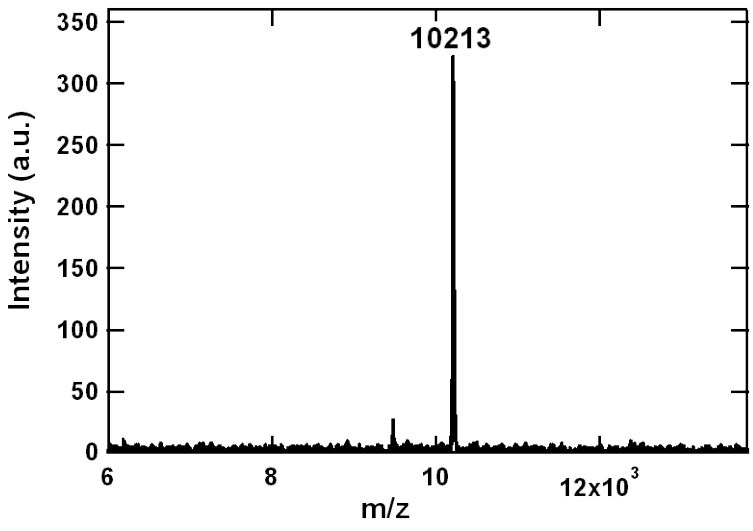

Figure 6-3 Sequence and MALDI spectrograph of BSL-Ag4 with significant peak at 10213.

6.3.2 Monitoring Production of Silver Nanoparticles with UV-Vis

The AG4 peptide binds silver ions from aqueous silver nitrate solution and nucleates formation of silver nanoparticles. Stone *et al.* [241] proposed a model for peptide-induced silver-crystal formation based on the hypothesis that interactions between silver-binding peptides and silver nanoclusters in the aqueous silver nitrate solution create a chemically reducing environment around these clusters, which in turn accelerated the reduction of silver ions at the interface between silver-binding peptides and metal clusters. As shown in Figure 6-4, when silver-binding peptides are added to the aqueous silver nitrate solution, silver-binding peptides start to reduce silver ions, induce silver nucleation, and form silver nanoclusters in the solution (step 1). As silver-binding peptides continually reduce silver ions around silver clusters, a chemically reducing environment is created (step 2), thus accelerating the reduction of silver ions at the interface between silver-binding peptides and silver clusters. Ultimately silver crystals with various distinct particle morphologies, such as triangles and hexagons, are formed in the solution (step 3).

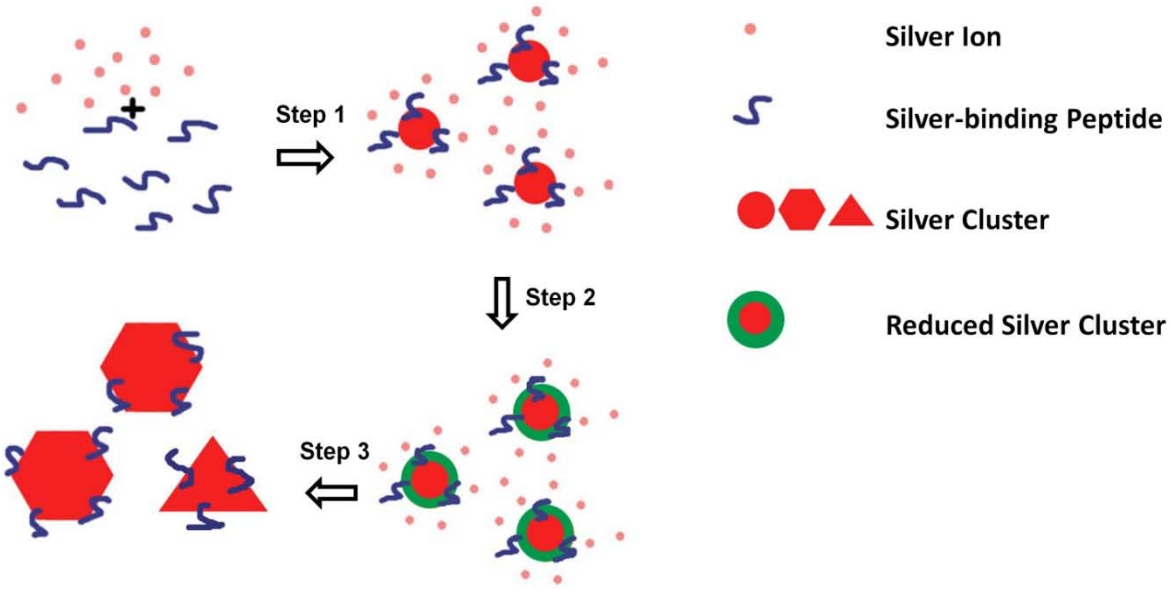

Figure 6-4 Proposed pathway for the formation of silver crystals with silver-binding peptides.

Since silver nanoparticles exhibit a size-dependent surface plasmon resonance absorption peak around 400-440 nm [240] which can be characterized using UV-Vis spectroscopy, we can in turn study the formation of silver nanoparticles by monitoring UV-Vis spectroscopy when silver nitrate solution is incubated with the silver-binding peptides. The shift in UV-Vis spectra with time is an indication of nucleation and growth of silver nanoparticles in solution. To examine the capability of BSL-Ag4 peptide to induce AgNP formation, aqueous solutions of 100 µM BSL proteins (BSL-Ag4 or BSL-spacer, as a control) and 20 mM silver nitrate were incubated for a period of 48 h at room temperature. The UV-Vis spectral response as a function of time of the silver nanoparticles induced by BSL-Ag4 is shown in Figure 6-5. The spectrum for the reaction with BSL-Ag4 peptide and silver nitrate solution was measured when they were initially mixed together and after 48 h of incubation at room temperature. For comparison, the UV-Vis spectrum using BSL-spacer

as a control reaction was also measured when initially mixed and after 48 h of incubation in silver nitrate solution.

There is no indication from UV-Vis absorption of AgNPs immediately after mixing of silver nitrate with BSL-Ag4 or BSL-spacer solutions. Moreover, after incubating for a period of 48 h, the UV-Vis spectrum for the reaction containing BSL-spacer peptide still showed no significant absorption band near 440 nm; however, the reaction containing BSL-Ag4 peptide exhibited a distinct but broad absorption band around 440 nm. The breadth of the absorption band at longer wavelengths is presumably due to the size and shape distribution of silver nanoparticles [242]. These UV-Vis results conclusively demonstrated that BSL-Ag4 peptide is capable of reducing silver ions from aqueous solutions and forming silver nanoparticles without the addition of any external reducing agents. In contrast, the BSL-spacer control, without the silver binding domain, was found to have no capability of reducing silver ions from a solution of silver nitrate.

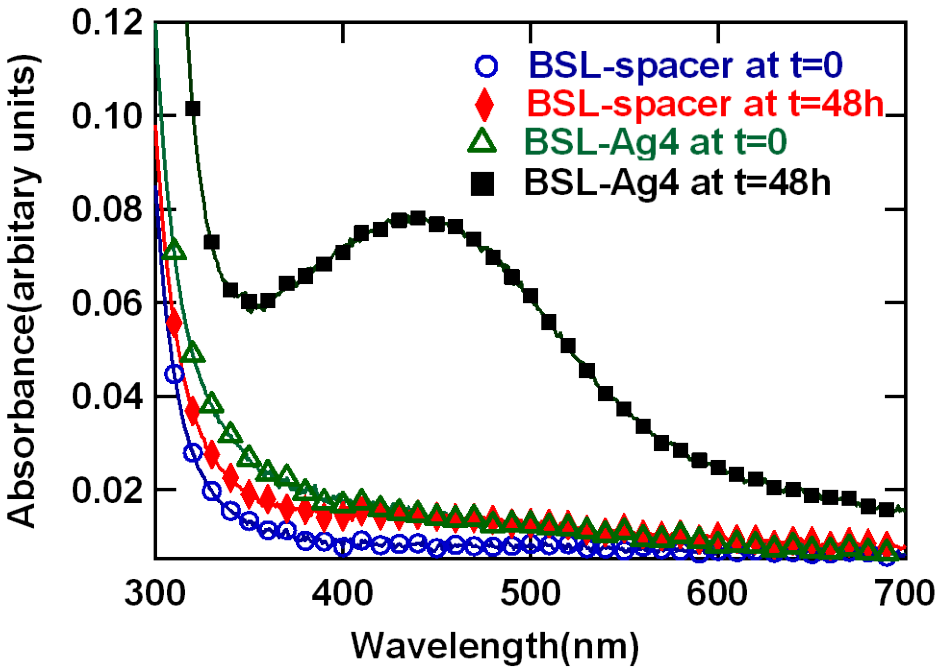

Figure 6-5 The UV-Vis spectral response of silver nitrate solutions in the presence of BSL proteins. For the case of BSL-Ag4, the presence of silver nanoparticles after 48 h is indicated by the absorption band at around 440 nm, whereas the presence of the control BSL-spacer did not lead to silver nanoparticles formation.

6.3.3 Silver Nanoparticle Formation on BSL-Ag4 Coated Surfaces

Electron microscopy was used to characterize the silver-binding ability of BSL-Ag4 peptide after it was immobilized onto surfaces by passive adsorption and the sizes and shapes of silver nanoparticles induced by the BSL-Ag4 peptide. An SEM experiment was first carried out to examine the formation process of silver nanoparticles in the presence of surface-bound BSL-Ag4 peptide. In the experiment, either BSL-Ag4 or BSL-spacer peptide was first immobilized onto the PS surface by passive adsorption of the amphiphilic β-sheet domains, as previously discussed. After subsequent exposure of silver nitrate solution for

48 h, the surfaces were prepared for SEM measurements by gently rinsing and drying the surfaces as previously described. Figure 6-6 shows representative SEM images of the samples. For the case of the BSL-spacer control protein (Figure 6-6a), there is no significant evidence of silver nanoparticles on the surface. A few small dots have square shapes probably due to the silver nitrate salts dried on the polystyrene surface. However, the PS surfaces coated with BSL-Ag4 protein have numerous faceted silver nanoparticles of different shapes and sizes (Figure 6-6b,c). The relatively smaller silver particles were observed using TEM, which is discussed later. These results confirmed that the silver-binding domain AG4 peptide was still functional after it was ligated to BSL-spacer and even after immobilization of BSL-Ag4 onto PS surfaces. Thus, the dual functionality of the BSL-Ag4 protein design (the ability to induce silver nanoparticles and to self-assemble on hydrophobic surfaces) has been achieved. SEM images of the silver particles synthesized using BSL-Ag4 peptide also revealed various distinct particle morphologies, including circular discs, hexagons, rod-like shapes, triangles and other irregular shapes. Particularly, faulty twinned crystals which partially contributed to the large size and shape of the nanoparticles [243] was also observed, as shown in Figure 6-6c.

The samples prepared for SEM studies were also used to verify the composition of nanoparticles with Energy-dispersive X-ray spectroscopy (EDS) [201]. A representative EDS spectral trace is shown in Figure 6-7. Grey lines in the figure indicate the positions of the characteristic X-ray lines of silver. Two significant silver peaks located at 3.34 keV and 3.51 keV were observed, and no visible atomic impurities were shown in the EDS

measurements. Thus, the EDS measurements confirmed that nanoparticles obtained with BSL-Ag4 were very pure silver.

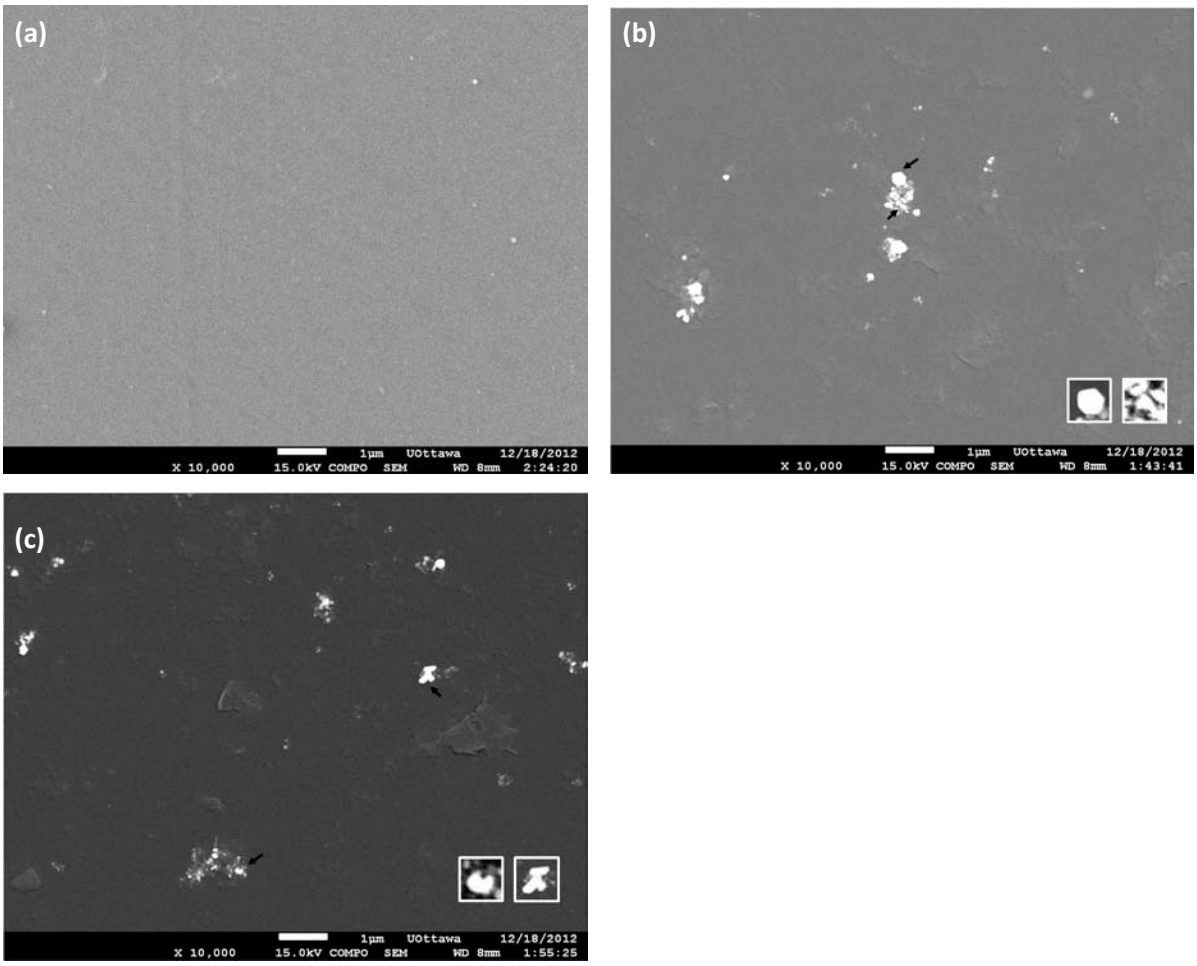

Figure 6-6 (a) A representative SEM image of negative control with BSL-spacer; (b-c) Representative SEM images of silver nanocrystals produced with BSL-Ag4, including hexagonal, trianglular, and rod-like shaped particles.

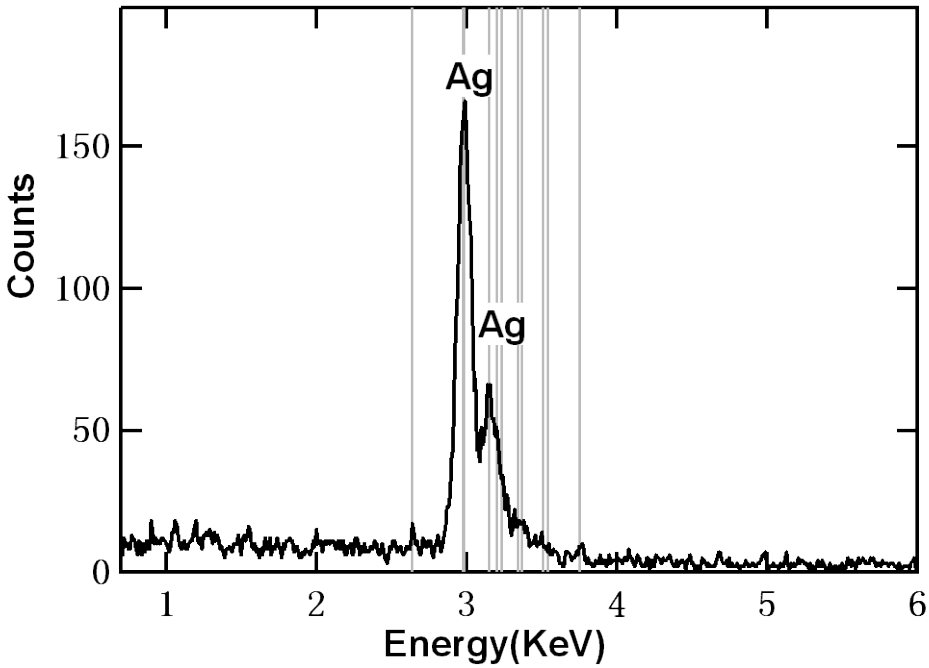

Figure 6-7 Representative EDS spectra for a nanoparticle obtained with BSL-Ag4 protein. Grey lines indicate the positions of the characteristic X-ray lines of silver.

The resolution limitations of the JSM-7599F SEM precluded the characterization of silver nanoparticles with size less than 50 nm. In order to characterize these smaller nanoparticles, additional studies were conducted using TEM. To do so, silver nanoparticles were produced on Au-grids by incubating a 2 mM silver nitrate solution with Au-grids that had been pre-coated with BSL-Ag4 or BSL-spacer peptides in dark environment for a period of 24 h. The silver nanocrystals formed on the surfaces were analyzed with TEM (Figure 6-8). For the case of the BSL-spacer control protein (Figure 6-8a), there were only a small number of very small silver nanoparticles found on the TEM grids; while there were numerous nanoparticles associated with the TEM grids coated with BSL-Ag4 (Figure 6-8b-d). As with the larger particles in the previous SEM studies, small circular, hexagonal, and triangular silver nanoparticles were observed for BSL-Ag4 coated grids. The size

distribution of these silver nanoparticles was obtained from a collection 266 distinct particles in the images by measuring the diameters of circles, the longest edges of the triangles, and length of rods, etc. This analysis yielded a mean size of 20±8 nm. Approximately 68% of the silver nanoparticles were in the size range of 10-25 nm that is particularly suitable for biomedical uses.

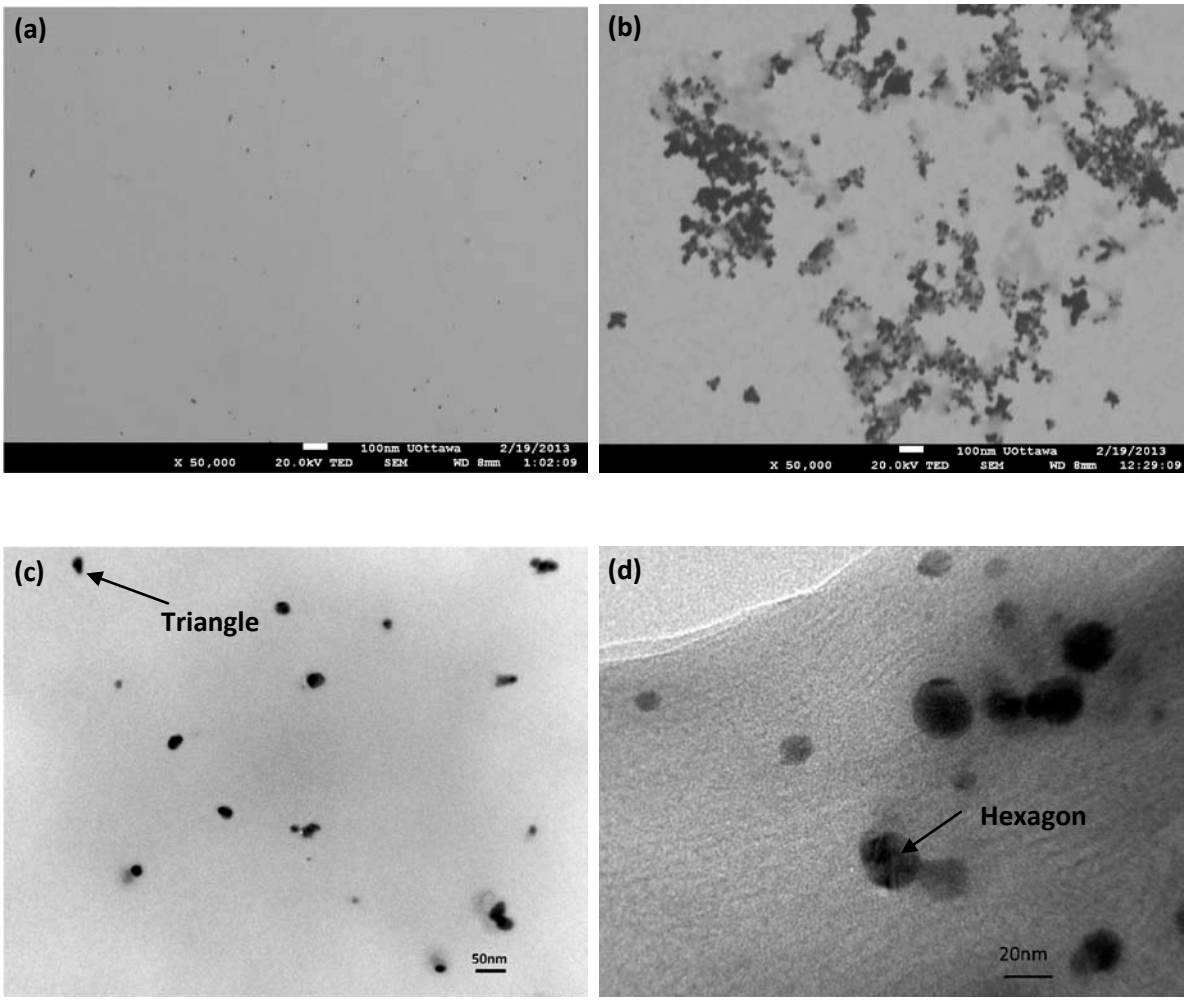

Figure 6-8 (a) Representative TEM image of negative control with BSL-spacer; (b-d) Representative TEM images of silver nanocrystals (hexagons, triangles, discs, and rods) produced with BSL-Ag4.

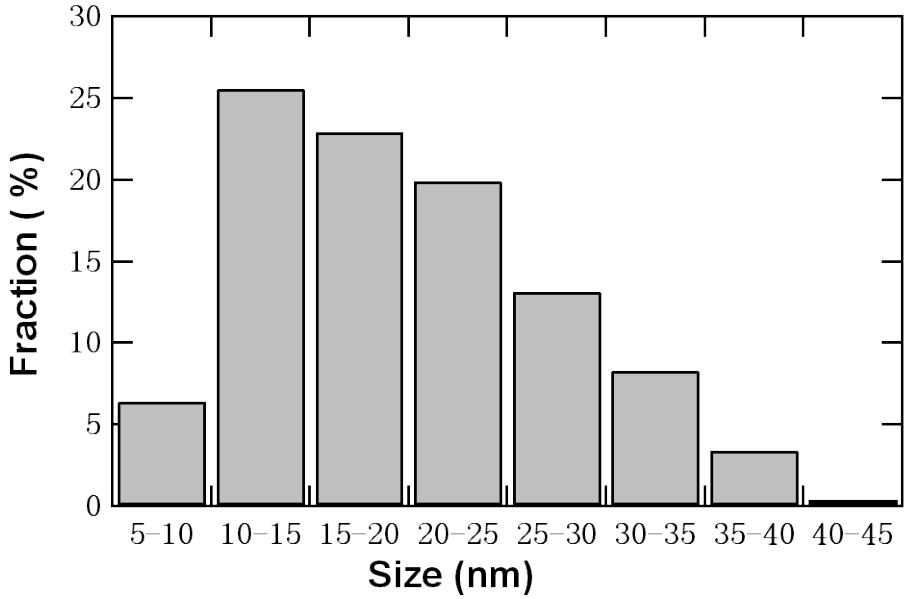

Figure 6-9 Particle size distribution for silver nanocrystals produced with BSL-Ag4.

6.4 Conclusions

A one-step synthesis method for protein-stabilized silver nanoparticles based on the bioreduction ability of BSL-Ag4 peptide under ambient conditions has been developed and validated. Using the well-known UV-Vis absorption characteristics of silver nanoparticles, the ability of the silver-binding domain in the BSL-Ag4 protein was shown to act as a reducing agent for silver ions in aqueous solution and to nucleate the subsequent formation of silver nanoparticles without addition of any external surfactants, protecting or linking agents. By characterization with TEM, SEM and EDS, it was also shown that immobilization of the BSL-Ag4 protein on surfaces did not inhibit the production of silver nanoparticles.

Since many applications of metal nanoparticles require their assembly on surfaces, this surface functionalization ability of BSL-Ag4 provides the possibility to build templates for deposition of inorganic silver nanoparticles. For instance, there is potential to spatially control the deposition of silver crystals into patterned arrays by spatially controlling the deposition of the BSL-Ag4 protein (e.g by using a materials printer). Such a facile means to functionalize surfaces with well-defined and controllable inorganic silver crystals may have utility in areas of biology, chemistry, engineering, and medicine. For example, as silver nanoparticles have innate antimicrobial properties, their templated patterning on surfaces would have numerous health care applications that are currently being explored in the group. Bio-synthesis of other metal nanoparticles such as gold, platinum and palladium based on BSL proteins is promising future work as well.

Chapter 7

Conclusions

Protein-based biomaterials have significant potential for fabrication of new scaffolds with properties that can be easily customized for particular tissue engineering applications. By combining multiple functional domains, such biomaterials are able to simultaneously induce various functions, such as improving cellular adhesion and response, generating antimicrobial attributes, and forming mineral deposits that may in turn generate a cell response. Since protein-based biomaterials are synthesized from monomeric building blocks, their structures and functions are controllable to suit for specific tissue engineering applications through appropriate genetic modular designs.

This thesis described the development of a library of de novo β-sheet-based diblock proteins for functionalizing scaffold interfaces using recombinant DNA methods. A variety of methodologies and techniques were involved in characterizing their structures and compositions and assessing their functional behaviors. Achievements within this thesis can be summarized as follows.

Diblock proteins, composed of a surface-active, amphiphilic block joined to a disordered, water-soluble block with an end terminal functional domain, were designed, cloned, expressed and purified. The proteins BSS-RGDS, BSS-YIGSR, BSL-RGDS and BSL-YIGSR were developed for generating and controlling cellular response to scaffold

surfaces. Additionally, the proteins BSL-5mer, BSL-7mer and BSL-9mer were developed for calcium phosphate mineralization on scaffold surfaces, and the protein BSL-Ag4 was developed for inducing silver nanoparticles and imparting antimicrobial properties on scaffold surfaces.

The primary structures of the proteins were confirmed using MALDI-TOF mass spectroscopy and amino acid composition analysis. By analyzing their secondary structures and thermal properties using CD, DSC and FTIR, it was demonstrated that the diblock proteins are composed of β-sheet, β-turn, and disordered coil secondary structures under moderate temperature and pH conditions, and that there is a well defined thermal transition between β-sheet and disordered coil structure in the amphiphilic block with increasing temperature. The insertion of bioactive domains, such as RGDS, YIGSR, at the terminus of the disordered coil module did not significantly affect the secondary structures of the proteins. This suggested that the various functional domains, including the cell binding, silver-binding, and hydroxyapaptite-binding domains, can be incorporated to the diblock proteins for the development of new attributes and applications without affecting the function of the associating β-sheet domain.

By studying the adsorption of proteins onto the hydrophobic substrates with the SPR technique and ^{125}I radio-labeling methods, it was demonstrated that the presentation of the bioactive domains has minimal impact on the surface adsorption of the proteins. The cell response to RGDS-functionalized scaffold surfaces was characterized using two adhesion-dependent cell lines, HFFs and C2C12s. Microscopy studies showed that cells remained round and un-attached on the surfaces coated with bioneutral BSL-spacer protein; while cells

strongly adhered and spread on the surfaces coated with the bioactive BSL-RGDS protein. Results from the microscopy and cell proliferation assays also showed that the cell response to the protein coated surfaces could be titrated and controlled by tuning the ratio of the bioneutral BSL-spacer (which inhibits cell adhesion) and the bioactive BSL-RGDS in solution, providing a facile means of tailoring bioactivity of a surface. Thus, a well-controlled method has been developed and verified for surface biofunctionalization based on the results that: (1) these diblock proteins self-assemble into stable, surface-active coatings on synthetic polymer materials; (2) the bio-active ligands distributed on the surfaces can be adjusted by the composition of coating solutions. This study focused on a single bioactive domain, RGDS; however, the method for surface biofunctionalization should be applicable to diblock protein variants with many other bioactive ECM peptide sequences. Different types of the bioactive ECM peptides could be introduced to substrate surfaces with optimized ratios to regulate the behavior of a wide range of cell types and cell culture applications.

Hydroxyapatite-binding domains were also fused to the terminus of the diblock proteins to produce biofunctional materials for bone regeneration. The binding affinity of the BSL-7mer for hydroxyapaptite was first quantitatively estimated by monitoring the concentration changes of the protein during the incubation with hydroxyapatite nanoparticles. The results indicated that as much as 60% of the protein was bound to the hydroxyapaptite after incubation for 24 h. Additional studies with SEM showed that BSL-7mer exhibited significant binding affinity for hydroxyapatite nanoparticles even after it was immobilized onto PS surfaces. It is also shown in TEM and EDS studies that the BSL-7mer is able to

direct the mineralization process of calcium and phosphate to produce OCP, a precursor of hydroxyapatite, in a dilute aqueous solution of Ca^{2+} and PO_4^{3-}. The resulting OCP materials had the morphology of large plate-like crystals with dimensions of several hundred nanometers in width and length. Moreover, studies with fluorescently stained biotinylated BSL-spacer and BSL-7mer (with Alexa Fluor 488 streptavidin) showed that the surface-active amphiphilic β-sheet domain and the biomineralization domain in the proteins were able to act independently. Therefore, BSL-7mer may be suitable as a biomineralization substrate since it is able to form well-defined two-dimensional surface layers by surface-adsorption of the β-sheet domain that are capable of subsequent mineralization by the displayed 7mer binding domain.

To develop a diblock variant with potential biocidal activity, the protein BSL-Ag4 with the Ag4 silver-binding domain attached to the terminus of the soluble random coil block was created and studied. Through UV-Vis spectroscopy, TEM and SEM studies, the silver-binding domain in the BSL-Ag4 protein was shown to be capable of reduction of silver ions in a silver nitrate aqueous solution, and subsequent nucleation and formation of silver nanoparticles without addition of any external surfactants, protecting or linking agents. The corresponding EDS spectra exhibited several distinct peaks for metallic silver, which confirmed that the nanoparticles obtained with the BSL-Ag4 are composed of essentially pure silver. Analysis of the size distribution of the silver nanoparticles obtained from a collection of 266 distinct particle images yielded a mean size of 20.0 nm. Approximately 68% of the silver nanoparticles was in the size range of 10-25 nm that is particularly suitable for biomedical uses. The surface functionalization ability of the BSL-Ag4 also provides the

possibility to precisely control the distribution of silver nanoparticles on a scaffold surface. Such silver nanoparticles on surfaces may be used for imparting innate antibacterial properties to various biomedical materials.

The results described in this thesis clearly demonstrate the potential of the amphiphilic diblock protein motif as an effective means of surface functionalization of biomaterials for tissue engineering and other biomedical applications. In the specific examples explored by the present work, we were able to improve cell adhesion and spreading in the presence of the RGDS ligands, induce calcium phosphate mineralization with the addition of the HA-binding domains, and form silver nanoparticles with insertion of the silver-binding domain. With the inherent surface self-assembly attribute of this diblock protein motif, a variety of biological functionalities may easily be imparted to otherwise bio-inert scaffold surfaces simply by incorporating an appropriate active sequence at the free terminus of the soluble block.

Given the potential applications of these diblock proteins in tissue engineering and biomedicine, several areas are worthy of future research. After demonstrating the capacity of the BSL-7mer to induce calcium phosphate mineralization, the lab will next focus on the investigation of the effect of the mineralized surfaces on the activity of osteoblasts and formation of skeletal tissues, and on the potential of directing stem cell differentiation to osteoblasts. The other two types of surface-active proteins with HA-binding domains (BSL-5mer and BSL-9mer) will also be studied as triggers of calcium phosphate mineralization on scaffold surfaces, as discussed in chapter 5. Another promising study is related to the antimicrobial activity of silver nanoparticles produced by BSL-Ag4. Since the use of silver

nanoparticles as an antimicrobial agent has rapidly increased, evaluation of the efficacy of surface-associated silver nanoparticles against different microorganisms will be investigated for several representative bacteria of interest. It will also be very interesting to expand the number of diblock variants to include a broad range of terminal functional domains and to combine various functional domains (such as bioactive ligands and HA-binding domains) for particular cell types and cell culture applications. In this scenario, the possibility of synergistic activities between various functional domains is particularly interesting. Finally, there is potential to directly use diblock proteins as scaffolds for tissue engineering, since they are in fact able to self-assemble to hydrogels in certain conditions. Although the results for the hydrogel formation with these diblock proteins were not discussed in this thesis, the methods to form hydrogels with the proteins have been developed and the characterization studies are currently being conducted.

References

[1] Barnes S.J. and Harris L.P., *Tissue engineering: roles, materials and applications*, Nova Science Publishers, New York, 2008.

[2] Wolfe R.A., Roys E.C. and Merion R.M. (2010), Trends in organ donation and transplantation in the United States 1999-2008, *Am. J. Transplant.* , 10, 4, 961-972.

[3] CIHI's Canadian Organ Replacement Register (CORR) (2013), Canadian Organ Replacement Register Annual Report: Treatment of End-Stage Organ Failure in Canada, 2002 to 2011, https://secure.cihi.ca/estore/productFamily.htm?locale=en&pf=PFC2053

[4] Scientific Registry of Transplant Recipients (SRTR) (2012), Table 1.1 U.S. Organ donors by organ and donor typer, 2002 to 2011; Table 1.3 Waiting list at end of year, 2002 to 2011, http://www.srtr.org/annual_Reports/2011/

[5] Chapekar M.S. (2000), Tissue engineering: challenges and opportunities, *J. Biomech. Mater. Res. (Appl. Biomater.)*, 53, 617-620.

[6] Liao S., Chan C.K. and Ramakrishna S. (2008), Stem cells and biomimetic materials strategies for tissue engineering, *Mater. Sci. Eng. C*, 28, 8, 1189-1202

[7] Binderman I., Yaffe A., Zohar R., Benayahu D. and Bahar H. (2011), Tissue engineering of bone: an ectopic rat model, *Front. Biosci. (Schol. ed.)*, 3, 61-68.

[8] O'Brien F.J. (2011), Biomaterials and scaffolds for tissue engineering, *Materialstoday*, 14, 3, 88-95.

[9] Bergmann C.P. and Stumpf A., *Dental ceramics: Microstructure, properties and degradation*, Springer-Verlag, Berlin, Heidelberg, 2013

[10] Rezwan K., Chen Q.Z., Blaker J.J. and Boccaccini A.R. (2006), Biodegradable and bioactive porous polymer/inorganic composite scaffolds for bone tissue engineering, *Biomater.*, 27, 18, 3413-3431.

[11] Cheung H.Y., Lau K.T., Lu T.P.and Hui D. (2007), A critical review on polymer-based bio-engineered materials for scaffold development, *Composites B*, 38, 291-300

[12] Lee K.Y. and Mooney D.J.(2001), Hydrogels for tissue engineering, *Chem. Rev.*, 101, 7, 1869-1880.

[13] Ratner B.D., Hoffman A.S., Schoen F.J. and Lemons J.E., *Biomaterials science: An introduction to materials in medicine, 3rd ed.,* Academic Press, Oxford, 2013

[14] Kazemzadeh-Narbat M., Kindrachuk J., Duan K., Jenssen H., Hancock R.E. and Wang R. (2010), Antimicrobial peptides on calcium phosphate-coated titanium for the prevention of implant-associated infections, *Biomater.,* 31, 36, 9519-9526

[15] Yildirim E.D., Gandhi M., Fridman A., Güçeri S. and Sun W. (2008), Plasma surface modification of three dimensional poly (ε-Caprolactone) scaffolds for tissue engineering application, In *Plasma Assisted Decontamination of Biological and Chemical Agents*, *NATO Sci. Peace Security A*, 191-201.

[16] Major R. (2013), Self-assembling surfaces of blood-contacting materials, *J. Mater. Sci.: Mater. Med*., 24, 3, 725-733

[17] Hajicharalambous C.S., Lichter J., Hix W.T., Swierczewska M., Rubner M.F. and Rajagopalan R. (2009), Nano- and sub-micron porous polyelectrolyte multilayer assemblies: Biomimetic surfaces for human corneal epithelial cells, *Biomater.*, 30, 23-24, 4029-4036

[18] Puleo D.A. and Nanci, A. (1999), Understanding and controlling the bone-implant interface, *Biomater*., 20, 2311-2321.

[19] Brétagnol F., Lejeune M., Papadopoulou-Bouraoui A., Hasiwa M., Rauscher H., Ceccone G., Colpo P. and Rossi F. (2006), Fouling and non-fouling surfaces produced by plasma polymerization of ethylene oxide monomer, *Acta Biomater.*, 2, 2, 165-172.

[20] Ratner, B.D. and Bryant S.J. (2004), Biomaterials: Where we have been and where we are going, *Annual Rev. Biomed. Eng*., 6, 41-75.

[21] Hoffman A.S. (1999), Non-fouling surface technologies, *J. Biomater, Poly. ed.,* 10, 10, 1011-1014.

[22] Frederix F., Bonroy K., Reekmans G., Laureyn W., Campitelli A., Abramov M.A., Dehaen W. and Maes G. (2004), Reduced nonspecific adsorption on covalently immobilized

protein surfaces using poly (ethylene oxide) containing blocking agents, *J. Biochem. Biophys. Methods*, 58, 67–74

[23] Kingshott P. and Griesser H.J. (1999), Surfaces that resist bioadhesion, *Curr. Opin. Solid State Mater. Sci.*, 4, 403– 412.

[24] Prime K.L. and Whitesides G.M. (1991), Self-assembled organic monolayers-model systems for studying adsorption of proteins at surfaces. *Science*, 252, 1164– 1167.

[25] Ishihara K., Ziats N.P., Tierney B.P., Nakabayashi N. and Anderson J.M.(1991). Protein adsorption from human plasma is reduced on phospholipid polymers, *J. Biomed. Mater. Res.* , 25, 1397-1407

[26] Holland N.B., Qiu Y., Ruegsegger M. and Marchant R.E. (1998), Biomimetic engineering of non-adhesive glycocalyx-like surfaces using oligosaccharide surfactant polymers, *Nature*, 392, 799-801

[27] Zourob M., *Recognition receptors in biosensors*, Springer, New York, 2010.

[28] Shin H., Jo S. and Mikos A.G. (2003), Biomimetic materials for tissue engineering, *Biomater*., 24, 24, 4353-4364.

[29] Brown E. and Dejana E. (2003), Cell-to-cell contact and extracellular matrix editorial overview: Cell-cell and cell-matrix interactions- running, jumping, standing still, *Curr. Opin. Cell Biol.*, 15, 5, 505-508.

[30] Fischer S.E., Liu X., Mao H.Q. and Harden J.L. (2007), Controlling cell adhesion to surfaces via associat.ing bioactive triblock proteins, *Biomaterials*, 28, 22, 3325-3337

[31] West J.L. and Hubbell J.A. (1999), Polymeric biomaterials with degradation sites for proteases involved in cell migration, *Macromol.*, 32, 241–244.

[32] Roy M.D., Stanley S.K., Amis E.J. and Becker M.L. (2008), Identification of a highly specific hydroxyapatite-binding peptide using phage display, *Advan. Mater.*, 20, 1830-1836.

[33] Naik R.R, Jones S.E., Murray C.J., McAuliffe J.C., Vaia R.A. and Stone M.O. (2004), Peptide templates for nanoparticle synthesis derived from polymerase chain reaction-driven phage display, *adv. Funct. Mater.*,14,1,25-30

[34] Langer R. and Tirrell D.A. (2004), Designing materials for biology and medicine, *Nature,* 428, 487-492.

[35] Gottlieb D., Morin S.A., Jin S. and Raines R.T. (2008), Self-assembled collagen-like peptide fibers as templates for metallic nanowires, *J. Mater. Chem.*, 1, 18, 3865-3870.

[36] Sengupta D. and Heilshorn S.C. (2010), Protein-engineered biomaterials: highly tunable tissue engineering scaffolds, *Tissue Eng. Part B Rev.* , 16, 3, 285-293.

[37] Woolfson D.N. (2010), Building fibrous biomaterials from α-helical and collagen-like coiled-coil peptides, *Biopolymers*, 94, 1, 118-127.

[38] Liu W., Merrett K., Griffith M., Fagerholm P., Dravida S., Heyne B., Scaiano J.C., Watsky M.A., Shinozaki N., Lagali N., Munger R. and Li F. (2008), Recombinant human collagen for tissue engineered corneal substitutes, *Biomater.*, 29, 9, 1147–1158.

[39] Fagerholm P., Lagali N.S., Merrett K., Jackson W.B., Munger R., Liu Y., Polarek J.W., Söderqvist M. and Griffith M. (2010), A biosynthetic slternative to human donor tissue for inducing corneal regeneration: 24-month follow-up of a phase 1 clinical study, *Sci. Transl. Med.*, 2, 46, 46-61.

[40] Zhu S., Qian L., Hong M., Zhang L., Pei Y. and Jiang Y. (2011), RGD-modified PEG-PAMAM-DOX conjugate: In vitro and in vivo targeting to both tumor neovascular dndothelial cells and tumor cells, *adv. Mater.*, 23, 12, H84–H89.

[41] Knowles T.P.J., Oppenheim T.W., Buell A.K., Chirgadze D.Y. and Welland M.E. (2010), Nanostructured films from hierarchical self-assembly of amyloidogenic proteins， *Nat. Nanotech.*,5, 204 - 207

[42] Dinca V. ,Kasotakis E. , Catherine J.,Mourka A.,Ranella A., Ovsianikov A. , Chichkov B.N,Farsari M.,Mitraki A. and Fotakis C. (2008), Directed Three-Dimensional Patterning of Self-Assembled Peptide Fibrils, *Nano Lett.*, 8, 2, 538–543

[43] Channon K. and MacPheeb C.E. (2008), Possibilities for ‘smart’ materials exploiting the self-assembly of polypeptides into fibrils,*Soft Matter,* 4, 647-652

[44] Zhang S., Marini D.M., Hwang W. and Santoso S. (2002), Design of nanostructured biological materials through self-assembly of peptides and proteins, *Curr Opin Chem Biol.*, 6, 6, 865-71

[45] Du C., Falini G., Fermani S., Abbott C. and Moradian-Oldak J. (2005), Supramolecular assembly of amelogenin nanospheres into birefringent microribbons, *Science,* 307, 1450–1454.

[46] Tanaka S., Kerfeld C.A., Sawaya M.R., Cai F., Heinhorst S., Cannon G.C. and Yeates T.O. (2008), Atomic-level models of the bacterial carboxysome shell, *Science,* 319, 1083–1086.

[47] Engelhardt H. (2007), Are S-layers exoskeletons? The basic function of protein surface layers revisited, *J. Struct. Biol.*, 160, 115–124.

[48] Liu J., Zheng Q., Deng Y.Q., Cheng C.S., Kallenbach N.R., Lu M. (2006), A seven-helix coiled coil, *Proc. Natl. Acad. Sci. U.S.A.*, 103, 15457–15462

[49] Grigoryan G. and Keating A.E. (2008), Structural specificity in coiled-coil interactions, *Curr. Opin. Struct. Biol.*, 18,4, 477–483

[50] Monica C. Branco M.C. and Schneider J.P. (2009), Self-assembling materials for therapeutic delivery, *Acta Biomater.*, 5, 3, 817–831

[51] Rajagopal K. and Schneider J.P. (2004), Self-assembling peptides and proteins for nanotechnological applications, *Curr Opin Struct Biol,* 14, 480–486.

[52] Arias F.J., Reboto V., Martín S., López I. and Rodríguez-Cabello J.C. (2006), Tailored recombinant elastin-like polymers for advanced biomedical and nano(bio)technological applications, *Biotechnol. Lett.,* 28, 10, 687-695.

[53] He G., Dahl T., Veis A. and George A. (2003) Nucleation of apatite crystals in vitro by self-assembled dentin matrix protein 1, *Nat Mater.* , 2,552–558.

[54] Gungormus M., Fong H., Kim I.W., Evans J.S., Tamerler C., Sarikaya M. (2008) Regulation of in vitro calcium phosphate mineralization by combinatorially selected hydroxyapatite-binding peptides, *Biomacromolecules,* 9, 966–973

[55] Koutsopoulos S., Unsworth L.D., Nagai Y. and Zhang S. (2009), Controlled release of functional proteins through designer self-assembling peptide nanofiber hydrogel scaffold, *Proc. Natl. Acad. Sci. U.S.A.*, 106, 12, 4623–4628

[56] Miller R.A., Presley A.D. and Francis M.B. (2007), Self-Assembling Light-Harvesting Systems from Synthetically Modified Tobacco Mosaic Virus Coat Proteins, *J. Am. Chem. Soc.,* 129, 11, 3104–3109

[57] Petka W.A., Harden J.L., McGrath K.P., Wirtz D. and Tirrell D.A. (1998) Reversible hydrogels from selfassembling artificial proteins, *Science,* 281, 389–392

[58] Mi L. , Fischer S. , Chung B. , Sundelacruz S., and Harden J.L. (2006), Self-Assembling Protein Hydrogels with Modular Integrin Binding Domains,*Biomacromolecules,* 7, 1, 38–47

[59] Fischer S.E., Mi L., Mao H.-Q., and Harden J.L. (2009), Biofunctional Coatings via Targeted Covalent Cross-Linking of Associating Triblock Proteins, *Biomacromolecules,* 10, 2408–2417

[60] Clark D.P. and Pazdernik N.J., *Molecular biology, 2nd Ed.*, Elsevier, Waltham, 2013.

[61] Branden C. and Tooze J., *Introduction to protein structure,* Garland Publishing, New York, 1991.

[62] Berg J.M., Tymoczko J.L. and Stryer L., *Biochemistry, 7th Ed.,* W.H. Freeman and Company, New York, 2012.

[63] Finkelstein A.V. and Ptitsyn O.B., *Protein physics: a course of lectures,* Academic Press, London, 2002

[64] Wu X. , Yang Z-Y., Li Y, Hogerkorp C-M., Schief W.R., Seaman M.S., Zhou T., Schmidt S.D., Wu L., Xu L., Longo N.S., McKeeK., O'Dell S. and Louder M.K. et al. (2010), Rational design of envelope identifies broadly neutralizing human monoclonal antibodies to HIV-1, *Science,* 329, 5993, 856-861

[65] Xiong H., Buckwalter B. L., Shieh H. M. and Hecht M. H. (1995), Periodicity of polar and nonpolar amino acids is the major determinant of secondary structure in self-assembling oligomeric peptides, *Proc. Natl. Acad. Sci. USA,* 92, 6349–6353

[66] Dahiyat B.I. and Mayo S.L. (1997), De novo protein design: Fully automated sequence selection, *science,* 278, 5335, 82-87

[67] Jäckel C., Kast P., Hilvert D. (2008), Protein design by directed evolution, *Annu. Rev. Biophys,* 37, 153-173

[68] Cordes M.H.J., Davidson A.R. and Sauer R. T. (1996), Sequence space, folding and protein design, *Curr. Opin. Struct. Biol.*, 6, 1, 3–10

[69] West M.W., Wang W., Patterson J., Mancias J., Beasley J. R. and Hecht M.H. (1999), De novo amyloid proteins from designed combinatorial libraries, *Proc. Natl. Acad. Sci. USA*, 96, 11211-11216.

[70] Xu G., Wang W., Groves J.T., and Hecht M.H. (2001), Self-assembled monolayers from a designed combinatorial library of de novo β-sheet proteins, *Proc. Natl. Acad. Sci. USA*, 98, 7, 3652-3657

[71] Brown C.L., Aksay I.A., Saville D.A and Hecht M.H. (2002), Template-directed assembly of a de novo designed protein, *J. Am. Chem. Soc.*, 124, 24, 6846-6848.

[72] Wang W. and Hecht M.H. (2002), Rationally designed mutations convert de novo amyloid-like fibrils into monomeric β-sheet proteins, *Proc. Natl. Acad. Sci. USA*, 99, 5, 2760–2765

[73] Whitlow M., Bell B.A., Feng S.L., Filpula D., Hardman K.D., Hubert S.L., Rollence M.L., Wood J.F., Schott M.E., Milenic D.E. Yokota T. and Schlom J. (1993), An improved linker for single-chain Fv with reduced aggregation and enhanced proteolytic stability, *Protein Eng.*, 6, 8, 989-995

[74] Pantoliano M.W. , Bird R.E. , Johnson S. , Asel E.D. , Dodd S.W., Wood J.F. and Hardman K.D. (1991), Conformational stability, folding, and ligand-binding affinity of single-chain Fv immunoglobulin fragments expressed in Escherichia coli, *Biochem.*, 30, 42, 10117-10125

[75] Van der Flier A. and Sonnenberg A. (2001), Function and interactions of integrins, *Cell Tissue Res*, 305, 3, 285-298.

[76] Givant-Horwitz, V., Davidson B. and Reich R. (2005), Laminin-induced signaling in tumor cells, *Cancer Letters*, 223, 1, 1-10.

[77] Kubota, Y., Kleinman, H. K., Martin, G. R., and Lawley, T. J. (1988), Role of laminin and basement membrane in the morphological differentiation of human endothelial cells into capillary-like structures, *J. Cell Biol.*, 707, 1589-1598.

[78] Sakamoto N., Iwahana M., Tanaka N.G. and Osada Y. (1991), Inhibition of angiogenesis and tumor growth by a synthetic laminin peptide, CDPGYIGSR-NH2, *Cancer Res*, 51, 903–906.

[79] Iwamoto Y., Robey F.A., Graf J., Sasaki M., Kleinman H.K., Yamada Y. and Martin G.R. (1987), YIGSR, a synthetic laminin pentapeptide, inhibits experimental metastasis formation, *Science*, 238, 1132–1134.

[80] Yoo S.Y., Kobayashi M., Lee P.P. and Lee S.W. (2011), Early osteogenic differentiation of mouse preosteoblasts induced by collagen-derived DGEA-peptide on nanofibrous phage tissue matrices, *Biomacromolecules*, 12, 4, 987–996

[81] Nomizu M., Weeks B.S., Weston C.A., Kim W.H., Kleinman H.K. and Yamada Y. (1995), Structure-activity study of a laminin α1 chain active peptide segment Ile- Lys-Val-Ala-Val (IKVAV), *FEBS Lett*, 365, 227-231

[82] Sarikaya M., Tamerler C., Jen A.K., Schulten K., and Baneyx F. (2003), Molecular biomimetics: nanotechnology through biology, *Nat Mater.* , 2, 9, 577-585.

[83] Whaley S.R., English D.S., Hu E.L., Barbara P.F. and Belcher A.M. (2000), Selection of peptides with semiconductor binding specificity for directed nanocrystal assembly. *Nature*, 405, 665-668.

[84] Gaskin D.J.H., Starck K. and Vulfson E.N. (2000), Identification of inorganic crystal-specific sequences using phage display combinatorial library of short peptides: A feasibility study, *Biotechnol. Lett.* , 22, 1211-1216.

[85] Ahmed S., Yang H., Ozcam A. E., Efimenko K., Weiger M. C., Genzer J. and Haugh J. M. (2011), Poly (vinylmethylsiloxane) elastomer networks as functional materials for cell adhesion and migration studies, *Biomacromolecules*, 12, 1265–1271.

[86] Lin Y.C., Brayfield C.A., Gerlach J.C., Rubin J.P. and Marra K.G. (2009), Peptide modification of polyethersulfone surfaces to improve adipose-derived stem cell adhesion, *Acta Biomater.*, 5, 5, 1416–1424.

[87] Jung H.J., Park K., Kim J.J., Lee J.H., Han K.O. and Han D.K. (2008), Effect of RGD-Immobilized Dual-Pore Poly (l-Lactic Acid) Scaffolds on Chondrocyte Proliferation and Extracellular Matrix Production, *Artif. Organs*, 32, 12, 981–989.

[88] Aucoin L., Griffith C.M., Pleizier G., Deslandes Y. and Sheardown H. (2002), Interactions of corneal epithelial cells and surfaces modified with cell adhesion peptide combinations, J. *Biomater. Sci., Polym. Ed.*, 13, 4, 447–462

[89] Zhang H and Hollister S. (2009), Comparison of bone marrow stromal cell behaviors on poly(caprolactone) with or without surface modification: Studies on cell adhesion, survival and proliferation , *J. Biomater. Sci., Polym. Ed.*, 20, 14, 1975–1993.

[90] Hirano Y., Okuno M., Hayashi T., Goto K. and Nakajima A. (1993), Cell-attachment activities of surface immobilized oligopeptides RGD, RGDS, RGDV, RGDT, and YIGSR toward five cell lines, *J. Biomater. Sci., Polym. Ed.*, 4, 3, 235–243.

[91] Li B., Chen J.X., Wang J.H.C. (2006), RGD peptide-conjugated poly(dimethylsiloxane) promotes adhesion, proliferation, and collagen secretion of human fibroblasts, *J. Biomed. Mater. Res. A*, 79, 4, 989-998.

[92] Li J., Ding M., Fu Q., Tan H., Xie X. and Zhong Y. (2008), A novel strategy to graft RGD peptide on biomaterials surfaces for endothelization of small-diamater vascular grafts and tissue engineering blood vessel, *J. Mater. Sci.: Mater. Med.*, 19, 7, 2595–2603.

[93] Morgan A.W., Roskov K.E., Lin-Gibson S., Kaplan D.L., Becker M.L. and Simon C.G. Jr. (2008), Characterization and optimization of RGD-containing silk blends to support osteoblastic differentiation, *Biomaterials*, 29,16, 2556-2563.

[94] Bini E., Foo C.W., Huang J., Karageorgiou V., Kitchel B. and Kaplan D.L. (2006), RGD-functionalized bioengineered spider dragline silk biomaterial, *Biomacromolecules*, 7, 11, 3139-3145.

[95] Andrade F.K., Moreira S.M., Domingues L. and Gama F.M. (2010), Improving the affinity of fibroblasts for bacterial cellulose using carbohydrate-binding modules fused to RGD, *J. Biomed. Mater. Res. A*., 92, 1, 9-17.

[96] Rowley J.A., Madlambayan G. and Mooney D.J. (1999), Alginate hydrogels as synthetic extracellular matrix materials, *Biomaterials*, 20, 1, 45–53.

[97] Ohga Y., Katagiri F., Takeyama K., Hozumi K., Kikkawa Y., Nishi N. and Nomizu M. (2009), Design and activity of multifunctional fibrils using receptor-specific small peptides, *Biomaterials*, 30,35,6731-6738

[98] Lin H.B., Sun W.,Mosher D.F.,García-Echeverría C.,Schaufelberger K.,Lelkes P.I.and Cooper S.L. (1994), Synthesis, surface, and cell-adhesion properties of polyurethanes containing covalently grafted RGD-peptides , *J. Biomed. Mater. Res. A*, 28,3,329-342

[99] Kammerer P.W., Heller M., Brieger J., Klein M.O., Al-Nawas B. and Gabriel M. (2011), Immobilisation of linear and cyclic RGD-peptides on titanium surfaces and their impact on endothelial cell adhesion and proliferation, *Eur. Cells Mater.*, 21, 364-372.

[100] Shu X.Z., Ghosh K., Liu Y., Palumbo F.S., Luo Y., Clark R.A. and Prestwich G.D. (2004),. Attachment and spreading of fibroblasts on an RGD peptide-modified injectable hyaluronan hydrogel, *J. Biomed. Mater. Res. A*, 68, 2, 365-375.

[101] Wilson M.J., Liliensiek S.J., Murphy C.J., Murphy W.L. and Nealey P.F. (2012), Hydrogels with well-defined peptide-hydrogel spacing and concentration: impact on epithelial cell behavior, *Soft Matt.*, 8, 390-398

[102] Lei Y., Rémy M., Labrugère C. and Durrieu M.C. (2012), Peptide immobilization on polyethylene terephthalate surfaces to study specific endothelial cell adhesion, spreading and migration, *J. Mater. Sci; Mater. Med.*, 23, 11, 2761-2772

[103] Derrick S. Grant D.S., Tashiro K.I., Segui-Real B., Yamada Y., Martin G.R. and Kleinman H.K. (1989), Two different laminin domains mediate the differentiation of human endothelial cells into capillary-like structures in vitro, *Cell*, 58, 5, 933–943

[104] Kuehn C., Dubiel E.A., Sabra G., Vermette P. (2012), Culturing INS-1 cells on CDPGYIGSR-, RGD- and fibronectin surfaces improves insulin secretion and cell proliferation, *Acta Biomater.*, 8, 2, 619–626

[105] Schmidt D.R. and Kao W.J. (2007), Monocyte activation in response to polyethylene glycol hydrogels grafted with RGD and PHSRN separated by interpositional spacers of various lengths, *J. Biomed. Mater. Res. A*, 83,3, 617–625

[106] Kama L., Shainb W., Turnera J.N. and Biziosa R. (2002), Selective adhesion of astrocytes to surfaces modified with immobilized peptides, *Biomater.*, 23, 2, 511–515

[107] Ferguson T.A., Mizutani H. and Kupper T.S. (1991), Two integrin-binding peptides abrogate T cell-mediated immune responses in vivo, *Proc. Natl. Acad. Sci. USA*, 88, 18, 8072-8076

[108] Choi B.H, Choi Y.S., Kang D.G., Kim B.J. Song Y.H. and Cha H.J. (2010), Cell behavior on extracellular matrix mimic materials based on mussel adhesive protein fused with functional peptides, *Biomater.*, 31, 34, 8980–8988

[109] Chollet C., Bareille R., Rémy M., Guignandon A., Bordenave L., Laroche G. and Durrieu M.C. (2012), Impact of peptide micropatterning on endothelial cell actin remodeling for cell alignment under shear stress, *Macromolec. Biosci.*, 12, 12, 1648–1659

[110] Wang W., Itoh S., Matsuda A., Aizawa T., Demura M., Ichinose S., Shinomiya K., Tanaka J. (2008), Enhanced nerve regeneration through a bilayered chitosan tube: The effect of introduction of glycine spacer into the CYIGSR sequence, *J. Biomed. Mater. Res. A*, 85,4, 919–928

[111] Nakamura M., Mie M., Nakamura M.and Kobatake E. (2012), Construction of multi-functional extracellular matrix proteins that inhibits migration and tube formation of endothelial cells, *Biotech. Lett.*, 34, 8, 1571-1577

[112] Granera E. et al. (2000), Cellular prion protein binds laminin and mediates neuritogenesis, 76, 1, 85–92

[113] Doyle P.M., Harris J.C., Moody C.M., Sadler P.J., Sims M., Thornton J.M., Uppenbrink J., Viles J.H. (1996), Solution structure of a biologically active cyclic LDV peptide analogue containing a type′ II β-turn mimetic, *Int. J. Peptide Protein Res.,* 47, 6,427–436

[114] Ji Y., Wei Y, Liu X., Wang J., Ren K. and Ji J. (2012), Zwitterionic polycarboxybetaine coating functionalized with REDV peptide to improve selectivity for endothelial cells, *J. Biomed. Mater. Res. A,* 100A, 6, 1387–1397

[115] Zou Z., Zheng Q., Wu Y., Song Y. and Wu B. (2009), Growth of rat dorsal root ganglion neurons on a novel self-assembling scaffold containing IKVAV sequence, *Mater. Sci. Eng. C,* 29, 7, 2099–2103

[116] Foster C.M, Collazo R., Sitar Z. and Ivanisevic A. (2013), Cell behavior on gallium nitride surfaces: Peptide affinity attachment versus covalent functionalization, *Langmuir*, 29, 26, 8377–8384

[117] Schuler M., Hamilton D.W., Kunzler T.P., Sprecher C.M., Michael de Wild, Brunette D.M., Textor M. and TosattiS.G.P.(2009), Comparison of the response of cultured osteoblasts and osteoblasts outgrown from rat calvarial bone chips to nonfouling KRSR and FHRRIKA-peptide modified rough titanium surfaces, *J. Biomed. Mater. Res. B,* 91B, 2, 517–527

[118] Hunter D.D., Cashman N., Morris-Valero R., Bulock J.W., Adams S.P. and Sanes J.R. (1991), An LRE (leucine-arginine-glutamate)-dependent mechanism for adhesion of neurons to S-laminin, *J. Neurosci*, 11, 12, 3960-3971

[119] Ghiselli G., Siracusa L.D. and Iozzo R.V. (1999), Complete cDNA Cloning, Genomic Organization, Chromosomal Assignment, Functional Characterization of the Promoter, and Expression of the Murine Bamacan Gene, *J. Bio. Chem.*, 274, 17384-17393.

[120] Samuel A. Santoro S.A. and Lawing Jr. W.J. (1987), Competition for related but nonidentical binding sites on the glycoprotein IIb-IIIa complex by peptides derived from platelet adhesive proteins, *Cell*, 48,5, 867–873

[121] Yang Z., Strickland D.K. and Bornstein P. (2001), Extracellular matrix metalloproteinase 2 levels are regulated by the low density lipoprotein-related scavenger receptor and thrombospondin 2, *J. Biol. Chem.*, 276, 8403–8408

[122] Dong C.L., Li S.Y, Wang Y., Dong Y, Tang J.Z., Chen J.C. and Chen G.Q. (2012), The cytocompatability of polyhydroxyalkanoates coated with a fusion protein of PHA repressor protein (PhaR) and Lys-Gln-Ala-Gly-Asp-Val (KQAGDV) polypeptide, *Biometer.*, 33,9, 2593–2599

[123] Wojtowicz A.M., Shekaran A., Oest M.E., Dupont K.M., Templeman K.L., Hutmacher D.W., Guldberg R.E. and García A.J. (2010), Coating of biomaterial scaffolds with the collagen-mimetic peptide GFOGER for bone defect repair, *Biomater.*, 31,9, 2574–2582

[124] Pocza P., Süli-Vargha H., Darvas Z and Falus A. (2007), Locally generated VGVAPG and VAPG elastin-derived peptides amplify melanoma invasion via the galectin-3 receptor, *Int. J. Cancer*, 122, 9, 1972–1980

[125] Merle B., Malaval L., Lawler J., Delmas P. and Clezardin P. (1997), Decorin inhibits cell attachment to thrombospondin-1by binding to a KKTR-dependent cell adhesive site present within the N-terminal domain of thrombospondin-1, *J. Cell Biochem.*, 67, 75–83.

[126] Murphy-Ullrich J.E. and Poczatek M. (2000), Activation of latent TGF-β by thrombospondin-1: mechanisms and physiology, *Cytokine Growth Factor Rev*., 11,1-2, 59–69

[127] Kim W.H, Nomizu M., Song S.Y., Tanaka K., Kuratomi Y., Kleinman H.K. and Yamada Y. (1998), Laminin-α1-chain sequence Leu-Gln-Val-Gln-Leu-Ser-Ile-Arg (LQVQLSIR) enhances murine melanoma cell metastases, *Int. J. Cancer*, 77, 4, 632–639

[128] Ribeiro S.M., Poczatek M., Schultz-Cherry S., Villain M. and Murphy-Ullrich, J. E. (1999) The activation sequence of thrombospondin-1 interacts with the latency-associated peptide to regulate activation of latent transforming growth factor-beta, *J. Biol. Chem.* ,274, 13586–13593

[129] Rosca E.V., Stukel J.M., Gillies R.J., Vagner J. and Caplan M.R. (2007), Specificity and Mobility of Biomacromolecular, Multivalent Constructs for Cellular Targeting, *Biomacromolec.*, 8, 12, 3830–3835

[130] Richard B.L., Nomizu M., Yamada Y. and Kleinman H.K. (1996), Identification of synthetic peptides derived from Laminin α1 and α2 chains with cell type specificity for neurite outgrowth, *Experimental Cell Res.*, 228, 1, 98–105

[131] Martin-Manso G., Galli S., Ridnour L.A., Tsokos M., Wink D.A. and Roberts D.D. (2008), Thrombospondin 1 promotes tumor macrophage recruitment and enhances tumor cell cytotoxicity of differentiated U937 Cells, *Cancer Res.*, 68,17, 7090-7099

[132] Kim S.H, Kiick K.L. (2007), Heparin-mimetic sulfated peptides with modulated affinities for heparin-binding peptides and growth factors, 28, 11, 2125–2136

[133] Guo N., Templeton N.S., Al-Barazi H., Cashel J.A., Sipes J.M., Krutzsch H.C. and Roberts D.D. (2000), Thrombospondin-1 promotes α3β1 integrin-mediated adhesion and

neurite-like outgrowth and inhibits proliferation of smallcell lung carcinoma cells. *Cancer Res.* 60, 457–466

[134] Gonzalez Jr J.M., Hu Y., Gabelt B.T., Kaufman P.L. and Peters D.M. (2009), Identification of the active site in the Heparin II domain of fibronectin that increases outflow facility in cultured monkey anterior segments, *Invest. Ophthalmol. Vis. Sci.*, 50, 1, 235-241

[135] Chen Y., Wang X., Weng D., Tian L., Lv L., Tao S. and Chen J. (2009), A TSP-1 synthetic peptide inhibits bleomycin-induced lung fibrosis in mice, *Experimental Toxicologic Pathology*, 61, 1,59-65

[136] Ren B., Yee K.O., Lawler J. and Khosravi-Far R. (2005), Regulation of tumor angiogenesis by thrombospondin-1, *Biochim. Biophy. Acta,* 1765, 2, 178-188

[137] Arora D.K., Das S., Sukumar M., *Analyzing microbes: manual of molecular biology techniques*, Springer, Berlin Heidelberg, 2013.

[138] Kelly S.M., Jess T.J., and Price N.C. (2005), How to study proteins by circular dichroism, *Biochimica et Biophysica Acta (BBA) - Proteins & Proteomics,* 1751, 2, 119–139.

[139] Holzwarth G. and Doty P. (1965), The ultraviolet circular dichroism of polypeptides 1, *J. Amer. Chem. Soc*., 87, 2, 218–228, 1965.

[140] Townend R., Kumosinski T. F., Timasheff S.N., Fasman G.D. and Davidson B. (1966), The circular dichroism of the structure of poly-l-lysine, *Biochem. and Biophys. Res. Communications*, 23, 2, 163–169.

[141] Serdyuk I.N., Zaccai N.R. and Zaccai J., *Methods in molecular biophysics-structure, dynamics, function*, Cambridge, England, 2007.

[142] Susi H. and Byler D.M. (1986), Resolution-enhanced fourier transform infrared spectroscopy of enzymes, *Methods in Enzymology*, 130, 290–311.

[143] Chalikian T.V., Volker J., Plum G.E., and Breslauer K.J. (1999), A more unified picture for the thermodynamics of nucleic acid duplex melting: A characterization by calorimetric and volumetric techniques, *Proc. Natl. Acad. Sci. USA*, 96, 7853–7858.

[144] Plum G.E. and Breslauer K.J. (1995), Calorimetry of proteins and nucleic acids, *Curr. Opin. Struct.Biol.*, 5, 682–690.

[145] http://geneura.ugr.es/cgi-bin/somcd/som.cgi?start=1

[146] Brey W. S., *Physical chemistry and its biological applicatitons*, Academic Press, New York, 1978.

[147] Keselowsky B.G., Collard D.M. and García A.J. (2003), Surface chemistry modulates fibronectin conformation and directs integrin binding and specificity to control cell adhesion, *J. Biomed. Mater. Res. A.,* 66, 2, 247–259

[148] Mann B.K. and West J.L. (2002), Cell adhesion peptides alter smooth muscle cell adhesion, proliferation, migration, and matrix protein synthesis on modified surfaces and in polymer scaffolds. *J. Biomed. Mater. Res.,* 60, 1, 86–93.

[149] Xu C., Yang F., Wang S. and Ramakrishna S. (2004), In vitro study of human vascular endothelial cell function on materials with various surface roughness, *J. Biomed. Mater. Res. A.* 71, 1, 154-61.

[150] Deligiannia D.D., Katsalaa N., Ladasb S., Sotiropouloub D., Amedeec J. and Missirlisa Y.F. (2001), Effect of surface roughness of the titanium alloy Ti–6Al–4V on human bone marrow cell response and on protein adsorption, *Biomater.,* 22,11, 1241–1251.

[151] Ranella A., Barberoglou M., Bakogianni S., Fotakis C. and Stratakis E. (2010), Tuning cell adhesion by controlling the roughness and wettability of 3D micro/nano silicon structures, *Acta Biomater.,* 6, 7, 2711-2720

[152] Wong J.Y., Leach J.B. and Brown X. Q. (2004), Balance of chemistry, topography, and mechanics at the cell–biomaterial interface: Issues and challenges for assessing the role of substrate mechanics on cell response, *Surface Science,* 570, 1-2, 119–133.

[153] Vladkova T.G. (2010), Surface engineered polymeric biomaterials with improved biocontact properties, *Int. J. Polym. Sci.,* 2010, 1-22.

[154] Lensen M.C., Schulte V.A., Salber J., Diez M., Menges F. and Moller M. (2008), Cellular responses to novel, micropatterned biomaterials, *Pure Appl. Chem.* 80, 11, 2479–2487.

[155] Bilek M.M. and McKenzie D.R. (2010), Plasma modified surfaces for covalent immobilization of functional biomolecules in the absence of chemical linkers: towards better biosensors and a new generation of medical implants, *Biophys. Rev.,* 2, 55-65

[156] Croll T.I., O'Connor A.J., Stevens G.W. and Cooper-White J.J. (2004), Controllable surface modification of poly(lactic-co-glycolic acid) (PLGA) by hydrolysis or aminolysis I: physical, chemical, and theoretical aspects, *Biomacromolecules,* 5, 463–73.

[157] Massia S.P. and Hubbell J.A. (1991), Human endothelial cell interactions with surface-coupled adhesion peptides on a nonadhesive glass substrate and two polymeric biomaterials, *J. Biomed. Mater. Res.,* 25, 2, 223-242.

[158] Pope N.M., Kulcinski D.L., Hardwick A. and Chang Y.A. (1993), New applications of silane coupling agents for covalently binding antibodies to glass and cellulose solid supports. *Bioconjugate chem.,* 4, 2, 166-171.

[159] Bhatia S.K., Shriver-Lake L.C., Prior K.J., Georger J.H., Calvert J.M., Bredehorst R. and Ligler F.S. (1989), Use of thiol-terminal silanes and heterobifunctional crosslinkers for immobilization of antibodies on silica surfaces, *Anal. Biochem.,* 178, 2, 408-413.

[160] Mikulikova R., Moritz S., Gumpenberger T., Olbrich M., Romanin C., Bacakova L., Svorcik V. and Heitz J. (2005), Cell microarrays on photochemically modified polytetrafluoroethylene, *Biomaterials,* 26, 27, 5572-5580.

[161] Gumpenberger T., Heitz J., Bäuerle D., Kahr H., Graz I., Romanin C., Svorcik V. and Leisch F. (2003), Adhesion and proliferation of human endothelial cells on photochemically modified polytetrafluoroethylene, *Biomaterials,* 24, 28, 5139-5144.

[162] Kam L., Shain W., Turner J.N., Bizios R. (2002), Selective adhesion of astrocytes to surfaces modified with immobilized peptides, *Biomaterials,* 23, 2, 511-515.

[163] Xu F.J., Neoh K.G. and Kang E.T. (2009), Bioactive surfaces and biomaterials via atom transfer radical polymerization, *Progress in Polymer Science,* 34,8, 719–761.

[164] Hubbell J.A., Massia S.P. and Drumheller P.D. (1992), Surface-grafted cell-binding peptides in tissue engineering of the vascular graft, *Ann. N. Y. Acad. Sci.,* 665,253-258.

[165] Biesalski M., Knabel A., Tu R. and Tirrell M. (2006), Cell adhesion on a polymerized peptide–amphiphile monolayer, *Biomaterials,* 27, 8, 1259–1269.

[166] Mrksich M. (2009), Using self-assembled monolayers to model the extracellular matrix, *Acta Biomater*., 5, 3, 832-841.

[167] Albeda S.M. and Buck C.A. (1990), Integrins and other cell adhesion molecules, *FASEB J.,* 4, 11, 2868-2880.

[168] Ruoslahti E. (1991), *Integrins,* J. Clin. Invest., 87, 1, 1-5.

[169] Humphries M.J. (1990), The molecular basis and specificity of integrin-ligand interactions, *J. cell Sci.,* 97,4, 585-592.

[170] Burgess B.T., Myles J.L. and Dickinson R.B. (2000), Quantitative analysis of adhesion-mediated cell migration in three-dimensional gels of RGD-grafted collagen, *Ann. Biomed. Eng.* , 28, 1, 110-118

[171] Chimenti I., Rizzitelli G., Gaetani R., Angelini F., Ionta V., Forte E., Frati G., Schussler O., Barbetta A., Messina E., Dentini M., Giacomello A. (2011), Human cardiosphere-seeded gelatin and collagen scaffolds as cardiogenic engineered bioconstructs, *Biomater.*, 32, 35, 9271–9281

[172] Myles J.L., Burgess B.T. and Dickinson R.B. (2000), Modification of the adhesive properties of collagen by covalent grafting with RGD peptides, *Biomater Sci, Poly. Ed.* , 11, 1, 69-86.

[173] He J., Huang T., Gan L., Zhou Z., Jiang B., Wu Y., Wu F., Gu Z. (2012), Collagen-infiltrated porous hydroxyapatite coating and its osteogenic properties: in vitro and in vivo study, *J. Biomed. Mater. Res. A.*, 100, 7, 1706-1715.

[174] Hejcl A., Sedý J., Kapcalová M., Toro D.A., Amemori T., Lesný P., Likavcanová-Mašínová K., Krumbholcová E., Prádný M., Michálek J. and Burian M. et al. (2010), HPMA-RGD hydrogels seeded with mesenchymal stem cells improve functional outcome in chronic spinal cord injury, *Stem Cells Dev.*, 19, 10, 1535-1546.

[175] Guarnieri D., De Capua A., Ventre M., Borzacchiello A., Pedone C., Marasco D., Ruvo M. and Netti P.A. (2010), Covalently immobilized RGD gradient on PEG hydrogel scaffold influences cell migration parameters, *Acta Biomater.*, 6, 7, 2532-2539.

[176] Lee H., Choi B.G., Moon H.J., Choi J., Park K., Jeong B. and Han D.K. (2012), Chondrocyte 3D-culture in RGD-modified crosslinked hydrogel with temperature-controllable modulus, *MacroMol. Res.* 20, 1, 106-111.

[177] Glass J., Blevitt J., Dickerson K., Pierschbacher M. and Craig W.S. (1994), Cell attachment and motility on materials modified by surface-active RGD-containing peptides, *Ann. N. Y. Acad. Sci.* 745,177-186.

[178] Kok R.J.,Schraa A.J.,Bos E.J. , Moorlag H.E., Ásgeirsdóttir S.A. ,Everts M.,Meijer D.K.F. and Molema G. (2002), Preparation and functional evaluation of RGD-modified proteins as αvβ3 Integrin directed therapeutics, *Bioconjugate Chem.*, 13, 1, 128–135

[179] Huang Y.H., Ho H.P., Wu S.Y. and Kong S.K. (2012), Detecting phase shifts in surface plasmon resonance: A Review, *Adv. Opt. Tech.*, 2012, ID471957.

[180] Le Saux G., Magenau A., Böcking T., Gaus K. and Gooding J.J. (2011), The relative importance of topography and RGD ligand density for endothelial cell adhesion, *PLoS One.* , 6, 7, e21869

[181] Rowley J.A.and Mooney D.J. (2002), Alginate type and RGD density control myoblast phenotype, *J. Biomed. Mater. Res.*, 60, 2, 217-223.

[182] Addadi L. and Weiner S. (1985), Interactions between acidic proteins and crystals: stereochemical requirements in biomineralization, *Proc. Natl. Acad. Sci. USA*, 82, 12, 4110-4114.

[183] Lowenstam H.A. (1981), Minerals formed by organisms, *Science*, 211, 4487, 1126-1131

[184] Busch S. (2004), Regeneration of human tooth enamel. *Angew. Chem. Int. Ed*. 43, 11, 1428-1431.

[185] Baldassarri M., Margolis H.C. and Beniash E. (2008), Compositional determinants of mechanical properties of enamel. *J. Dent. Res.* 2008, 87, 645-649.

[186] Fong H., Foster B.L., Sarikaya M. and Somerman M.J. (2009), Structure and mechanical properties of Ank/Ank mutant mouse dental tissues--an animal model for studying periodontal regeneration. *Arch. Oral Biol.*, 54, 570-576.

[187] Salih E., Wang J.X.,Mah J. and Fluckiger R. (2002), Natural variation in the extent of phosphorylation of bone phosphoproteins as a function of in vivo new bone formation induced by demineralized bone matrix in soft tissue and bony environments. *J. Biochem.*, 2002, 364, 465-474.

[188] Alves N.M., Leonor I.B., Azevedo H.S., Reis R.L. and Mano J.F. (2010), Designing biomaterials based on biomineralization of bone. *J. Mater. Chem.*, 20, 2911-2921.

[189] Mahamid J., Aichmayer B., Shimoni E., Ziblat R., Li C.H., Siegel S., Paris O., Fratzl P., Weiner S. and Addadi L. (2010), Mapping amorphous calcium phosphate transformation into crystalline mineral from the cell to the bone in zebrafish fin rays. *Proc. Natl. Acad. Sci. USA*, 107, 6316-6321

[190] Hoang Q.Q., Sicheri F., Howard A.J. and Yang D.S. (2003), Bone recognition mechanism of porcine osteocalcin from crystal structure, *Nature*, 425, 977–980.

[191] Margolis H.C., Beniash E. and Fowler C.E. (2006), Role of macromolecular assembly of enamel matrix proteins in enamel formation, *J. Dent. Res.*, 85, 775–793.

[192] Sarikaya, M. (1999), Biomimetics: Materials fabrication through biology, *Proc. Natl. Acad. Sci. USA*, 96, 14183–14185.

[193] Hunter, G.K., Hauschka, P.V., Poole, A.R., Robsenberg, L.C., and Goldberg, H.A. (1996). Nucleation and inhibition of hydroxyapatite formation by mineralized tissue proteins, *J. Biochem.* , 317, 59–64.

[194] Lakshminarayanan, R., Vivekanandan, S., Samy, R.P., Banerjee, Y., Chi-Jin, E.O., Teo, K.W., Jois, S.D.S., Kini, R.M. and Valiyaveettil, S. (2008), Structure, self-assembly, and dual role of a betadefensin- like peptide from the chinese soft-shelled turtle eggshell matrix. *J. Am. Chem. Soc.*, 130, 4660-4668.

[195] He G., Gajjeraman S. , Schultz D., Cookson D. , Qin C. ,Butler W.T., Hao J. and George A. (2005), Spatially and temporally controlled biomineralization is facilitated by interaction between self-assembled dentin matrix protein 1 and calcium phosphate nuclei in solution, *J. Biochem.*, 44, 49, 16140–16148.

[196] Tsuji T., Onumasuji K., Yamamoto A., Iijima M. and Shiba K. (2008), Direct transformation from amorphous to crystalline calcium phosphate facilitated by motif-programmed artificial proteins, *Proc. Natl. Acad. Sci. USA*, 105, 44, 16866–16870.

[197] Gomes S., Leonor I.B., Mano J.F., Reis R.L. and Kaplan D.L. (2011), Spider silk-bone sialoprotein fusion proteins for bone tissue engineering, *Soft Matter*, 7, 4964-4973

[198] Gomes S., Gallego-Llamas J., Leonor I.B., Mano J.F., Reis R.L. and Kaplan D.L. (2013), In vivo biological responses to silk proteins functionalized with bone sialoprotein, *Macromol. Biosci.*, 13, 4, 444–454

[199] Jeon E. and Jang J-H. (2009), Protein engineering of a fibroblast growth factor 2 protein for targeting to bone mineral hydroxyapatite, *Protein and Peptide Lett*., 16, 6, 664-667(4)

[200] Kang W., Kim T-I, Yun Y., Kim H-W. and Jang J-H. (2011), Engineering of a multi-functional extracellular matrix protein for immobilization to bone mineral hydroxyapaptite, *Biotechnol Lett.*, 33, 199-204

[201] Goldstein J.I., Newbury D.E., Echlin P., Joy D.C., Lyman C.E., Lifshin E., Sawyer L. and Michael J.R., *Scanning electron microscopy and X-ray microanalysis*, Kluwer Academic/Plenum Publishers, New York, 2003.

[202] Weiner S., Addadi L. and Mater J. (1997), Design strategies in mineralized biological materials, *J. Mater. Chem.*, 7, 689-702.

[203] George A., Bannon L., Sabsay B., Dillon J.W., Malone J., Veis A., Jenkins N.A., Gilbert D.J. and Copeland N.G. (1996), The Carboxyl-terminal domain of phosphophoryn contains unique extended triplet amino acid repeat sequences forming ordered carboxyl-posphate interaction ridges that may be essential in the biomineralization rrocess, *J. Biol. Chem.* 271, 32869-32873.

[204] Fernández M.E., Zorrilla-Cangas C., García-García R., Ascencio J.A. and Reyes-Gasga J. (2003), New model for the hydroxyapaptite-octacalcium phosphate interface, *Acta Cryst.B*, 2, 175-181

[205] Ito N., Kamitakahara M., Murakami S., Watanabe N. and Ioku K. (2010), Hydrothermal synthesis and characterization of hydroxyapatite from octacalcium phosphate, *J.Ceramic Soc. Japan*, 118, 8, 762-766

[206] Zhang H., Yan Y., Wang Y. and Li S. (2003), Morphology and formation mechanism of hydroxyapatite whiskers from moderately acid solution, Mat. Res, 6, 1, 1516-1439

[207] Brown W.E. (1966), Crystal growth of bone mineral, *Clin. Orthop. Relat. Res.*,.44, 205-220

[208] Mathew M., Brown W.E., Schroeder L.W. and Dickens B. (1988), Crystal structure of octacalcium bis (hydrogenphosphate) tetrakis(phosphate) pentahydrate, $Ca_8(HPO_4)_2(PO_4)_4 \cdot 5H_2O$, *J. Chem. Crystallogr*, 18, 235–250.

[209] Anada T., Kumagai T., Honda Y., Masuda T., Kamijo R., Kamakura S., Yoshihara N., Koriyagama T.,Shimauchi H. and Suzuki O. (2008), Dose-dependent osteogenic effect of octacalcium phosphate on mouse bone marrow stromal cells. *Eng. Part A*, 14, 965–978.

[210] Suzuki O., Kamakura S., Katagiri T., Nakamura M., Zhao B., Honda Y. and Kamijo R. (2006), Bone formation enhanced by implanted octacalcium phosphate involving conversion into Ca-deficient hydroxyapaptite, *Biomater.*, 27, 2671–2681

[211] Suzuki O., Nakamura M., Miyasaka Y., Kagayama M., and Sakurai M. (1991), Bone formation on synthetic precursors of hydroxyapatite, *Tohoku J. Exp. Med.*, 164, 37-50.

[212] Iijima M., Du C., Abbott C., Doi Y. and Oldak-Moradian J. (2006), Control of apatite crystal growth by the co-operative effect of a recombinant porcine amelogenin and fluoride, *Eur. J. Oral Sci.*, 114, 304–307.

[213] Chou Y.F., Huang W., Dunn J.C.Y., Miller T.A. and Wu B.M. (2005), The effect of biomimetic apatite structure on osteoblast viability, proliferation and gene expression, *Biomaterials*, 26, 285–295

[214] Zhu M., Wang C., Meng D. and Diao G. (2013), In situ synthesis of silver nanostructures on magnetic Fe3O4@C core–shell nanocomposites and their application in catalytic reduction reactions, *J. Mater. Chem. A* , 1, 2118-2125

[215] Singh R. and Nalwa H.S. (2011), Medical Applications of Nanoparticles in Biological Imaging, Cell Labeling, Antimicrobial Agents, and Anticancer Nanodrugs, *J. Biomed. Nanotech.*, 7, 7, 489-503.

[216] Saha K., Agasti S.S., Kim C. , Li X., and Rotello V.M. (2012), Gold Nanoparticles in Chemical and Biological Sensing, *Chem. Rev.*, 112, 5, 2739–2779

[217] Chang L.T. and Yen C.C. (1995), Studies on the preparation and properties of conductive polymers. VIII. Use of heat treatment to prepare metallized films from silver chelate of PVA and PAN, *J. Appl. Polymer Sci.*, 55, 2, 371–374.

[218] Wormeester H., Henry A-I., Kooij E.S., Poelsema B. and Pileni M-P. (2006), Ellipsometric identification of collective optical properties of silver nanocrystal arrays, *J. Chem. Phys.*, 124, 204713.

[219] Li P., Li J., Wu C.,Wu Q. and Li J. (2005), Synergistic antibacterial effects of β-lactam antibiotic combined with silver nanoparticles, *Nanotech.*, 16, 1912–1917

[220] Tian J., Wong K.K., Ho C.M., Lok C.N., Yu W.Y., Che C.M., Chiu J.F. and Tam P.K. (2007), Topical delivery of silver nanoparticles promotes wound healing, *ChemMedChem*, 2, 1, 129–136.

[221] Sharverdi A.R., Mianaeian S., Shahverdi H.R., Jamalifar H. and Nohi A.A. (2007), Rapid synthesis of silver nanoparticles using culture supernatants of Enterobacteria: a novel biological approach, *Process Biochem*., 42, 919–923.

[222] Liu F.K., Hsu Y.C., Tsai M.H. and Chu T.C. (2007), Using γ-irradiation to synthesize Ag nanoparticles, *Mater. Lett.* , 61, 11-12, 2402 – 2405.

[223] Remita S., Fontaine P., Lacaze E., Borensztein Y., Sellame H., Farha R., Rochas C. and Goldmann M. (2007), X-ray radiolysis induced formation of silver nano-particles: A SAXS and UV–visible absorption spectroscopy study, *Nucl. Instrum. Methods Phys. Res. Sect. B*, 263, 2, 436 –440.

[224] Raffia M., Rumaiz A.K., Hasan M.M. and Shah S.I. (2007), Studies of the growth parameters for silver nanoparticle synthesis by inert gas condensation, *J. Mater. Res.*, 22, 12, 3378-3384

[225] Lee E., Longhai Piao L. and Kim J. (2012), Synthesis of silver nanoparticles from the decomposition of silver(I)[bis(alkylthio)methylene]malonate complexes, *Bull. Korean Chem. Soc.*, 33, 1, 60-64

[226] Frattini A., Pellegri N., Nicastro D. and Sanctis O. (2005), Effect of amine groups in the synthesis of Ag nanoparticles using aminosilanes, *Mater. Chem. Phys.*, 94,1, 148–152

[227] Mann S., *Biomimetic Materials Chemistry*, VCH, New York, 1996.

[228] Kalimuthu K., Babu R.S., Venkataraman D., Bilal M. and Gurunathan S. (2008), Biosynthesis of silver nanocrystals by Bacillus licheniformis, *Colloids Surf. B: Biointerfaces*, 65, 150-153.

[229] Mukherjee P., Ahmad A., Mandal D., Senapati S., Sainkar S.R., Khan M.I., Parischa R., Ajaykumar P.V., Alam M., Kumar R. and Sastry M. (2001), Fungus-Mediated Synthesis of Silver Nanoparticles and Their Immobilization in the Mycelial Matrix: A Novel Biological Approach to Nanoparticle Synthesis, *Nano lett.*, 1, 1,0, 515-519

[230] Klaus-Joerger T., Joerger R., Olsson E. and Granqvist C.G. (2001), Bacteria as workers in the living factory: metal-accumulating bacteria and their potential for materials science, *Trend Biotechnol.*, 9, 15–20.

[231] Kowshik M., Ashtaputre S., Kharrazi S., Vogel W., Urban J., Kulkarni S.K. and Paknikar K.M. (2003), Extracellular synthesis of silver nanoparticles by a silver-tolerant yeast strain MKY3, *Nanotech*. 14, 95-100

[232] Kathiresan K., Manivannan S., Nabeel M.A. and Dhivya B. (2009), Studies on silver nanoparticles synthesized by a marine fungus, Penicillium fellutanum isolated from coastal mangrove sediment , *Colloids Surf. B*, 71, 1, 133–137

[233] El-Rafie H.M., El-Rafie M.H. and Zahranc M.K. (2013),Green synthesis of silver nanoparticles using polysaccharides extracted from marine macro algae, *Carbohydr. Poly.*, 96, 2, 403-410

[234] Haefli C., Franklin C. and Hardy K. (1984), Plasmid determined silver resistance P. stutzeri isolated from silver mine. J. Bacteriol., 158, 389-392

[235] Chen J.C., Lin Z.H. and Ma, X.X. (2003), Evidence of the production of silver nanoparticles via pretreatment of Phoma sp. 32883 with silver nitrate, *Lett. Appl. Microbiol*, 37,105–108.

[236] Bhainsa K.C. and D'Souza S.F. (2006), Extracellular biosynthesis of silver nanoparticles using the fungus Aspergillus fumigatus, *Colloids Surf. B*, 47, 160–164.

[237] Ahmad A., Mukherjee P., Senapati S., Mandal D., Khan M.I., Kumar R. and Sastry M. (2003), Extracellular biosynthesis of silver nanoparticles using the fungus Fusarium oxysporum, *Coll.Surf. B*, 28, 4, 313–318

[238] Prathna T.C., Chandrasekaran N., Raichur A.M. and Mukherjee A. (2011), Biomimetic synthesis of silver nanoparticles by Citrus limon (lemon) aqueous extract and theoretical prediction of particle size, *Colloids Surf. B: Biointerfaces*, 82, 152–159,

[239] Tripathy A., Raichur A.M., Chandrasekaran N, Prathna T.C. and Mukherjee A. (2010), Process variables in biomimetic synthesis of silver nanoparticles by aqueous extract of Azadirachta indica (Neem) leaves, *J. Nanopart. Res.*, 12, 237–246

[240] Liz-Marzan L.M. (2006), Tailoring surface plasmons through the morphology and assembly of metal nanoparticles, *Langmuir*, 22, 32–41.

[241] Naik R.R, Stringer S.J., Agarwal G. Jones S.E. and Stone M.O. (2002), Biomimetic synthesis and patterning of silver nanoparticles, *Nat. Mater*., 1, 169 – 172.

[242] Desai R., Mankad V., Gupta S.K. and Jha P.K. (2012), Size distribution of silver nanoparticles: UV-visible spectroscopic assessment, *Nanosci. Nanotech. Lett.*, 4, 1, 30-34.

[243] Zhang X., Yang P., Yang W.and Chen J. (2008), The bio-inspired approach to controllable biomimetic synthesis of silver nanoparticles in organic matrix of chitosan and silver-binding peptide (NPSSLFRYLPSD), *Mater. Sci. Eng. C*, 28, 237–242